Contributions of anisotropic and heterogeneous tissue modulus to apparent trabecular bone mechanical properties

Yue Yu

Submitted in partial fulfillment of the
requirements for the degree of
Doctor of Philosophy
in the Graduate School of Arts and Sciences

COLUMBIA UNIVERSITY

2017

© 2017
Yue Yu
All rights reserved

Contributions of anisotropic and heterogeneous tissue modulus to apparent trabecular bone mechanical properties

Yue Yu

ABSTRACT

The highly optimized hierarchical structure of trabecular bone is a major contributor to its remarkable mechanical properties. At the micro-scale level, individual plate-like and rod-like trabeculae are interconnected, forming a complex trabecular architecture. It is widely believed that bone strength, an important mechanical characteristic that describes the capability of bone to resist fracture, is largely determined by the tissue-level material properties of these microscopic trabecular elements. However, due to the complicated microstructure and irregular morphology of trabecular bone, a link between the tissue-level and the apparent-level mechanics in trabecular bone has never been established. Thus, the goal of this thesis is to examine the tissue-level material properties of trabecular bone and their contribution to apparent-level bone mechanics, and ultimately to improve our fundamental understanding and assessment of bone strength in diseased and healthy patients.

At the micro-scale level, plate-like and rod-like trabeculae are distinctly aligned along different orientations on the anatomical axis of the skeleton. Also, the highly organized underlying ultrastructure of bone tissue suggests trabecular bone might possess an anisotropic tissue modulus, i.e. different modulus in the axial and lateral cross-section of a trabecula. In this

thesis, we studied this tissue-level anisotropy by examining mechanical properties of individual trabecular plates and rods aligned longitudinally, obliquely, and transversely on the anatomical axis using micro-indentation. We discovered that, despite the different orientations of trabeculae, tissue moduli are higher in the axial direction than in the lateral direction for both plates and rods. We also discovered that plates have a higher tissue modulus than rods, suggesting different degrees of mineralization. Furthermore, the tissue mineral density correlated strongly but distinctly with tissue modulus in the axial and lateral directions, providing descriptions on how spatially heterogeneous mineralization at the tissue level affects the tissue modulus.

After characterization of the anisotropic and heterogeneous modulus of trabecular bone at the tissue level, we then sought to investigate its contribution to apparent-level mechanical properties, including apparent Young's modulus and yield strength. Non-linear FE voxel models incorporating experimentally determined anisotropy and heterogeneity were created from micro-computed tomography (μCT) images of healthy trabecular bone samples. Apparent Young's modulus and yield strength predicted by the models were compared to and correlated with gold standard mechanical testing measurements, as well as to the same FE models without incorporation of anisotropy and/or heterogeneity. We discovered that the anisotropic model prediction was highly correlated and indistinguishable from mechanical testing measurements. However, the prediction power of the model was not enhanced by incorporating anisotropy and heterogeneity (compared to a homogeneous and isotropic model), suggesting that variances in tissue-level material properties contribute minimally to the apparent-level bone behaviors in healthy bone.

However, the possibility remained that a more substantial contribution could arise in diseased bone, particularly diseases in which tissue-level properties are compromised. Therefore,

we studied trabecular bone in two diseased conditions – subchondral bone in human knees affected by osteoarthritis and pelvic bone affected by adolescent idiopathic sclerosis – to see how disease can alter the tissue-level and, consequently, apparent-level bone mechanics. In OA bone, we found a significant decrease in tissue modulus in the subchondral bone under severely damaged cartilage compared to control, which provides an explanation for a minimal increase in apparent stiffness with an almost doubled bone volume fraction. In AIS bone, no differences were found in tissue-level or apparent-level Young's modulus compared to control. However, the mineral density was found to play a distinct role in the modulus of growing bone tissue compared to mature bone.

Table of Contents

List of Tables iv
List of Figures v
Acknowledgements viii
Chapter 1. Overview 1
1.1. Background 1
1.1.1. Human bone and its hierarchy 1
1.1.2. Bone growth, acquisition, and the mineralization process 3
1.1.3. Bone strength determinants 4
1.1.4. Basic mechanics of bone 7
1.2 Characterization of trabecular plate and rod microstructure 9
1.2.1 Trabecular morphology and μCT 9
1.2.2 Individual Trabecula Segmentation (ITS) 11
1.3 Characterization of intrinsic tissue material properties 12
1.3.1 Depth-sensing indentation and tissue modulus 12
1.3.2 Heterogeneous distribution of tissue mineralization 14
1.3.3 Diseases or treatments affecting bone material properties 15
1.4 Finite element modeling of human bone 17
1.4.1 High resolution image-based finite element modeling 17
1.4.2 Homogeneous and heterogeneous finite element models 18
1.5 Scientific and Clinical Motivations 20
1.6 Specific Aims and Organization 22
1.6.1 Specific Aims 22
1.6.2 Organization 22
Chapter 2. Development and calibration of a micro-indentation technique to fast and accurately measure tissue modulus 27
2.1. Introduction 27
2.2. Mechanical theory of depth-sensing indentation 28
2.2.1. Depth-sensing indentation theory and assumptions 28
2.2.2. Calculation of Young's modulus 30
2.3. Micro-indentation specification and performance 31
2.3.1 Setup of the indentation system 31

2.3.2 Performance 32
2.3.3 Instrument compliance and calibration 32
2.4. Discussion 33
Chapter 3. Heterogeneous and anisotropic tissue mechanical properties of trabecular bone 41
3.1. Introduction 41
3.2. Materials and Methods 43
3.2.1. Specimen preparation and μCT imaging 43
3.2.2. ITS-based anatomic direction and indentation direction selection 45
3.2.3. Microindentation and tissue modulus measurements 46
3.2.4. Image registration to co-localize TMD and tissue modulus 47
3.3. Results 48
3.3.1. TMD and tissue modulus difference between plates and rods 48
3.3.2. Tissue modulus difference between axial and lateral directions 49
3.3.3. Correlations between TMD and Young's modulus in different indentation directions 49
3.4. Discussion 50
Chapter 4. μFE modeling with anisotropic and heterogeneous tissue properties 64
4.1. Introduction 64
4.2. Materials and Methods 66
4.2.1. Specimen Preparation 66
4.2.2. μCT imaging and segmentation 67
4.2.3. μFE modeling: homogeneous/isotropic model and heterogeneous/isotropic model 67
4.2.4. Development of anisotropic and heterogeneous μFE voxel model 69
4.2.5. Mechanical testing 70
4.2.6. Statistical Analyses 70
4.3. Results 71
4.3.1. Elastic modulus predicted by homogeneous/isotropic model and heterogeneous/anisotropic model compared to mechanical testing 71
4.3.2. Elastic modulus predicted by heterogeneous/isotropic model and heterogeneous/anisotropic model compared to mechanical testing 71
4.4. Discussion 72
Chapter 5. Tissue material properties of adolescent idiopathic scoliosis patients 79
5.1. Introduction 79
5.2. Materials and Methods 80

5.2.1. Subjects 80
5.2.2. μCT 82
5.2.3. ITS 83
5.2.4. Microindentation 83
5.2.5. FE analyses 84
5.2.6. Statistical analysis 84
5.3. Results 85
5.3.1. Microstructural results 85
5.3.2. Microindentation results 85
5.3.3. FE results 85
5.4. Discussion 86
Chapter 6. Tissue material properties and microstructural changes in subchondral bone in osteoarthritis with/without type 2 diabetes 94
6.1. Introduction 94
6.2. Materials and Methods 96
6.2.1. Subjects 96
6.2.2. μCT and ITS 97
6.2.3. Microindentation tests 97
6.2.4. μFE models 98
6.2.5. Statistics 98
6.3. Results 99
6.3.1. Microstructural differences 99
6.3.2. Microindentation results 99
6.3.3. FE results 100
6.4. Discussion 100
Chapter 7. Summary and future work 110
7.1. Anisotropic trabecular plates and rods 111
7.2. Contribution of anisotropic trabecular plate and rod to apparent level mechanical properties 112
7.3. Diseases altered tissue material properties and apparent level mechanical properties 112
7.4. Future work 113
Bibliography 115

List of Tables

Table 3.1. Donor and sample information in the experimental set. 55

Table 4.1. Donor and sample information in the experimental set. 75

Table 5.1 Sample information including age, spine curve angle, bone mass Z-score, and standard μCT measurements. 89

Table 5.2 Trabecular micro-architecture measured with ITS in AIS and controls. Difference %= (AIS-control)/control %. 90

Table 5.3 Apparent modulus in AIS and controls calculated by homogeneous and heterogeneous FE analysis. Difference %= (AIS-control)/control %..... 91

Table 6.1 Patient information and bone volume fraction of regular OA, T2DM/OA, and control for A) morphological analysis B) Indentation 104

Table 6.2 Detailed ITS results of the comparison between regular OA, T2DM/OA and control. * represents significant difference from control and # represents significant difference tween T2MD/OA and regular OA. *p<0.05, #p<0.05 105

List of Figures

Figure 1.1. Schematic diagram of bone hierarchical levels of organization (adapted from http://www.iupui.edu/~bbml/Figures/hier.jpg). 25

Figure 1.2. Load-deformation plot (left) and stress-strain plot (right) depicting the various properties that can be used to characterize a material..... 26

Figure 2.1 Contact geometry of a cylindrical flat punch. a:indenter radius; Us is the deformation of the sample 37

Figure 2.2 Schematic of the indentation system setup. A) Linear actuator; B) Load cell; C) Displacement sensor; D) Indenter; E) Specimen; F) Specimen holder and XY-table G) Load frame 38

Figure 2.3 Illustration of the loading and unloading curves. The slope at the initial unloading point is defined as stiffness 39

Figure 2.4 Loading profile of each indentation test. The unloading curve is highly linear with an unloading speed of 0.03 μm/s 40

Figure 3.1 Illustration of a μCT scanning with density calibration phantoms and the linear regression of the calibration relationship 56

Figure 3.2 Illustration of ITS display of trabecular type and anatomic orientation on the indentation surface. 57

Figure 3.3 Illustration of anatomic directions and indentation directions. 58

Figure 3.4 Illustration of co-localizing the TMD and Young's modulus. 59

Figure 3.5 Comparisons of Young's modulus and co-localized TMD between plates and rods.. 60

Figure 3.6 Comparisons of Young's modulus between axial and lateral directions for all trabecular types and anatomic directions; *p<0.05. 61

Figure 3.7 Comparisons of Young's modulus between axial and lateral directions for all trabecular types and anatomic directions; *p<0.05. 62

Figure 3.8 Simulated indentation modulus corresponding to the different angle between the material direction and indentation directions. 63

Figure 4.1. Compliance matrix and local-to-global coordinates transformation. E_{axi} : axial modulus; E_{lat}: lateral modulus; ν_{axi}: Poisson's ratio in axial direction, ν_{lat}: Poisson's ratio in lateral direction; G_{Lat}: shear modulus in lateral direction 76

Figure 4.2 Linear regression of A) Young's modulus and B) between predictions by isotropic model, anisotropic model, and measurements by mechanical testing. 77

Figure 4.3. Linear regression of A) Young's modulus and B) yield strength between predictions by heterogeneous/isotropic models, heterogeneous/anisotropic model, and measurements by mechanical testing. 78

Figure 5.1. Comparisons of Young's modulus and co-localized TMD between AIS and control 92

Figure 5.2. Correlations between tissue modulus and TMD in A) AIS, B) control, and C) overall samples, as well as D) correlation between apparent Young's modulus predicted by two types of FE models. 93

Figure 6.1 Illustration of sub-region selections. a, b) Top-down view of a tibial plateau from control and OA; c, d) Top-down view from reconstructed μCT images of control and OA; e, f) μCT images of the anterior-posterior view. A: anterior; P: posterior; C: central; MA: medial anterior; MC: medial central; LA: lateral anterior; LC: lateral central 106

Figure 6.2 Microstructural comparisons between OA, T2DM/OA, and control on A) medial side and B) lateral side. 107

Figure 6.3 Tissue modulus comparisons between A) medial and lateral side, and B) T2DM/OA, regular OA, and control. 108

Figure 6.4 Apparent elastic modulus predicted by FE analysis.* indicate significance from the other groups. *p<0.05 109

Acknowledgements

I owe my deepest gratitude to my dear family, my great mentor, colleagues, friends, and everyone else who has offered me support and help throughout my Ph.D. study. It is the encouragement and trust bestowed on me that drove me to overcome all the challenges and complete this thesis work.

First, I would like to express my greatest gratitude to my research advisor, Prof. X. Edward Guo, who provided me the precious opportunity to pursue my Ph.D. study in the first place. It was dream-come-true for me to study at a prestigious Ivy League university. It has been a privilege for me to have Ed guiding me in every step of my research and life during the past five years. My rigorous training has given me the engineering skills and knowledge to conduct research. More importantly, it has equipped me to solve any problem with determination, confidence, and a critical and sharp mind. Ed has never given up on me when I struggled, and he has always encouraged me to try the impossible. It is that one extra step that makes me complete the research for this thesis and my Ph.D. study.

In addition, I would like to extend my gratitude to our collaborators, Dr. Elizabeth Shane, Dr. Kyle Nishiyama, and Fernando Rosete at the Columbia University Medical Center. I would also like to thank Dr. Yan Chen and Dr. William Lu from the University of Hong Kong for the opportunities to study knee osteoarthritis together. I would also thank Kayee Cheuk, Dr. Wayne Lee, and Dr. Jack Chen from The Chinese University of Hong Kong for offering me to research on very valuable adolescent idiopathic scoliosis subjects.

Furthermore, I want to give my special thanks to my wonderful colleagues in the Bone Bioengineering Lab: Dr. Bin Zhou, Dr. Ji Wang, Dr. Genevieve Brown, Jenny Hu, Eddie Zhang, Andrea Morrell, Sam Robinson, Rachel Sattler, and previous lab member Dr. Andrew Baik. I

feel so proud and lucky to be part of this great team. We are always like a big family supporting each other with the best we can offer. In particular, I would like to thank Dr. Bin Zhou and Dr. Ji Wang for their guidance and suggestions in my research as well as for providing instrumental help for my projects. My special gratitude goes to my office neighbor and good friend Dr. Genevieve Brown for our great friendship and advice on my research and writing. I also thank Jenny Hu and Eddie Zhang for assisting me with my research projects.

In addition, I would like to thank the faculty and staff in the Department of Biomedical Engineering – Prof. Barclay Morrison, Prof. Christopher Jacobs, Prof. Henry Hess, Prof. Stavros Thomopoulos – for being on my thesis defense committee and providing me exceptional insights and advice; Shila Maghji, Michelle Cintron, James Ihn, Kidest Shenkoru, Zachery Corter, Paulette Louissaint for their kindest help with the administrative issues. I would also like to thank Keith Yeager and Arthur Autz for their advice and help in designing and fabricating my experimental setups.

Last, but not least, I would like to give my deepest thanks to my loving wife Tiffany and to my parents, who have always been there for me and supported me to live my life to the fullest. I could not have gone this far without their selfless support and unconditional love.

To my wife and my parents

for their unconditional love

Chapter 1. Overview

1.1. Background

1.1.1. Human bone and its hierarchy

The human skeleton is one of the most important systems that provides structural support and maintains body shape, protects the fragile organs enclosed in the body, and permits movement and locomotion. Bone is also a living system that constantly undergoes remodeling to replace old, damaged bone with new bone and changes shape in order to adapt to the biomechanical environment. Bone, as a tissue and an organ, is hierarchically structured, and its mechanical properties are essentially dictated by the composition and organization at various metric levels.

The bone hierarchical structures ranges from the molecular level to the organ level, as shown in Figure 1.1. At the macroscopic level, bone has two compartments: cortical, or compact bone, and trabecular, or cancellous bone (Cowin 2001). Cortical bone is this densely packed bone that constitutes the outer shell of most bones; it is mainly present in the shafts of long bones such as the femur and the tibia. This compartment makes up approximately 80% of the bone mass in the whole skeleton, yet it accounts for a much smaller surface area than trabecular bone (Bronner and Worrell 1999). Trabecular bone is less densely packed, consisting of interconnecting plates and rods that form a mesh-like structure. Trabecular bone is mainly found in the ends of long bones (inside the cortical shell) as well as in the vertebrae. Although overall the trabecular compartment makes up only roughly 20% of the bone mass, different skeletal sites have distinct proportions of the two bone compartments. For example, trabecular bone accounts for 75% of the bone mass in the vertebra, 50% in the femoral head, and only 5% in the radial diaphysis.

At the microstructure and sub-microstructure levels, cortical bone is composed mainly of primary and secondary osteons and interstitial bone, approximately 100-300 μm in size. Cortical bone is vascularized, and the pore that houses blood vessels is called a Haversian canal. Rings of lamellae – sheet-like bone made from highly aligned, mineralized collagen fibers – surround the Haversian canal to make up the basic structural unit of cortical bone called the osteon (3-8 layers of lamellae). Osteons are oriented with the long axis of the bone, and interstitial bone fills the spaces between these osteons. Trabecular bone is rather different. It is a honeycomb-like structure composed of interconnected trabeculae, 100~-150 μm in thickness. Trabecular packets formed at each cycle of remodeling form the basic unit of trabecular bone. Much like cortical bone, trabecular bone packets are also comprised of highly organized lamellae. Unlike the concentric arrangement in cortical bone, lamellae arrangement is parallel to the trabecular packets.

At the nanostructure and ultrastructure levels, bone primarily consist of the mineral hydroxyapatite and an organic matrix mostly made of type I collagen. The collagen molecules assemble into fibrils with specific periodical tertiary structure with holes in between. As mineralization occurs, the mineral crystallizes in plates shaped with thickness, length and width roughly at 2-3nm, 50nm, and 25nm, fills in the holes, and grows parallel to the long axes of the collagen fibrils. The whole mineralized matrix bundles together to form a collagen fiber. The two constituents – mineral and collagen – have distinct mechanical properties. However, the close interactions between them are the very fundamental basis which determines the mechanical characteristics of bone as a tissue and even a structure, including strength, stiffness, and toughness.

1.1.2. Bone growth, acquisition, and the mineralization process

During development, there are two main methods by which bones are formed: intramembranous ossification and endochondral ossification. The majority of cortical bone is formed by intramembranous ossification, including flat bones and the bones in the skull. This growth is initiated by mesenchymal cells that differentiate into osteoblasts (bone forming cells), which eventually deposit osteoid (unmineralized bone). Within the osteoid, spicules form to make trabecular bone. Cortical bone is formed when the spaces between the trabeculae are filled the lamellar bone to form osteons (Cowin 2001).

Endochondral ossification forms the majority of long bones as well as trabecular bone. This method of growth is initiated by chondrocytes proliferating and depositing a matrix. Cartilage cells in this matrix calcify to form a primary ossification center. At these centers, osteoblasts secrete osteoid and trabecular bone is formed. Blood vessels penetrate the remaining cartilage, and secondary ossification centers are formed. Eventually, in these secondary centers, the cartilage is reduced to thin growth plates where longitudinal bone growth occurs. Finally, at maturity, these growth plates fuse and the remainder of the cartilage is mineralized (Mackie, Ahmed et al. 2008).

Closely linked with the processes of bone growth is bone modeling, which controls the outer shape and size of the bones as well as the shape and size of the inner cavities. In this process, bone formation by the osteoblasts occurs independently of osteoclasts on separate bone surfaces. The majority of modeling occurs during growth in the form of periosteal apposition in conjunction with endosteal resorption, resulting in bones with larger cross-sectional areas and only minimal changes in cortical thickness (Duan, Beck et al. 2003, Kontulainen, Macdonald et

al. 2006). After maturity, some periosteal bone modeling continues throughout life, particularly in men, which is observed as an increase in bone diameter with age (Duan, Beck et al. 2003).

In contrast, bone remodeling is a continuous process that occurs throughout life on the trabecular, endocortical, and intracortical surfaces. It is composed of resorption and formation phases coupled to the same site in bone, and maintains an approximately constant bone mass. By this process, bone can adapt and repair microdamage (Parfitt 2002).

Bone tissue consists of 65% mineral, 35% organic matrix, cells, and water. The organic matrix is dominated by Type-I collagen, and the mineral is in the form of hydroxyapatite located within and between collagen fibers. Bone mineral provides mechanical rigidity and load-bearing strength to bone, whereas the organic matrix provides flexibility and elasticity. When new bone is formed, the bone osteoblasts secrete and deposit the collagen matrix first, which then gradually mineralizes. The mineralization process starts with a rapid increase in the mineral content during the first few days up to 70% of the final level, a phase typically referred to as the primary mineralization and followed by a slow and gradual maturation of the mineral content, referred to as secondary mineralization. The mineral content of bone matrix is not uniform because bone packets are deposited at different moments in a remodeling cycle, and the mineral content depends on the time of its deposition. Therefore, the average mineral density and the heterogeneity of mineralization are both important factors in determining fundamental mechanical properties of bone tissue, which also affect strength on the whole-bone level.

1.1.3. Bone strength determinants

Fracture occurs when external loads exceed bone's capacity to withstand them. Bone strength, or the capability to resist fracture, is mainly determined by the bone quantity and bone quality. Bone quantity, characterized by bone mass, simply means how much bone there is.

Clinically, bone mass is used as the key index to diagnose osteoporosis and assess risk fracture. The most commonly used tool is dual-energy x-ray absorptiometry (DXA), which allows clinicians to obtain a measure of areal bone mineral density (aBMD; g/cm^2). DXA uses x-rays at two different energies to distinguish bone and soft tissue. It can be used in vivo at all sites within the body. DXA-measured aBMD is the clinical standard as a surrogate for bone strength, and a decrease in aBMD is associated with a decrease in bone strength (Bouxsein, Coan et al. 1999). Bouxsein and colleagues also indicated that aBMD predicts about 66-74% of the variance in bone strength (Bouxsein, Coan et al. 1999). However, this bone mass measurement is limited because aBMD is a two-dimensional rather than a volumetric measure of bone density, and is therefore affected by both the size and the orientation of bone. This limitation may explain why more than 80% of fractures occur in individuals without osteoporosis as defined by aBMD alone (Stone, Seeley et al. 2003). DXA is also limited by its inability to distinguish between cortical and trabecular bone or to reveal microarchitecture.

It is, therefore, becoming apparent that factors other than aBMD contribute to fracture risk and determine bone strength and a more recent focus has been shifted to bone quality. Bone quality is mainly characterized by cortical and trabecular microstructure on the microscopic level and the intrinsic material properties of bone on the tissue level. Thanks to the emergence of high-resolution computed tomography, detailed microstructures have been able to be characterized by morphological parameters describing scale, such as bone volume fraction and thickness; orientation, such as structure anisotropy; and topology, such as connectivity (Wehrli 2007). Bone microstructure has been strongly associated with fracture risk and bone strength. On the microstructural level, fracture risk is linked with this loss of bone, or osteoporosis that may include thinning and a decrease in the number of trabeculae (Gourion-Arsiquaud, Faibish et al.

2009), as well as increased cortical porosity and decreased cortical thickness (Stein, Kepley et al. 2014). Osteoporosis and increased fracture risk can affect many populations. The most common observance is still in postmenopausal women (Melton, Chrischilles et al. 1992), but osteoporosis also occurs in pre-menopausal women (Gourlay and Brown 2004) and men (Bilezikian 1999). Following menopause, there is a decrease of estrogen in the body, which causes decreased bone turnover and increased bone loss (Jarvinen 2003).

Besides microstructure, the intrinsic bone material property is considered to be an important determinant of bone strength. The intrinsic bone material properties include: (1) the material properties of the constituent bone tissue determined by the composition and organization of the primary nanoscale constituents, mineral and collagen, and (2) microdamage and microstructural discontinuities such as lacunae or the submicron gaps between lamellae. The composition and organization further include the orientation of crystal size, maturation and orientation; collagen ultrastructures, such as orientation and cross-linking of collagen fibers (Fonseca, Moreira-Goncalves et al. 2014, Georgiadis, Guizar-Sicairos et al. 2015); and the measurement of mineral and collagen content. It is known that the heterogeneous mineralization distribution helps hinder a micro-crack from propagating further by increasing the energy dissipation, therefore increasing the toughness (van der Linden, Birkenhager-Frenkel et al. 2001, Ettinger, Burr et al. 2013, Milovanovic, Rakocevic et al. 2014). The accumulation of microdamage caused by long term usage of anti-resorptive drugs, such as bisphosphonates, has been considered an important explanation for the occurrence of atypical fractures (Chiang, Zebaze et al. 2013, Iwata, Mashiba et al. 2014). Quantitatively, for two structures with global uniform and isotropic material properties, a structure with higher material properties proportionally has higher stiffness and better strength. However, when the tissue material

property is not uniform or not isotropic, as in trabecular bone, there is a gap in the knowledge of the comprehensive tissue material properties, discussed in chapter 3, and how they contribute to whole bone stiffness or strength, discussed in chapter 4.

1.1.4. Basic mechanics of bone

Structural and microarchitecture indices have been shown to be useful surrogates for bone strength and, in some cases, are associated with fracture outcomes. Since fractures occur when the applied load exceeds the mechanical strength (Keaveny and Bouxsein 2008), it is important also to provide estimates of bone strength to assess fracture risk.

Here is an illustration of the basics of bone mechanics. Force represents an action on an object and is composed of a magnitude and a direction. In order to characterize the mechanical properties of a material, force can be plotted against the material's displacement under a given load, and this relationship depends on the structure (i.e. size and geometry) of the material (Figure 1.2). Stress is a force acting over a specific area with a unit of measure of either pascals (Pa) or newtons per square meter (N/m^2), while strain is a dimensionless measure of the deformation per unit length due to a force. Unlike a load-displacement plot, a plot of stress versus strain does not depend on the structure of the object in question.

Various properties can be used to characterize a material and its resistance to fracture. The slope of the load-deformation plot in the linear region represents the stiffness of the material (Beer 2006). The equivalent region from the stress-strain plot is also known as the Young's, or elastic, modulus. Other intrinsic properties include the point where the line transitions from the elastic to the plastic region, known as the yield stress, and the highest point on the curve before fracture, which is the ultimate or maximum stress. The toughness of a material is the area under the entire curve and represents the amount of energy the material can absorb before complete

failure occurs, while the resilience of a material is the area under the curve up to the yield stress and represents that energy that can be absorbed before yielding occurs (Beer 2006).

Mechanical testing can be used to experimentally determine mechanical properties of an object. These tests can be either force- or displacement-controlled, where one of the variables is applied, and the other is measured to produce a force-displacement plot. Many considerations such as temperature, hydration, and storage must be addressed when performing mechanical testing in order to not alter the mechanical properties. For example, compared to a hydrated bone (which best captures *in vivo* conditions), a dry bone may have increased Young's modulus but decreased toughness (Cowin 2001). Furthermore, the loading configurations lead to specific fracture patterns: compression causes oblique fractures, tension causes transverse fractures, and torsion produces spiral fractures. The actual loads involved in fracture can be complex in nature and may represent a combination of these conditions. Bending, which is commonly observed in a sideways fall on the hip, is a combination of both tension and compression which produces a transverse fracture with a small fragment on the concave side (Einhorn 1992).

Micro finite element (μFE) analysis can also estimate the elastic and yield properties of bone by simulating a mechanical test on a specimen-specific FE model. Recent advances in high-resolution imaging technologies now allow for a reconstruction of the three-dimensional (3D) trabecular microstructure at 10-80 μm voxel size, which is sufficient to capture detailed trabecular features. The details on the assessment of bone strength using high-resolution image-based μFE analysis will be discussed in Chapter 1.4.

The mechanical properties of bone characterize bone's behavior under mechanical loads and are important quantitative factors for assessing the risk of fractures. There are two levels of mechanical properties: apparent level, which refers to the mechanical behavior at the continuum

level of the whole bone specimen; and tissue level, which refers to those at the individual trabeculae or osteon level.

1.2 Characterization of trabecular plate and rod microstructure

1.2.1 Trabecular morphology and μCT

Trabecular bone microstructure is a complicated, interconnected network composed of plate-like and rod-like trabeculae. Due to the high porosity and high surface-to-volume ratio, trabecular bone is much more metabolically active (more bone remodeling) and prone to metabolic disease. In most cases, plate-like trabeculae make up the largest proportion of trabeculae in healthy bone. With aging and the development of osteoporosis, however, there is a drastic change in the trabecular bone structure from plate-like to more rod-like. These trabecular plates and rods are distributed distinctly along different anatomic directions of the skeleton. These individual trabeculae are approximately 100-200 μm in thickness, and it can be up to ~2mm in length in humans.

To evaluate this complex bone morphology and microstructure, μCT has become the gold standard. With a resolution as high as several μm, μCT is a non-destructive tool capable of characterizing the detailed trabecular microstructure. It is an x-ray-based modality that obtains projections around the subject being scanned to produce a three-dimensional image (Dowsett 2006). In most current μCT scanners, the source and detector move around the subject, and the emitted x-rays are collected from various views. As the x-rays pass through the subject, the photons are attenuated to different extents. This attenuation depends on the linear attenuation coefficient of the material through which the x-rays are passing. The projections are then reconstructed into two-dimensional slice images where the attenuation is represented as a CT number in Hounsfield units (Dowsett 2006). Briefly, image reconstruction of the CT projections

is most commonly performed using filtered back projection. This method first filters the projections and then smears the projections across the path of the x-ray. When multiple projections are included, the high and low attenuation locations become apparent in the image (Dowsett 2006). While not reviewed in this thesis, it is important to note that there are other image reconstruction methods less commonly used in medical imaging, including the Fourier transform and algebraic reconstruction (Pan, Sidky et al. 2009).

μCT allows for direct 3D measurements of trabecular morphology. Bone volume fraction (BV/TV) is defined as the bone tissue volume divided by the total volume of the sample region. Trabecular thickness (Tb.Th) is calculated based on a distance transformation and maximal sphere fitting in the trabeculae. Trabecular number (Tb.N) is defined as the inverse of the mean distance between the mid-axes of the trabeculae. Similarly, trabecular spacing (Tb.Sp) is calculated based on maximal sphere fitting in the marrow space between trabeculae. Structure model index (Rahman, Cibere et al.) was developed to characterize the likeness of a 3D structure towards an ideal plate (SMI=0) or an ideal rod (SMI=3). The degree of anisotropy (DA) indicates how the trabecular network is oriented. Finally, connectivity density (Conn.D) describes the connectivity level of the structure normalized by the size of the specimen.

Besides morphology, μCT is also capable of measuring volumetric bone mineral density (vBMD; g/cm^3). Furthermore, the measurements of bone tissue mineralization can be accurately estimated by calibrating the x-ray attenuation with the density of hydroxyapatite phantoms. Accurate measurements of the morphology and mineral density provide a direct estimation of bone strength using μCT-based FE. However, the radiation associated with regular μCT is too high to enable a direct clinical *in vivo* scan. The emergence of clinical μCT or high-resolution quantitative peripheral computed tomography (HR-pQCT) overcomes this issue,

enabling a fast *in vivo* imaging of the trabecular and cortical microstructure at distal radius and distal tibia, but at the expense of resolution. Although it only produces an isotropic voxel size of ~60 μm, it works using the same principles as μCT, provides the same morphological measurements, and can still capture changes in trabecular microstructure with disease and drug treatments (Nishiyama, Cohen et al. 2014, Stein, Kepley et al. 2014, Agarwal, Rosete et al. 2016, Wang, Stein et al. 2016, Zhou, Zhang et al. 2016).

1.2.2 Individual Trabecula Segmentation (ITS)

μCT or HR-pQCT morphological analysis only accounts for the overall bone structure; it doesn't provide detailed analyses of trabecular plates and rods. Although SMI somewhat indicates if a trabecular region is more plate-like or rod-like, it does not explicitly quantify the amount of trabecular plates and rods, let alone provide direct access to characterize a particular plate or rod. However, SMI has shown that a radical change of the trabecular structure from plate-like to rod-like is a major hallmark of aging or osteoporosis (Ding and Hvid 2000), suggesting the necessity of a tool to characterize the plate- and rod-based morphology of trabecular bone structure. Liu et al. applied digital topological analysis to trabecular bone μCT images and developed an individual trabeculae segmentation (ITS) technique that decomposes a 3D trabecular network into individual trabecular plates and rods, allowing separate evaluation for each trabecular element (Liu, Sajda et al. 2008). The characterization of trabecular type is based on skeletonization and classification algorithms developed by Saha et al. (Saha and Chaudhuri 1996, Saha, Chaudhuri et al. 1997). The technique first applies an iterative erosion process called skeletonization that essentially peels off the bone voxels layer by layer until the topology or shape of a trabecular microstructure cannot be maintained anymore if going further. The outcome of this transformation is a minimal representation of the trabecular bone microstructure

by one voxel thick surfaces or curves (Saha, Chaudhuri et al. 1994). Then, through digital topological classification, each voxel is identified as belonging to either a plate (surface) or a rod (curve). Lastly, volumetric reconstruction of the trabeculae – a layer-by-layer dilation process of the skeletal voxels – was performed (Liu, Sajda et al. 2006). After the same number of iteration times, each bone voxel is labeled as belonging to an individual trabecular plate or rod. Through this process, the volumetric parameter to describe trabecular bone microstructure is calculated.

ITS not only provides the classification on trabecular type, but it also quantifies the orientation of each trabecular plate and rod. For a plate, the normal direction is obtained as the surface normal to a plane representing the surface skeleton using a least-square fitting algorithm. For a rod, the orientation is quantified from 3D principal component analysis on its curve skeleton. ITS morphological analysis has been validated on both μCT and clinical HR-pQCT images and applied extensively to study bone diseases and the influence of treatments(Liu, Sajda et al. 2008, Liu, Zhang et al. 2010, Liu, Stein et al. 2011, Nishiyama, Cohen et al. 2014). Due to the powerful capacity of ITS, any individual trabecula within the complicated trabecular bone structure can be characterized into a particular trabecular type with an anatomic orientation, which makes the investigation of the anisotropy of trabecular bone possible. This is one key objective of this thesis.

1.3 Characterization of intrinsic tissue material properties

1.3.1 Depth-sensing indentation and tissue modulus

The tissue modulus of bone, one of the most important intrinsic tissue material properties, has been measured by many experimental methods, including buckling experiments of dissected single trabecula, bending tests, ultrasonic techniques, back-calculations from FE analysis, and indentation techniques. These methods have yielded somewhat inconsistent measurements of the

tissue modulus in trabecular bone and cortical bone. However, in general, the tissue modulus of trabecular bone is ~20% lower than that of cortical bone. The emergence of the depth-sensing indentation technique has offered a truly reliable and convenient method of characterizing tissue material properties.

Traditional indentation techniques measure the hardness of bone tissue, which is defined by a certain force over a projected contact area between the indenter and the testing material. The peak load and the projected contact areas are measured separately by a load cell and high-resolution microscopy. The measurement of hardness highly depends on the shape and size of the indenter as well as the loading profile, and the results cannot be compared to those obtained by a different experimental setup. Thanks to the fast and advanced development in the precision of analog and digital devices at the end of the 20th century, the creation of ultra-high resolution and precision mechanical loading systems were made possible. In addition, the emergence of depth-sensing indentation and analytic methods for calculating modulus solely based on the associated load-displacement curve added the ability to directly measurement Young's modulus (Oliver and Pharr 1992). The unloading portion of the load-displacement curve can be perfectly fit by a power law equation. The initial unloading is assumed to be purely elastic, and the slope at that point is the stiffness. Modulus can be calculated based on a function of the stiffness and contact area (Oliver and Pharr 1992). Indentation has been applied to test bone tissue (Zysset, Guo et al. 1999, Hoffler, Moore et al. 2000, Hoffler, Moore et al. 2000, Hoffler, Guo et al. 2005, Faingold, Cohen et al. 2013) for more than 20 years. Tissue mechanical properties ranging from different loading sites, including the femur (Zysset, Guo et al. 1999) and spine (Wolfram, Wilke et al. 2010, Dall'Ara, Karl et al. 2013) and different bone units, including osteons (Carnelli, Vena et al. 2013, Korsa, Lukes et al. 2015) and lamellae (Faingold, Cohen et al. 2012, Korsa, Lukes et

al. 2015), have been well characterized by indentation. In particular, indentation can be performed on wet bone tissue that mimics a more physiological condition (Hengsberger, Kulik et al. 2002, Hoffler, Guo et al. 2005). Indentation has also been used to measure the trabecular bone modulus in different cross-sections in an attempt to study the anisotropy. However, due to a lack of quantification of the angle of the cross-section direction and an inability to identify trabecular types, the existing findings are incomplete. Therefore, in this thesis, depth-sensing indentation, with its high spatial resolution, is used for tissue modulus characterization of individual trabeculae.

1.3.2 Heterogeneous distribution of tissue mineralization

A heterogeneous distribution is one of the basic features of intrinsic material properties. The non-uniform tissue mineralization in trabecular bone tissue is a result of constant bone remodeling and dynamic mineralization kinetics in newly formed bone packets. During remodeling, the surface layer of trabeculae is more frequently remodeled, while the tissue in the center of trabeculae or interstitial bone is less frequently renewed (Birkenhager-Frenkel, Nigg et al. 1993, Boyde, Elliott et al. 1993) and usually more highly mineralized (Roschger, Fratzl et al. 1997, Camacho, Rinnerthaler et al. 1999). During mineralization, 70% of the total mineral content is deposited in new bone tissue in roughly two days, and the remaining mineralization continues at a slower rate for years before the tissue gets resorbed (Grynpas 1993). Advanced imaging techniques, such as synchrotron radiation μCT (SRμCT) and quantitative backscattered electron imaging (qBEI) have been applied to study the tissue mineralization distribution of trabecular bone. Wang et al. studied the average TMD of trabecular elements using SRμCT and μCT and discovered morphology- and orientation-based TMD variations. Roschger et al. studied the heterogeneous mineralization distribution and confirmed that newly formed bone packets on

the surface exhibit much lower mineral concentration compared with old bone tissue in the center of trabeculae. They further quantified the heterogeneity in mineralization by a distribution of the mineral content characterized by the grey scale value of qBEI pixels within a region of interest, where the average mineralization density and degree of heterogeneity characterized by the width of distribution are the major indexes. Normal healthy adults were found to have a characteristic TMD distribution regardless of gender, age, or race (Roschger, Gupta et al. 2003). Adults with bone metabolic diseases and certain treatments, such as osteomalacia, osteoporosis, and treatment with bisphosphonates, were shown to possess distinct deviations from healthy adult TMD distributions, with different average mineralization density and degree of heterogeneity (Roschger, Paschalis et al. 2008).

The heterogeneous distribution contributes to bone toughness. But how this heterogeneous distribution, especially when deviated from a normal TMD distribution, affects the stiffness of bone is unclear. It is also unknown whether the mineralization varies in trabecular types and orientations between healthy and diseased individuals, and whether this could contribute to the pathophysiology of the disease. In this thesis, tissue mineralization will be studied alongside tissue-level mechanical properties based on μCT-derived TMD.

1.3.3 Diseases or treatments affecting bone material properties

There are many diseases that can affect bone mineralization and collagen formation and therefore further affect the mechanical properties of bone tissue. These diseases can manifest as bone mineral homeostasis disorders, an imbalance of bone remodeling, or disorders of the collagen or mineral building blocks. For example, both rickets and osteomalacia are a result of impairment in mineral deposition (Ryan, Anderson et al. 2013); hyperparathyroidism, with excessive secretion of parathyroid hormone, leads to excessive bone resorption (Fraser 2009).

Another condition, Paget's disease, is characterized by a rapid bone turnover that leads to a disorganized pattern of lamellar and woven bone (Ralston, Langston et al. 2008). Osteogenesis imperfecta is caused by mutation of type I collagen genes that leads to a defect in the bone matrix, with over-mineralization and highly brittle bone (Basel and Steiner 2009). Lastly, the most prevalent bone disease – osteoporosis – is usually associated with increased bone resorption that results in an increased heterogeneity of bone mineralization. Though the mechanisms of these diseases have been established, how the alterations in mineralization or collagen affect the tissue mechanical proprieties have barely been studied. In this thesis, two prevalent bone related diseases were selected to study alterations of the mineralization and tissue material properties, osteoarthritis (Bouxsein, Coan et al.) and adolescent idiopathic scoliosis (Bacchetta, Boutroy et al.).

OA characterized by articular cartilage degradation and bone sclerosis, which presents as dramatically higher bone volume fraction as well as BMD. When characterizing the bone tissue that constitutes these rapid changes in structure, it is difficult to determine whether changes in mineralization are caused by a disturbed balance between biological processes or by a change in the loading environment. No matter the root cause, it would be interesting to know how and if the changes in tissue composition affect the tissue mechanical properties in OA models, particularly as models evolve to better describe the influence of the mechanical properties and loading environment on the biological activity in OA.

Conversely, AIS patients have been reported to have lower BMD and deranged trabecular distribution compared to aged-match controls (Cheuk, Zhu et al. 2015). Not only could scoliosis be attributed to a more compliant tissue material, but the adolescent bone tissue is likely also

different from the adult bone. A more detailed discussion of the tissue material properties in the two diseases will be discussed in detail in Chapter 5 and 6.

1.4 Finite element modeling of human bone

1.4.1 High resolution image-based finite element modeling

Finite element analysis, as a substantial alternative to destructive mechanical testing, can be applied to predict or examine bone mechanical properties. With the emergence of high-resolution 3D imaging techniques like μCT, bone microstructure can be accurately visualized at high resolution, which further enhances the precision of FE modeling. Starting with a 3D μCT image, a μFE model incorporating specimen-specific microstructural parameters can be generated based on a direct conversion of each bone voxel to an 8-node brick element. The μFE modeling approach has been shown to predict the bone mechanical properties accurately and is now a prevailing method of evaluating bone mechanical properties. Initially, μFE analysis was only applied to a simple linear simulation of trabecular bone in order to evaluate the elastic properties of bone (Hollister, Brennan et al. 1994). Subsequently, more complicated material properties and nonlinear algorithms were incorporated into FE analysis to mimic the failure behavior of bone tissue under different loading profiles and to predict the yield strength of trabecular bone (not just stiffness) (Niebur, Yuen et al. 2001, Bevill, Eswaran et al. 2006). For example, nonlinear μFE analysis was employed to examine the failure initiation and propagation across a whole proximal femur at a sideways fall configuration, and the load sharing between trabecular and cortical bone at the femoral neck provided additional insights on the relative contributions to support between the two different types of bone (Nawathe, Akhlaghpour et al. 2014, Nawathe, Nguyen et al. 2015). Clinically, the emergence of HR-pQCT makes the direct assessment of a patient's bone stiffness and strength through FE analysis possible. Validation

studies have demonstrated HR-pQCT-based μFE predicts the stiffness measures highly comparable to the measures by mechanical testing and μCT-based μFE (Macneil and Boyd 2008, Liu, Zhang et al. 2010, Zhou, Wang et al. 2016). Furthermore, the predictions of stiffness by μFE analysis on standard HR-pQCT scanning regions correlate highly with the predictions on other regions (Liu, Wang et al. 2013), and are a reliable factors to indicate osteoporotic fracture risk in postmenopausal women (Boutroy, Van Rietbergen et al. 2008, Vilayphiou, Boutroy et al. 2010). All these studies support the promise of μFE analysis to become a powerful tool for the clinical assessment of bone strength and fracture risk.

1.4.2 Homogeneous and heterogeneous finite element models

Despite the efforts put forth to ensure μFE analysis predicts the mechanical properties of human bone structure as accurately as possible, the fundamental mathematical representation of the underlying bone tissue is still rather simplified, and the non-uniform bone tissue material properties are mostly excluded from current models due to the lack of a comprehensive understanding of intrinsic bone tissue material properties. Instead, bone tissue has routinely been assumed to be an isotropic material with a homogeneous tissue modulus. However, for patients with certain diseases and treatments that have a high impact on bone mineralization, such as chronic kidney disease or long-term anti-resorptive treatments, the resultant high extent of changes in bone tissue mechanical properties may have a profound influence on the apparent mechanical behavior. Therefore, homogeneous finite element models might not accurately predict bone mechanical properties in these scenarios.

There have been attempts at understanding how the inclusion of heterogeneity affects FE model predictions. Several studies suggest that the incorporation of mineral heterogeneity results in an underestimation in the predicted stiffness. Jaasma et al. used a spatially heterogeneous

tissue modulus proportional to TMD based on μCT to model uniaxial compression of human femoral neck and vertebral body trabecular bone, and they found that the apparent modulus decreased and percentage of failed tissue increased nonlinearly as the coefficient of variation (COV) of the tissue modulus increased, indicating that the degree of heterogeneity can have substantial biomechanical effects on both the linear and nonlinear behaviors(Jaasma, Bayraktar et al. 2002). Nevertheless, the extent of this reduction was inconsistent, varying from 2% to 20% depending on the mineralization distribution model used in those studies (Bourne and van der Meulen 2004, Chevalier, Pahr et al. 2007, Harrison, McDonnell et al. 2008, Gross, Pahr et al. 2012). In a recent clinical study on the effects of teriparatide treatment on premenopausal women with idiopathic osteoporosis, heterogeneous FE models were used to account for the large amount of newly formed but not fully mineralized bone. The comparison between the homogeneous and heterogeneous models indicated the latter was more sensitive in detecting subtle improvements in stiffness and failure load (Nishiyama, Cohen et al. 2014).

Despite the attempts to simulate the contribution of heterogeneity to whole bone level bone mechanics(van der Linden, Birkenhager-Frenkel et al. 2001, Jaasma, Bayraktar et al. 2002, Bourne and van der Meulen 2004), most studies assume a random scaled correlation between the TMD and tissue modulus. Wolfram et al. incorporated nanoindentation-tested specimen-specific moduli to their FE analyses and showed a slightly better correlation with mechanical testing compared to a global modulus FE model (Wolfram, Wilke et al. 2010). However, only homogeneous FE analysis was performed. Trabecular bone is likely to possess other non-uniform material properties, such as anisotropy, for the reason that the trabecular bone tissue is essentially comprised of highly organized lamellar layers similar to cortical bone, the anisotropy of which has been widely studied. From a quantitative point of view, the predicted μFE results

are critically dependent on the chosen trabecular and cortical bone tissue properties. None of the studies above have systematically investigated the contribution of tissue material properties to whole bone mechanics based on mechanically-tested tissue modulus inputs, which is one of the motivations for this thesis.

1.5 Scientific and Clinical Motivations

Tissue material properties have emerged to be major determinants of bone strength and resistance to fractures. Spatially heterogeneous bone tissue moduli impede cracking propagations and contribute to bone toughness (Tai, Dao et al. 2007). However, how the tissue material properties contribute to whole bone stiffness (the ability to resist deformation) and strength (the maximum loading capacity), which are directly related to the risk of fractures, is not clear. A comprehensive study of how tissue material properties relate to apparent level mechanical behavior, whether the contribution is small or large, would provide directions for improving current fracture risk assessment methods, evaluating new therapies for bone metabolic and remodeling disorders, and evaluating drugs for more specific and targeted functionality. The tissue-level and micro-level mechanics of trabecular bone are not well studied. Morphologically, trabecular bone grows in different anatomic directions. Although more trabecular plates tend to align in the principal trabecular direction and adapt to load, the mineralization in transversely aligned plates was found to be higher (Liu, Sajda et al. 2008, Wang, Kazakia et al. 2015). Trabecular rods are distributed mainly in the transverse direction, but the mineralization is similar in all directions (Liu, Sajda et al. 2008, Wang, Kazakia et al. 2015). On the lamellar level, mineralized collagen fiber bundles align in a highly organized manner, and, especially in cortical bone, the collagen fibers spirally align along an osteon uniformly (Wagermaier, Gupta et al. 2006, Faingold, Cohen et al. 2013). As a result, the cortical bone possesses anisotropic

mechanical properties, i.e., the Young's modulus in the axial direction is higher than that in the lateral direction (Swadener, Rho et al. 2001, Reisinger, Pahr et al. 2011, Carnelli, Vena et al. 2013). Although the trabecular bone is also comprised of lamellar layers, the anisotropy of trabecular bone has never been studied due to the irregular shapes and distinct orientations of individual trabecula. It is expected that trabecular bone would also have a direction-related pattern of mineralization and mechanical properties. Because of the lack of knowledge at the tissue level, μCT-based FE models do not account for tissue material properties. Clinical μCT-based μFE analysis is a noninvasive way to accurately assess bone stiffness and bone strength (Liu, Zhang et al. 2009, Christen, Melton et al. 2013). The accuracy of clinical μCT-based μFEA measurements has been demonstrated in several validation studies, and these measurements have also been utilized in clinical studies to characterize differences in bone mechanical competence between subjects with or without osteoporosis and with or without a history of fractures (Boutroy, Van Rietbergen et al. 2008, Vilayphiou, Boutroy et al. 2010), suggesting the promise of μCT-based μFE analysis to become a powerful tool for the clinical assessment of bone strength and fracture risk. However, the tissue modulus in these models is empirically assumed to be a constant. Such a model might deliver reliable predictions within a group that has healthy bone and is in similar age. However, when the mineralization or the distribution of trabecular types and orientations is significantly altered, current models might not be comprehensive enough. Thus, testing the models with disease-altered mineralization and trabecular distribution can provide fundamental scientific insights to improve the understanding of tissue material contributions to whole bone mechanics.

1.6 Specific Aims and Organization

1.6.1 Specific Aims

Hypothesis 1. TMD-dependent mechanical properties of individual trabecular plates and rods do not differ in anatomic directions but differ in individual trabecular direction

Aim 1a. Develop and calibrate a micro-indentation technique to accurately measure bone tissue modulus.

Aim 1b. Investigate the relationships between TMD and tissue modulus with different trabecular types, anatomic directions, and indentation directions.

Hypothesis 2a. Inclusion of experimentally obtained anisotropic material properties does not change the prediction power of a voxel-based finite element model

Hypothesis 2b. Inclusion of experimentally obtained anisotropic material properties increases the accuracy of prediction of a voxel FE model

Aim 2a. Develop a heterogeneous and anisotropic FE voxel model to assess trabecular bone mechanics.

Aim 2b. Compare the stiffness predicted by different FE models and mechanical testing to evaluate the contribution of an anisotropic tissue modulus to apparent level stiffness.

Hypothesis 3. Altered mineralization distribution will affect the tissue level material properties and the associated apparent level bone mechanics

Aim 3**a.** Measure and compare the TMD and modulus distributions of adolescent idiopathic scoliosis and osteoarthritis trabecular samples and compare normal controls.

Aim 3**b.** Compare the predicted apparent level bone stiffness between normal and diseased bone.

1.6.2 Organization

This thesis is organized based on a framework to address the specific aims above. The development and calibration of the micro-indentation technique to test the tissue modulus of trabecular bone is discussed in Chapter 2. The heterogeneous and anisotropic trabecular bone tissue material properties are discussed in Chapter 3. The contribution of heterogeneous and anisotropic trabecular bone tissue material properties to apparent level bone mechanics is

discussed in Chapter 4. Altered mineralization and the effect on associated apparent level bone mechanics in metabolic bone diseases are discussed in Chapters 5 and 6.

In Chapter 2, the motivation for developing a micro-indentation technique to characterize bone tissue modulus is introduced along with the mechanics principles behind the technique. Then, detailed descriptions of the setup and the specifications of the micro-indentation device are provided along with an evaluation of the performance of the system. Lastly, the calibration of the system by a standard material (fused silica) and the accuracy of the system is described.

In Chapter 3, in human trabecular bone from multiple loading sites, trabecular plates and rods in different anatomic directions were identified by μCT ITS and tested by micro-indentation in both axial and lateral cross-section directions. The tissue modulus of the plates and rods were compared in different anatomic directions as well as cross-section directions. Lastly, the tissue modulus was correlated with the corresponding TMD on a point-to-point basis.

In Chapter 4, a voxel-based finite element model incorporating the experimentally obtained anisotropic and heterogeneous tissue modulus input was created and validated. The apparent level mechanical properties of a set of proximal tibia, femoral neck, and greater trochanter trabecular bone cores were analyzed by the aforementioned FE model and a conventional homogeneous model. The simulated stiffness and yield strength were also compared with gold standard mechanical testing measurements.

In Chapter 5, trabecular bone samples from AIS patients were tested by indentation, and the bone tissue material properties were compared with the corresponding non-AIS control group. Furthermore, μFE was used to characterize the differences in apparent level mechanical properties between control and diseased bone.

In Chapter 6, trabecular bone samples from regular OA knees and diabetic OA knees were tested by indentation, and the bone tissue material properties were compared with the corresponding normal control group. The microstructure of the different groups was analyzed and compared as well. In addition, μFE was used to characterize the differences in apparent level mechanical properties between control and diseased bone.

Finally, Chapter 7 summarizes the key findings from this thesis research and provides suggestions for future studies.

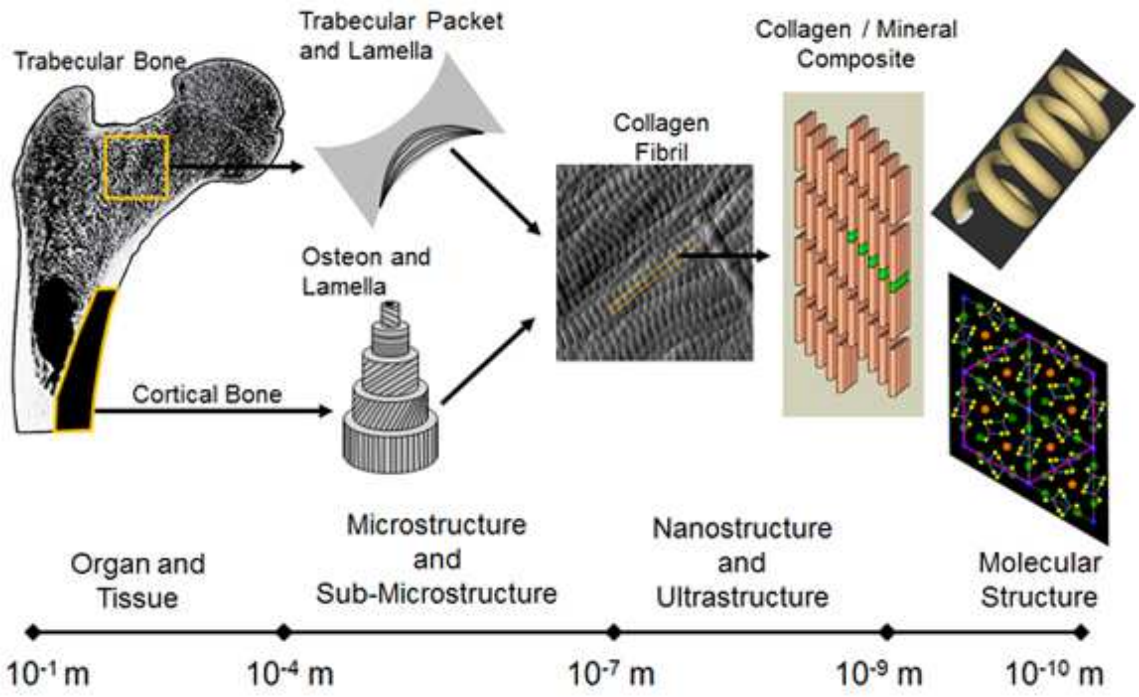

Figure 1.1. Schematic diagram of bone hierarchical levels of organization (adapted from http://www.iupui.edu/~bbml/Figures/hier.jpg).

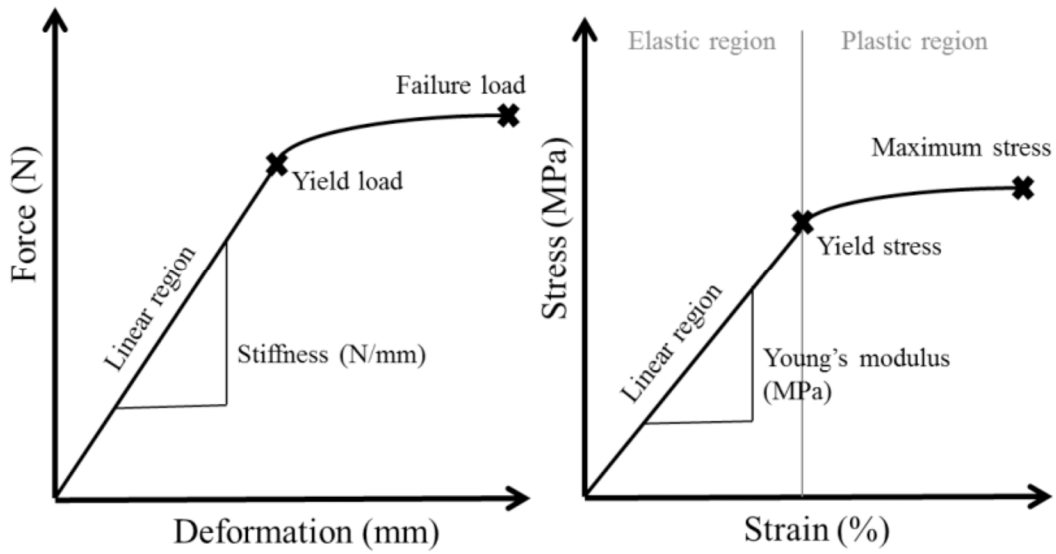

Figure 1.2. Load-deformation plot (left) and stress-strain plot (right) depicting the various properties that can be used to characterize a material.

Chapter 2. Development and calibration of a micro-indentation technique to fast and accurately measure tissue modulus

2.1. Introduction

Indentation is the most direct mechanical testing method for measuring the material properties of a given sample on a smaller scale. Traditionally, micro-indentation referred to a micro-hardness test that measures the hardness of a material with low applied loads. The hardness is defined as the pressure applied over the contact area between the indenter and the material being tested. However, there are two major limitations with this method. First, it requires a separate imaging measurement of the residual indents. As the testing scale goes smaller and smaller, the requirement for the resolution and accuracy of the imaging technique becomes impractical. Second, the measurements highly depend on the size and geometry of the indenter as well as the applied force; therefore the results from different indenters are not comparable.

Thanks to the development of instruments measuring displacement and force and linear actuators with more precision in the late 1980s, the techniques for probing the mechanical properties of a material were made possible on a submicron scale. The technique, called depth-sensing indentation, determines the Young's modulus and hardness of a tested specimen based only on the simultaneously acquired displacement and load data for a single cycle of loading and unloading. The development was initially used in quality control for the thin film of silicon wafers. With improved methods introduced by Oliver and Pharr in 1992, the technique was widely adopted in other industries as well. It has been two decades since researchers started to use depth-sensing indentation on bone tissue. However, though commercial products can achieve

an ultrahigh load and displacement resolutions at 0.3μN and 0.16 nm, these machines are more suitable for testing the material properties of an object with dimensions on order of several microns, such as the lamellae of osteons, considering the number of tests necessary to truly reflect the overall material property of the whole object. Besides, each cycle of test takes roughly ten mins, which is impractical to be used for the characterization of the tissue material properties of an individual trabecular plate or rod with a dimension of more than 100 μm to several mm. As an additional consideration, in order to correlate Young's modulus with a co-localized TMD measurement to provide a quantitative description of the tissue modulus inputs for μCT-based μFE analysis, the scale of the indenter should be on the same scale of the resolution of μCT, which is ~10 μm. Therefore, in this thesis, a custom made micro-indentation machine was built to employ the same depth-sensing principle to measure the Young's modulus of trabecular plates and rods efficiently and accurately on the desired scale.

2.2. Mechanical theory of depth-sensing indentation

2.2.1. Depth-sensing indentation theory and assumptions

The indentation theory was originated from the elastic contact problem. Boussinesq computed the stress and displacement in an elastic object probed by a rigid and axisymmetric indenter using potential theory(Sneddon 1965, Sneddon 2008). Sneddon then derived the Boussinesq solution and further provided a broad relationship between displacement, load and the contact area for a punch of arbitrary profile that can be mathematically described (Sneddon 1965). The theoretical foundation of the depth-sensing method lies on the critical assumption that the solutions for the elastic deformation of an irreversibly indented surface, meaning that the shape of the indent doesn't change, only the depth recovers, resembles those for an indented flat

semi-infinite half space (Figure 2.1). Simple solution for a flat punch loading on flat semi-infinite half surface is presented below. Based on the pressure distribution beneath the indenter, superposing the Boussinesq stress field can compute the stress field. For a rigid cylindrical flat punch, the pressure distribution of contact is

$$\frac{\sigma_z}{p_c} = -\frac{1}{2}\left(1-\frac{r^2}{a^2}\right)^{-\frac{1}{2}} \quad r \leq a \tag{2.1}$$

where σ_z is the principle stress in the loading direction on the axis of symmetry; p_c is the contact pressure beneath the indenter; a is the radius of the indenter. The deformation of the free surface beneath the indenter in the loading direction, U_z can be described as(Sneddon 2008)

$$\frac{U_z}{p_c} = \frac{1-\nu^2}{E}\, a\, \frac{\pi}{2}\,, \quad r \leq a \tag{2.2}$$

Note that $p_c = \frac{P}{\pi a^2}$, where P is the contact load without considering any localized deformations of the indenter at the periphery. $U_z = U_s$ for rigid indenter (Figure 2.1). For a non-rigid indenter, E considers the deformation of specimen and indenter. ν is the Poisson's ratio. For indentation, ν of the bone tissue samples is known either through literature or other testing results. During indentation, P / $U_z$can be measured based a load-displacement curve. For the above theory to be valid, the constitutive behavior of the targeted specimen is elastic with time-independent plasticity, meaning that at the very initial unloading point, the specimen approximates pure elastic behaviors. This assumption also allows the measurements of the stiffness which equals to dP / dU_z at the initial unloading point. The simplified Young's modulus calculation procedure is shown in Chapter 2.2.2

2.2.2. Calculation of Young's modulus

The calculation of the Young's modulus was adapted from Pharr and Oliver (Oliver and Pharr 1992). At the initial unloading point, the deformation of the tested sample and indenter was assumed to be completely elastic. The load-displacement relationship can be written as power law (Sneddon 1965). 80% of the unloading curve was used for fitting by a power law through a Matlab curve fitting toolbox (Ezyfit 2.44). The slope at the initial unloading was calculated as stiffness *S*; an illustration is shown in Figure 2.2.

$$S = \frac{dP}{dh} \tag{2.1}$$

The effective modulus or reduced modulus, E_r, is calculated from stiffness *S*, by

$$S = \frac{2}{\sqrt{\pi}} E_r \sqrt{A} \tag{2.2}$$

where A is the contact area. The reduced modulus depends on the deformation from both the samples and the indenter. Therefore, the sample's modulus can be calculated from the effective modulus by

$$\frac{1}{E_r} = \frac{1 - v_s^2}{E_s} + \frac{1 - v_i^2}{E_i} \tag{2.3}$$

where Poisson's ratio of bone was assumed to be 0.3 (Rho, Tsui et al. 1997). The modulus of the custom made indenter E_i was 415 GPa and the Poisson's ratio was 0.16 (National Jet, Lavale, MD).

2.3. Micro-indentation specification and performance

2.3.1 Setup of the indentation system

A high-resolution, non-contact capacitive measurement system (Micro-Epsilon capaNCDT 6300) was used to measure displacement. A high-precision miniature load cell (Honeywell Model 31 Low Range Precision Miniature Load Cell) was used to measure load. A high-performance servo motion controller (NI FW7344) with 62 μs loop update rate was employed for close loop negative feedback motion control. The displacement control system was designed to allow robust linear loading and unloading trajectories through a simple PID control algorithm. The motion controller allows a feedback control of the displacement. The displacement actuation signal of the motion controller was amplified by a PWM servo amplifier (Advanced Motion Controls 30A8) to drive the loading shaft through a linear voice coil motor (BEI Kimco linear actuator LA10-12-027A). The load and displacement signals were simultaneously acquired by a 12-bit data acquisition module on the motion controller. The system can also be easily switched into load control. The motion control of the indentation system was realized by a program based on LabVIEW (NI, Texas). To achieve higher resolution for displacement and load, a signal condition amplifier (Micro-measurements 2120B) with adjustable gains was used to trade off the range of the measurement for better resolution. A schematic of the indentation system is shown in Figure 2.1. The indentation system was connected to an optical microscope (Olympus BX51) with a camera to capture a photo of the bone samples' surface for the purpose of recording the indentation locations. The whole system was mounted on a benchtop vibration isolation platform (Minus K 100BM-8) to reduce vibration noise from the surroundings.

2.3.2 Performance

For the indentation tests in this thesis, the resolution of the displacement was set at 30 nm, and the resolution of the load was set at 0.6 mN. The loading and unloading speed was set at 30 nm/s. The indentation depth was set at 2.5 μm. One cycle of preloading to 2.5 μm was applied before acquiring the indentation data to examine the reversibility of the specimen's deformation and ensure that the unloading data were mostly elastic. The unloading curve of the second cycle was used for the calculation of Young's modulus. The linearity of the unloading curve was 100%, as shown in Figure 2.2. Overall, each test, including the preloading, took roughly five mins to complete.

2.3.3 Instrument compliance and calibration

A cylindrical plat punch (National Jet, Lavale, MD) with a diameter of 25 μm was used. The depth measurements in a depth-sensing system account for not only the deformation of the sample and indenter but also any displacement induced by a reaction force during this process. These additional displacements are assumed to be proportional to the load. These displacements can come from any connecting parts along the loading direction, including the load frame and indenter shaft, the sample mount, and all the connections between these parts. Instrument compliance, C_f, is used to quantitatively describe the displacement induced by the load. At the initial unloading point, the sample/indenter combination and the loading frame can be considered as two springs in series. Therefore, the total compliance, C_t, is the sum of the compliance caused by the deformation of the sample/indenter combination, C_s and C_f, as shown in two equivalent forms below:

$$C_t = C_s + C_f \tag{2.4}$$

$$\frac{dP}{dh} = \frac{1}{S} + C_f \tag{2.5}$$

In this study, to calculate the compliance, the system was switched to load control, and a constant load of 200 mN was applied to make the indenter directly load on the stainless steel stage (absence of sample). The selected load was set to match the maximum load during an indentation on a bone tissue surface at the set indentation depth. The load and displacement curve was highly linear, and the ratio between the maximum displacement and the load was considered as the compliance. Due to the high elastic modulus and hardness of the material of the stage, with 200 mN of load, the compliance caused by the deformation of the stage was less than 0.1% of the total instrument compliance; therefore, it was ignored in this setup.

The displacement sensor and the load cell were calibrated routinely to ensure accurate measurements of the critical displacement and load measurements. The calibration of the displacement sensor was based on a micrometer at 10 μm intervals throughout the sensing range for both loading and unloading. The linearity within the sensing range was also guaranteed based on its sensing principle and out-of-factory calibration. The calibration of the load was based on a series of weights to mimic compression. Regarding the calibration of the system, system compliance was measured before each project as described above. Then, before and after the tests of each sample, three indentation tests were performed on a standard material, fused silica, with a known Young's modulus of 71.7 GPa (literature value consistent with manufacturer data). A highly reproducible measurement of elastic modulus at 70.4 ± 1.9 GPa was achieved.

2.4. Discussion

This chapter serves as a technical foundation for the thesis. A depth-sensing micro-indentation system was built and calibrated for accurate and fast measurements of the Young's

modulus of bone tissue. Compared to nano-indentation, the setup of the micro-indentation system offered several advantages without compromising the accuracy of elastic modulus measurements. First, as mentioned before, the scale of the indentation enables a representation of trabecular bone anisotropic modulus with fewer tests. Second, each cycle of loading and unloading were performed in a shorter time. Third, a cylindrical flat punch was selected as the indenter geometry. Compared to a sphere indenter and sharp indenters, the contact radius of this shape remains constant during testing, which reduces the number of variables that need to be analyzed, especially when it comes to the complicated instrument compliance calibration process involved in using a pyramidal shape indenter. In addition, it avoids the occurrence of multiple cone cracking during the loading process of a spherical indenter under expanding contact area. The sharp edge of the cylindrical indenter results in ultra-high values at the edge of the circle of contact in the stress field, which leads to plastic deformation of bone tissue. However, if the load on the indenter is limited, the small amount of plastic deformation at the circle contact edge does not affect the elastic stress distribution or the analytical solution in the tested specimen. Also, it should be noticed that at our testing scale, the unloading couldn't be perfectly ideal. The recovered bone surface could be not completely flat or parallel. As a result, the indenter could have a receding area that disconnects from the sample. It is also possible that there is friction between punch and bone sample. Therefore, only the initial part of the unloading curve can be considered linear.

Regarding understanding the indentation results measured by this system, there are also several aspects that require careful consideration. First of all, the thickness of the tested trabecular bone needs to be large enough for them to be considered as elastic half-spaces with this indentation setup. It is, therefore, possible that, at the cut surface used for indentation, a

percentage of the exposed trabeculae are too shallow. To minimize the variance caused by this, the indentation locations are selected at the central region of a trabecular bone with a relatively large size. However, the average measured modulus could be overestimated if they are used to interpret the overall trabecular bone tissue material properties, as the central part of a trabecula is likely to be more mineralized and possess higher modulus. Second, the discontinuities such as lacunae might corrupt the continuum assumption of the indentation technique. With larger diameter and deeper indentation displacement, the chances of this system to encounter such situations are much higher than in nano-indentation. To avoid this adverse effect, the indentation locations were selected at sites with few visible lacunae, and any indents on or near a lacuna were excluded from analysis. Though appropriate for trabecular bone, this solution to avoid lacunae might not be as practical if this system was used to test cortical bone, as the lacuna and vascular canals are much more spatially spread with high concentration. A similar consideration applies when there is microdamage surrounding the tested regions, as it has been suggested in the literature that micro-indentation can pick up the difference caused by microdamage, while microdamage does not affect the tissue modulus measurement for nano-indentation(Dall'Ara, Schmidt et al. 2012). We, therefore, made sure all the specimens used in this thesis were fresh cut samples handled with caution and were not subjected to any mechanical testing before indentation. The calculation of the modulus overlooks the damage behavior in bone tissue, which could potentially result in an underestimation of the modulus measurements. However, the calculation based on the two cycles of loading and unloading did not show any differences, suggesting the damage might be limited; this is reasonable given the superior bone material and testing under wet conditions.

The indentation depth was selected to ensure a sufficient amount of unloading data for analysis and also to save testing time. It has been reported that the average modulus measurement isn't affected by the indentation depth, but there are higher variances with low indentation depths, suggesting the selected depth is not likely to affect the measurement of modulus. The loading and unloading rates do affect the modulus values. In general, the higher the loading rate or strain rate, the higher the tested modulus. Linde and colleagues showed that the stiffness varies with strain rate raised to a power of 0.06 by testing bone at the continuum level in compression(Linde, Norgaard et al. 1991). Therefore, all the loading and unloading rates of the tests throughout this thesis were kept consistent.

In summary, a micro-indentation technique with an experimental protocol that provides consistent Young's modulus for trabecular bone both fast and accurately was established. The modulus calculation in the all the studies involved in this thesis was based on this micro-indentation system.

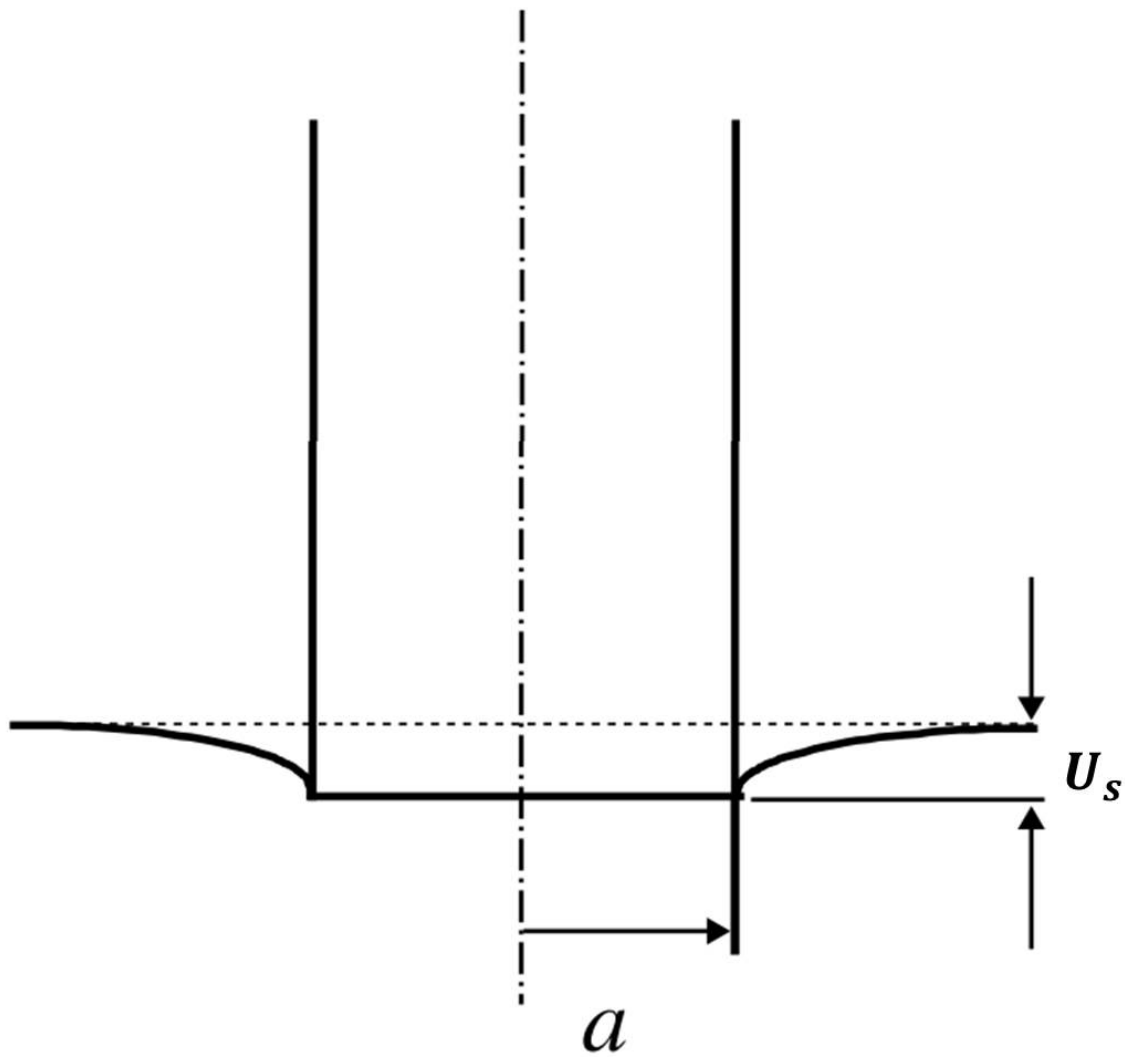

Figure 2.1 Contact geometry of a cylindrical flat punch. a:indenter radius; U_s is the deformation of the sample

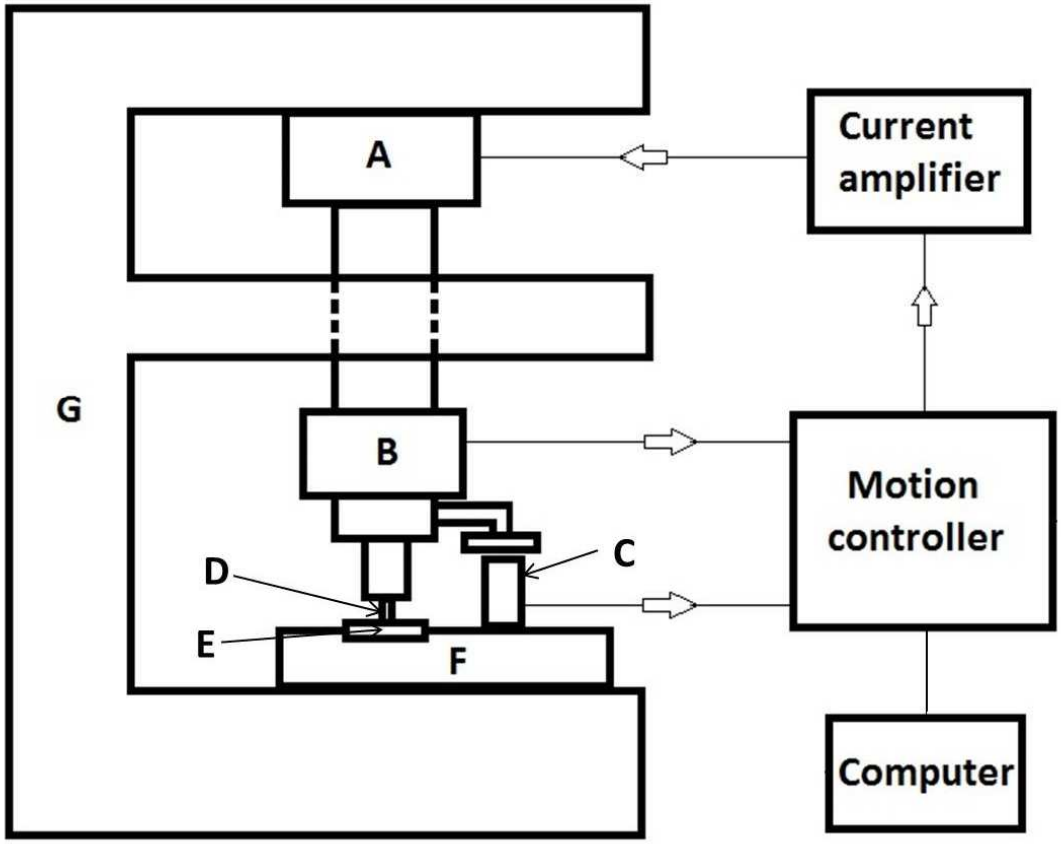

Figure 2.2 Schematic of the indentation system setup. A) Linear actuator; B) Load cell; C) Displacement sensor; D) Indenter; E) Specimen; F) Specimen holder and XY-table G) Load frame

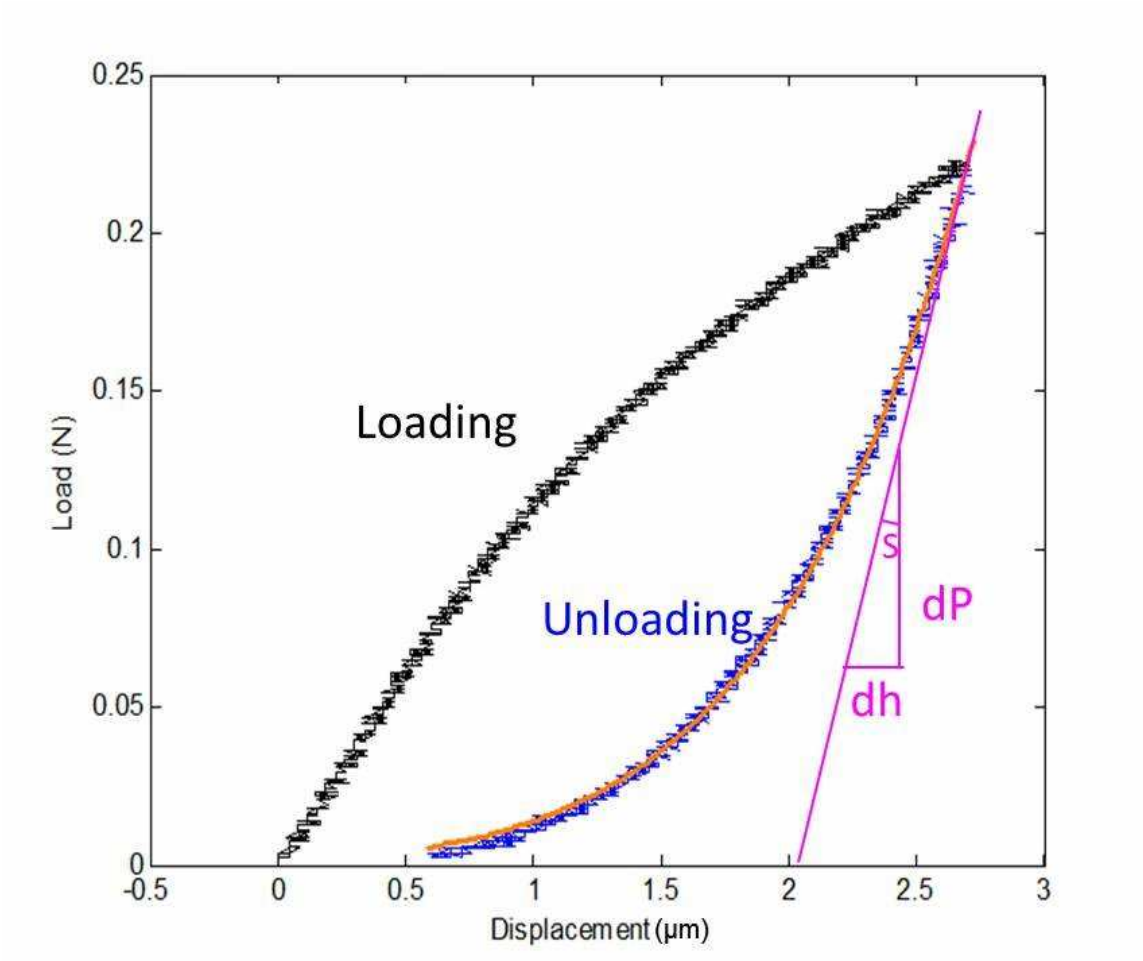

Figure 2.3 Illustration of the loading and unloading curves. The slope at the initial unloading point is defined as stiffness

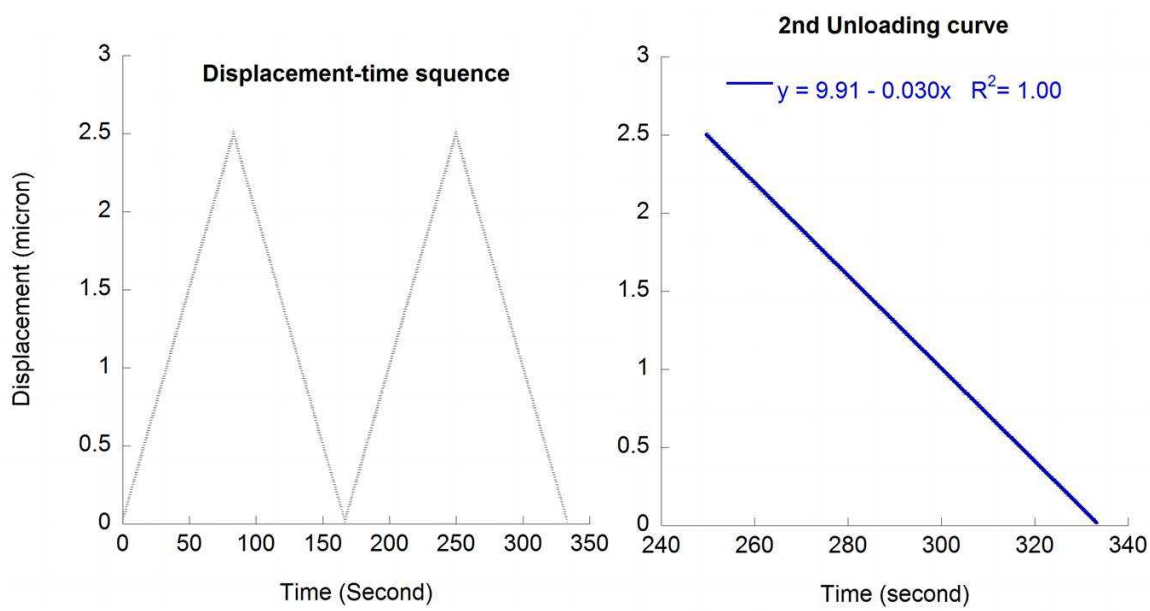

Figure 2.4 Loading profile of each indentation test. The unloading curve is highly linear with an unloading speed of 0.03 μm/s

Chapter 3. Heterogeneous and anisotropic tissue mechanical properties of trabecular bone

3.1. Introduction

Trabecular bone, a crucial bone compartment, is a complicated network of two types of trabeculae: rod-like and plate-like. Together, these plates and rods completely capture the mechanical properties of the entire trabecular network (Wang, Zhou et al. 2015). However, plates play a distinct role in determining the apparent stiffness and bone strength compared with rods (Liu, Sajda et al. 2008, Liu, Zhang et al. 2009, Liu, Walker et al. 2011, Zhou, Liu et al. 2014). For example, more plates are aligned in the loading direction to support and transmit load, while most rods are in the transverse direction to absorb energy in major joints like the hip, knee, and spine. Besides carrying the load, trabecular bone is also metabolic active, and its high surface-area-to-volume ratio makes it susceptible to bone resorption and metabolic bone diseases. The active metabolism further helps shape trabecular bone to grow in a preferred direction to better support (adapt) to loading. In multiple skeletal sites, it has been reported that there are more trabecular plates aligned axially in the loading direction (Liu, Sajda et al. 2008). However, despite the numbers, the trabecular plates tend to have a high tissue mineral density (TMD) in the transverse direction compared to the longitudinal direction (Wang, Kazakia et al. 2015). Furthermore, while the trabecular structure has been studied, how the mechanical properties of each trabecula vary with type and anatomic direction are not known. It has been a challenge in the past to classify trabecular types and anatomic directions from a whole trabecular structure. However, with our individual trabecula segmentation (ITS) technique, the trabecular structure

can be decomposed into individual trabeculae, and the assessment of the trabecular type and anatomic direction can be consistently provided.

The heterogeneity of bone tissue properties has emerged as a key component of bone toughness (Tai, Dao et al. 2007). The spatially inhomogeneous Young's modulus is known to impede the propagation of the cracking after an initial local failure. This spatial heterogeneity is primarily a result of the underlying composition, especially the mineral content. Bone is primarily composed of mineral and collagen; wherein the mineral is considered to be the component that determines stiffness. Due to the constant bone remodeling and the deposition kinetics during bone formation, trabecular bone packets with dramatically different mineralization can be observed adjacent to each other on the same trabecular bone (Boivin and Meunier 2002, Roschger, Paschalis et al. 2008). Donnelly et al. found that the indentation modulus correlated with the mineral concentration in a cortical bone matrix in a young growing rat model. The model took advantage of the monotonic increase in mineralization of a young rat's appositional growth and therefore similar increases in the Young's modulus (Donnelly, Boskey et al. 2010). However, the indentation in this study was performed under dry conditions, which do not mimic the physiological environment. Furthermore, trabecular bone has a much more complicated structure and morphology, which makes mapping the mineralization onto Young's modulus a greater challenge.

Aside from the composition-determined mechanics, bone is also hierarchically organized, and, on each scale, the layouts and structures also dictate the mechanics. The mineralized collagen fibers bundle together and form the lamellar structures which comprise the trabecular packets during bone formation. In cortical bone, these lamellae are spirally oriented around osteons in a highly uniform manner (Wagermaier, Gupta et al. 2006, Faingold, Cohen et al.

2013). As a result, cortical bone is mechanically anisotropic (Swadener, Rho et al. 2001, Reisinger, Pahr et al. 2011, Carnelli, Vena et al. 2013). From the osteon level to the apparent level of cortical bone, it has been reported that bone is stiffer in the longitudinal direction than in the radial or transverse directions (Faingold, Cohen et al. 2013). However, the orientation of the trabecular lamellae layout is far more complicated and heterogeneous. Reznikov et al. studied collagen fibril networks and found that similar to the organization of cortical bone's lamellar structure, the orientation of the collagen in trabecular bone is highly organized and is reflected in the microstructure of the entire fabric (Reznikov, Chase et al. 2015). Wolfram et al. performed indentation tests in two perpendicular directions of trabecular rods and found that the Young's modulus in the longitudinal direction was higher than that in the radial direction (Wolfram, Wilke et al. 2010). However, none of the existing studies have quantitatively confirmed the trabecular type (rod or plate) or whether the trabecular elements had anisotropy.

Thus, the objectives of this study are to (1) compare the tissue modulus and co-localized TMD between trabecular plates and rods, (2) compare the tissue modulus between axial and lateral directions in different trabecular types of different anatomic directions, and (3) examine the correlation between TMD and Young's modulus in different trabecular types and indentation directions. The outcomes of the study will provide new insights into the mechanical properties of individual trabecular plates and rods.

3.2. Materials and Methods

3.2.1. Specimen preparation and μCT imaging

Fifteen cylindrical (~8.5 mm diameter, ~15 mm length) on-axis (along the principle trabecular orientation) human trabecular bone cores were harvested from the femoral neck (FN,

n=5), greater trochanter (GT, n=5), and proximal tibia (PT, n=5) along the principle trabecular direction following a previously reported protocol (Morgan and Keaveny 2001). The subjects were obtained from the International Institute for the Advancement of Medicine (Scranton, PA) with no history of bone-related metabolic diseases. The age, gender, and bone volume fraction are shown in Table 3.1. Contact x-ray radiograph was taken to verify that there was no fracture, damage, or other bone pathologies in the specimens. To ensure that the longitudinal axis of the bone core was aligned along the principle trabecular orientation, x-ray radiographs were taken on two orthogonal planes parallel with the longitudinal axis to confirm that the difference between the trabecular orientation and the longitudinal axis was no larger than 10°. The bone cores were sprayed with Gentamicin solution (Hoffler, Guo et al. 2005), wrapped with wet gauze, and kept in sealed plastic bags at −20 °C prior to experiments.

The cylindrical specimens were scanned along the longitudinal axis by a μCT system (VivaCT 40, Scanco Medical AG, Switzerland) at 15 μm voxel size with 200 ms integration time and with a source potential of 55 kV and tube current of 109μA. Gaussian filter (Gauss sigma=0.8, gauss support=1) and anatomic site-specific thresholds were applied to segment grayscale images into binary images composed of bone and marrow. These sets of images were acquired ITS-based plate and rod morphological analysis.

The cylinder samples were cut with an Isomet low-speed saw (Buehler, Lake Bluff, IL). Three segments 5mm in length were saved for indentation. Each segment was rinsed with a waterjet to remove all the marrow and bone surface cells in trabecular cavities. The cleaned bone core was left in the air for an hour until the bone tissue was completely dry. A weakly exothermal liquid plastic (Measurements Group, Inc., Ra-leigh, NC) was used to embed the dried bone cores. The embedded samples were placed in a vacuum chamber for 30 mins to facilitate

the liquid plastic to fill in the porosity of the trabecular bone and prevent the formation of air bubbles. Then the samples were left at room temperature for 18 hours to cure fully. All specimens were then cut into a 10mm x 10mm cross section. Then the specimens were polished in wet conditions with waterproof progressive grades of silicon carbide paper (800, 1200, 2400 and 4000 grit) and finished on a soft cloth with 1μm and 0.05μm alumina suspension (Struers, Westlake, OH). The polished samples were cleaned in a distilled water ultrasonic bath for 15 min (to get rid of the polish particles left on the bone surface). The polished sample was ~4mm in thickness and was prepared for μCT-based TMD measurements and then indentation tests.

The polished samples were scanned again by μCT with a source potential of 55 kV and tube current of 109μA at a voxel size of 10.5μm at 600ms integration time to achieve a high image quality for TMD measurements. To minimize the beam hardening effect, a standard aluminum filter was installed in the μCT scanner, and a voltage- and scanner-specific beam-hardening correction algorithm derived from a wedge phantom of 200 mg HA/cm^3 density was implemented (Burghardt, Kazakia et al. 2008). A set of 5 density calibration phantoms (CIRS, Norfolk, Virginia) was scanned with the samples for *in situ* calibration of the attenuation-to-TMD relationship. An illustration of the CT scan with phantoms and the linear regression of the calibration relationship are shown in Fig 3.1.

3.2.2. ITS-based anatomic direction and indentation direction selection

The binary μCT image corresponding to the 15mm whole cylinder sample was then subjected to ITS analysis. The detailed procedure and principle of ITS analysis were described in our previous publication (Liu, Sajda et al. 2008). As shown in Fig 3.2, the trabecular types and anatomic directions of the trabeculae on the plane corresponding to indentation surface were displayed in different colors. The combination of the two colors of each trabecula from the two

corresponding images represented a trabecular type in an anatomic direction. For example, the circled TR trabecula stands for a "transverse rod". The very outside layer of trabecular bone close to the boundary was excluded from selection as shown in Fig 3.2 to avoid false classification of the discontinued trabecular bone structure.

The anatomic directions were defined with respect to the principle trabecular directions. For a trabecular plate, angle Φ was defined as the angle between the normal vector of the plate and the longitudinal axis. For a trabecular rod, angle Φ was defined as the angle between the direction of the rod and the longitudinal axis. Trabecular orientations were categorized into longitudinal (angle Φ 60°-90° for plates and 0°-30° for rods), oblique (angle Φ 30°-60° for plates and rods), and transverse (angle Φ 0°-30° for plates and 60°-90° for rods), as shown in Fig 3.3A.

The indentation direction was classified into axial and lateral directions (Fig 3.3B). For a cylindrical rod, the axial direction was defined as the longitudinal direction, and the lateral direction was defined as the radial direction. For a plate, the axial direction was defined as the in-plane direction, and the lateral direction was defined as the normal direction.

3.2.3. Microindentation and tissue modulus measurements

The calculation of the Young's modulus was adopted from Pharr and Oliver (Oliver and Pharr 1992). At the initial unloading point, the deformation of the tested sample and indenter was assumed to be completely elastic. 80% of the unloading curve was used to fit by a power law through a Matlab curve-fitting toolbox (Ezyfit 2.44). The slope at the initial unloading was calculated as the stiffness. The effective modulus, or reduced modulus, E_r, was calculated from the stiffness S by $S = \frac{2}{\sqrt{\pi}} E_r \sqrt{A}$, where A is the contact area. The Young's modulus of the samples, E_s, was then calculated from the effective modulus by $\frac{1}{E_r} = \frac{1-v_s^2}{E_s} + \frac{1-v_i^2}{E_i}$, where the

Poisson's ratio of bone was assumed to be 0.3 (Rho, Tsui et al. 1997). The modulus of the custom made indenter E_i was 415 GPa, and the Poisson's ratio was 0.16 (National Jet, Lavale, MD). The system was calibrated by measuring fused silica, a standard material possessing a highly reproducible elastic modulus of 72 GPa.

The selected trabecular plates and rods classified by ITS were subjected to indentation test. Plates and rods were tested in both axial and lateral directions. For each selected trabecula, three indentation tests were made. The sample was kept wet by Gentamicin solution throughout the indentation procedure. Indentations were separated by at least 50μm from each other and from the boundary of a bone to minimize the boundary effect. A cylindrical indenter tip with a diameter of 25 μm (National Jet Co., Inc, LaVale, MD) was used. The samples were preloaded to 2.5 μm then unloaded to 0.25 μm, and then indentation was driven to a depth of 2.5 μm. The resolution of the displacement sensor was 25 nm. Displacement was applied as a monotonic ramp at (50 nm/s) and then an unloading ramp at the same rate. The unloading curve was then used to calculate the modulus. During the indentation, a photo of each selected trabecula was taken by a light microscope.

3.2.4. Image registration to co-localize TMD and tissue modulus

The calculation of the Young's modulus was adopted from Pharr and Oliver (Oliver and Pharr 1992). At the initial unloading point, the deformation of the tested sample and indenter was assumed to be completely elastic. The initial unloading curve was used to fit by a power law through a Matlab curve-fitting toolbox (Ezyfit 2.44). The slope at the initial unloading was calculated as the stiffness. The effective modulus, or reduced modulus, E_r, was calculated from the stiffness S by $S = \frac{2}{\sqrt{\pi}} E_r \sqrt{A}$, where A is the contact area. The Young's modulus of the

samples, E_s, was then calculated from the effective modulus by $\frac{1}{E_r} = \frac{1-v_s^2}{E_s} + \frac{1-v_i^2}{E_i}$, where the Poisson's ratio of bone was assumed to be 0.3 (Rho, Tsui et al. 1997). A cylindrical flat punch with a diameter of 25 μm was used. The modulus of the custom made indenter E_i was 415 GPa, and the Poisson's ratio was 0.16 (National Jet, Lavale, MD). The system was calibrated by measuring fused silica, a standard material possessing a highly reproducible elastic modulus of 72 GPa.

The selected trabecular plates and rods classified by ITS were subjected to indentation test. Plates and rods were tested in both axial and lateral directions. For each selected trabecula, three indentation tests were made. The sample was kept wet by Gentamicin solution throughout the indentation procedure. Indentations were separated by at least 50μm from each other and from the boundary of a bone to minimize the boundary effect. A cylindrical indenter tip with a diameter of 25 μm (National Jet Co., Inc, LaVale, MD) was used. The samples were preloaded to 2.5μm then unloaded to 0.25μm, and then indentation was driven to a depth of 2.5μm. The resolution of the displacement sensor was 25 nm. Displacement was applied as a monotonic ramp at (50 nm/s) and then an unloading ramp at the same rate. The unloading curve was then used to calculate the modulus. During the indentation, a photo of each selected trabecula was taken by a light microscope.

3.3. Results

3.3.1. TMD and tissue modulus difference between plates and rods

Altogether, 594 indentations were performed, of which 540 were used after removing outliers and the indents close to (less than ten μm) or on lacunae. Mean and standard deviation of Young's modulus and the co-localized TMD of the tested plates and rods were compared in Fig

3.5. The Young's modulus of the plates ranged from 6.1 to 27.3 GPa, and the Young's modulus of the rods ranged from 5.8 to 25.4 GPa. The TMD ranged from 612 to 1384 mg HA/cm^3 for plates and 573 to 1369 mg HA/cm^3 for rods. The average Young's modulus of the plates (15.1 ± 3.9 GPa) was significantly higher compared to that of the rods (13.1 ± 3.4, $p<0.05$), which coincided with the co-localized TMD (1040 ± 142 mg HA/cm^3 for plates, 957 ± 159 mg HA/cm^3 for rods, $p<0.05$). Multivariate ANOVA test showed the TMD-adjusted Young's modulus of plates and rods were not different ($p=0.87$).

3.3.2. Tissue modulus difference between axial and lateral directions

By comparing the Young's modulus in axial and lateral directions, we found that, regardless of the trabecular type and anatomic direction, the Young's modulus was higher in the axial direction compared to the lateral direction ($p<0.05$, Fig 3.6). The ratio between the axial and lateral modulus in each direction ranged from 1.13 to 1.41. The axial modulus in different anatomic directions was not different, neither was the lateral modulus in different anatomic directions. For the correlated TMD, it increased from the longitudinal directions to oblique directions and to transverse directions. Multivariate ANOVA tests confirmed that the differences in Young's modulus in different anatomic directions were likely a result of the different TMD distributions, as the TMD-adjusted modulus was not different among the anatomic directions.

3.3.3. Correlations between TMD and Young's modulus in different indentation directions

Overall, the TMD and Young's modulus were moderately correlated to each other. However, TMD and tissue modulus are strongly correlated in both axial and lateral direction regardless of trabecular type and anatomic direction. Multiple linear regression analysis showed that the correlations between TMD and tissue modulus of different anatomic sites (FN, GT, and PT), trabecular types, and anatomic directions were not different ($p=0.76$). So the data was

pooled according to trabecular direction. TMD-to-modulus correlations were significantly different between axial and lateral directions ($p<0.05$, Fig 3.7).

3.4. Discussion

To our knowledge, this was the first study to test and confirm the anisotropic Young's modulus of randomly selected individual trabecular plate and rod elements. We utilized ITS-based plate and rod microstructural analysis to systematically classify the trabecular type, anatomic directions, and the axial and lateral indentation directions of the trabecular elements. The major differences in the Young's modulus in the axial and lateral directions were described regardless of the trabecular type and anatomic directions. Our results extended the finds of Wolfram et al., who described the nano-indentation-measured anisotropic Young's modulus of trabecular rods. While both studies discovered the Young's modulus of trabecular rods was higher in the axial direction, and the anisotropic ratios were both close to 1.24, our study quantitatively measured the indentation direction with respect to trabecular direction and tested on well-defined trabecular types. Not only trabecular rods, but also trabecular plates, were found to possess higher Young's modulus in the axial direction compared to the lateral directions. However, the anisotropy ratio of trabecular rods in the three directions (1.33 ± 0.09) was higher than that of trabecular plates (1.18 ± 0.03, $p<0.05$). Additionally, the anisotropic Young's modulus was consistent in all longitudinal, transverse, and oblique anatomic directions, not simply limited to the trabecular bone aligned in the loading direction. This suggests the trabecular bone aligned in different anatomic directions essentially might have a similar lamella or ultrastructure that relates to the orientation of the trabecular bone. This finding coincides with the work conducted by Reznikov et al., describing how the structure of the collagen fibril

network in human trabecular bone is organized similarly as the corresponding trabecular packets (Reznikov, Chase et al. 2015).

Besides the universal anisotropy of individual trabecular bone, another major strength of this study is to describe and to suggest the reason behind the differences between trabecular plates and rods. Liu et al. have described trabecular plates as a type of trabeculae that play a major role in sustaining the load compared to rods (Liu, Zhang et al. 2009), and the anisotropy of apparent level trabecular bone modulus was largely attributed to the axially aligned trabecular elements (Liu, Sajda et al. 2008). The findings of this study further support the previous discoveries by describing a higher Young's modulus in trabecular plates compared to trabecular rods on the bone tissue level. This indicates that the superior role of plates in determining a trabecular structure's stiffness and yield strength results from not only its higher bone volume fraction and a better alignment, but also its higher tissue-level material properties. The TMD-adjusted Young's modulus was not different between plates and rods, suggesting that the higher modulus in trabecular plates was likely due to its higher mineral density. The higher TMD in plates was consistent with the validation study by Wang et al., where TMD was confirmed to be higher in trabecular plates by SRmCT (Wang, Kazakia et al. 2015). The difference in TMD and Young's modulus between plates and rods was likely, in return, caused by their adaption to the loading environments.

Further, this study provides a broader understanding of the role of TMD in trabecular bone mechanics. It has been widely accepted that the mineral content is the most important determinant of bone mechanical properties on the tissue level. Donnelly et al. described that the bone tissue material composition (mineral contents) highly correlated with the Young's modulus in cortical bone (Donnelly, Boskey et al. 2010). Kerrigan et al. found a weak correlation between

modulus measured by large-scale relaxation indentation tests and TMD measured by μCT in the human knee patella. However, the scale of the indenter in their study was 0.1mm, which is almost as big as the trabecular bone thickness; therefore, this was more of a measure on the apparent-level than of the tissue-level material property. A significant and strong correlation between TMD and Young's modulus was never confirmed prior to our study in trabecular bone due to the complicated nature of the morphology and ultrastructure, and because a scale necessary to still characterize the tissue material properties but be large enough to be representative of the apparent bone samples with limited number of tests was not feasible. In this study, we not only confirmed the strong correlation between TMD and modulus, but also suggest such correlations are different in the axial and lateral directions. These results indicate that the fundamental underlying ultrastructure of trabecular plates and rods might be the same in the corresponding trabecular directions. However, the difference might lie in the lamellae alignments between the axial and lateral directions. Taken together, this study suggests the mechanics of trabecular elements are mainly twofold: 1) within an individual trabecular plate or rod, a consistent anisotropic modulus exists due to the similarly aligned lamellae structure, and 2) spatially-related heterogeneous Young's modulus is a result of distinct TMD distributions.

Aside from the strengths of this research, several limitations and considerations should be taken into account. First, the Young's modulus was ranged from 5.8 GPa to 27.3 GPa and averaged at 14.0 ± 4.1 GPa, slightly lower than the literature reported value. However, it is comparable to 11.4 ± 5.6 GPa, the Young's modulus of femoral neck trabecular bone lamella reported by Zysset and colleagues (Zysset, Guo et al. 1999). A possible reason for lower modulus is that the indentation scale was different, where the small gaps between lamellar layers and the absence of lacunae were likely to cause an underestimation of the modulus. Also, in this

study, equal numbers of trabecular plates and rods were chosen for indentation as compared to other studies, where most of the selected trabecular bone would be plates since, in the loading sites, most of the bone volume is comprised of trabecular plates. Second, the actual indentation direction was not perfectly in line with the axial and lateral directions defined in the method, as there was an angle between the trabecular direction and the normal of the cut surface of the embedded sample for all the selected trabeculae. Thus, the indentation tests were not made completely in the axial and lateral direction, and, overall, this might have resulted in a slight underestimation of the modulus. To evaluate the errors potentially caused by the misalignment, a linear FE model simulation was performed to mimic the indentation procedure (Abaqus 6.11, Dassault System Americas, Waltham, MA). As shown in Figure 3.8, the modulus was not much affected by the material directions when the angle was smaller than 20 degrees. In this study, the trabeculae were selected for indentation only when the angle between material direction and trabecular indentation directions were smaller than 20 degrees. Third, the specimens in this study were from relatively older individuals (average aged at 70). In this age group, we expected to see an overall relatively low BMD but higher heterogeneous mineralization distribution. While the age might affect the tissue mineralization, the tissue modulus should be influenced by age similarly and, in this group, the overall tissue modulus was expected to be lower than a younger age group. However, we expected the correlation between TMD and Young's modulus to remain the same in the younger adult group. Fourth, TMD measurements were based on the μCT images of embedded samples. Though the best resolution was used, due to the partial volume effect, the first couple slices of μCT images close to the indentation surface were excluded in the calculation of TMD. Lastly, the measures of the trabecular rod and plate moduli in lateral

directions should be interpreted cautiously, as there was a possibility that a certain percentage of the indented trabeculae were cut too thin to be considered elastic half-spaces.

In conclusion, we comprehensively examined the mechanical properties of individual trabecula and the corresponding relationship with trabecular type, anatomic direction, and indentation direction. For the first time, the anisotropic Young's modulus of individual trabecular plates and rods was systematically measured and confirmed. Strong but different correlations were found between the tissue modulus and TMD in the axial direction and lateral direction, indicating that the underlying ultrastructure may play a critical role in the tissue mechanical properties of individual trabeculae. Plates and rods are likely to have similar ultrastructure on the corresponding axial and lateral directions. The different mechanical properties between trabecular plates and rods and among differently oriented trabecular bone are more likely to be a result of the different mineralization distributions. This chapter serves as a foundation of this thesis. The next several chapters will be based on this chapter to evaluate how these TMD-dependent anisotropic tissue properties play a role in whole bone mechanical competence and how diseases alter bone tissue material properties.

Table 3.1. Donor and sample information in the experimental set.

Anatomic site	*No. Specimens*	*No. Donors (male/female)*	*Age (year)*	*BV/TV*
Proximal tibia	5	5 (4/1)	68±5	0.096±0.03
Femoral neck	5	5 (3/2)	70±4	0.29±0.09
Greater Trochanter	5	5 (3/2)	71±5	0.087±0.03

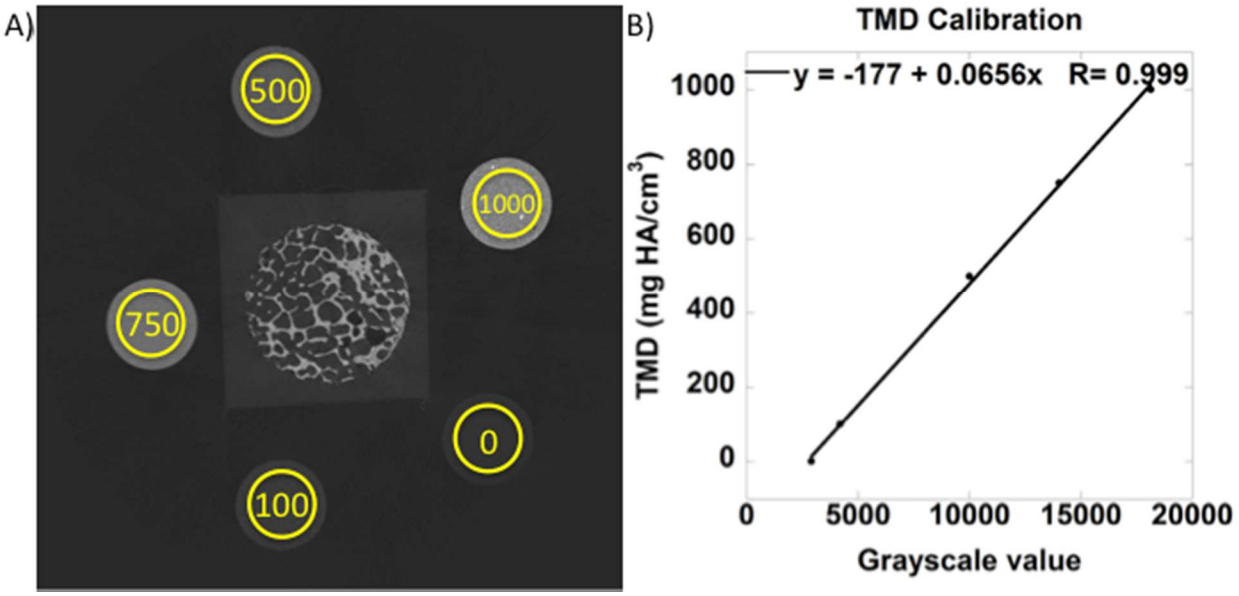

Figure 3.1 Illustration of a µCT scanning with density calibration phantoms and the linear regression of the calibration relationship

A) A 2D slice of a µCT image with *in situ* density calibration phantoms (0, 100, 500, 750, 1000 mg HA/cm^3)

B) Specimen-specific calibration relationship

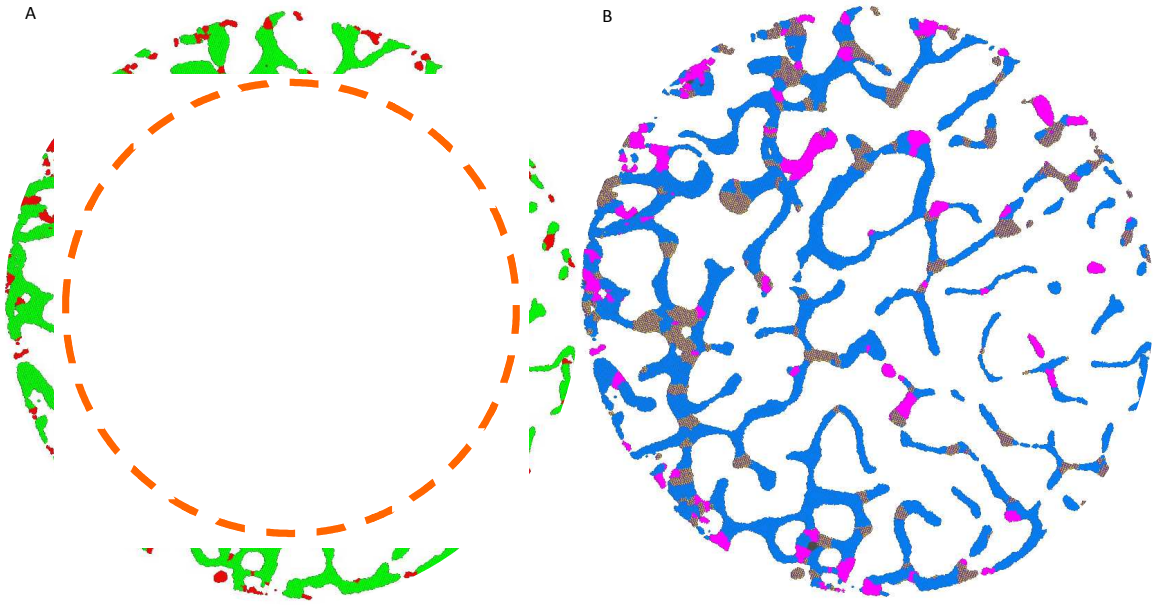

Figure 3.2 Illustration of ITS display of trabecular type and anatomic orientation on the indentation surface.

A) ITS display of plates and rods, with plates indicated in green and rods indicated in red; inside the orange dash circle (radius= 3mm) is the region of selection. The most outside layer of trabecular bone was not selected to avoid the inaccurate classification of ITS on the discontinued boundaries. TP: transverse plate; LP: longitudinal plate; TR: transverse rod; LR: longitudinal rod. The boxed area was used for illustration of image registration in Fig 3.4

B) ITS display of anatomic orientation, with the longitudinal direction in blue, transverse direction in pink, and oblique direction in tan.

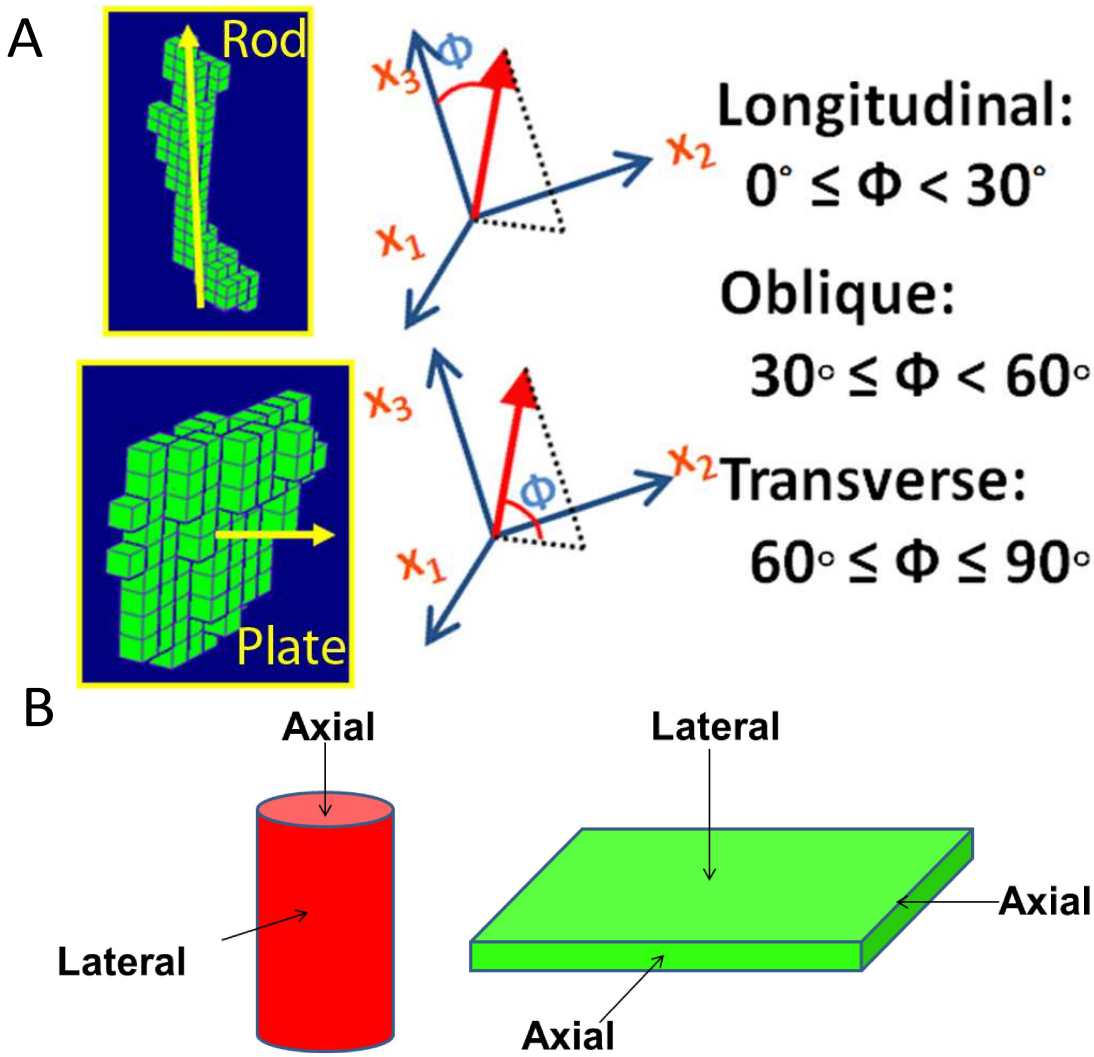

Figure 3.3 Illustration of anatomic directions and indentation directions.

A) Different classification for anatomic directions between plates and rods.

B) Classification of the axial and lateral cross-section directions.

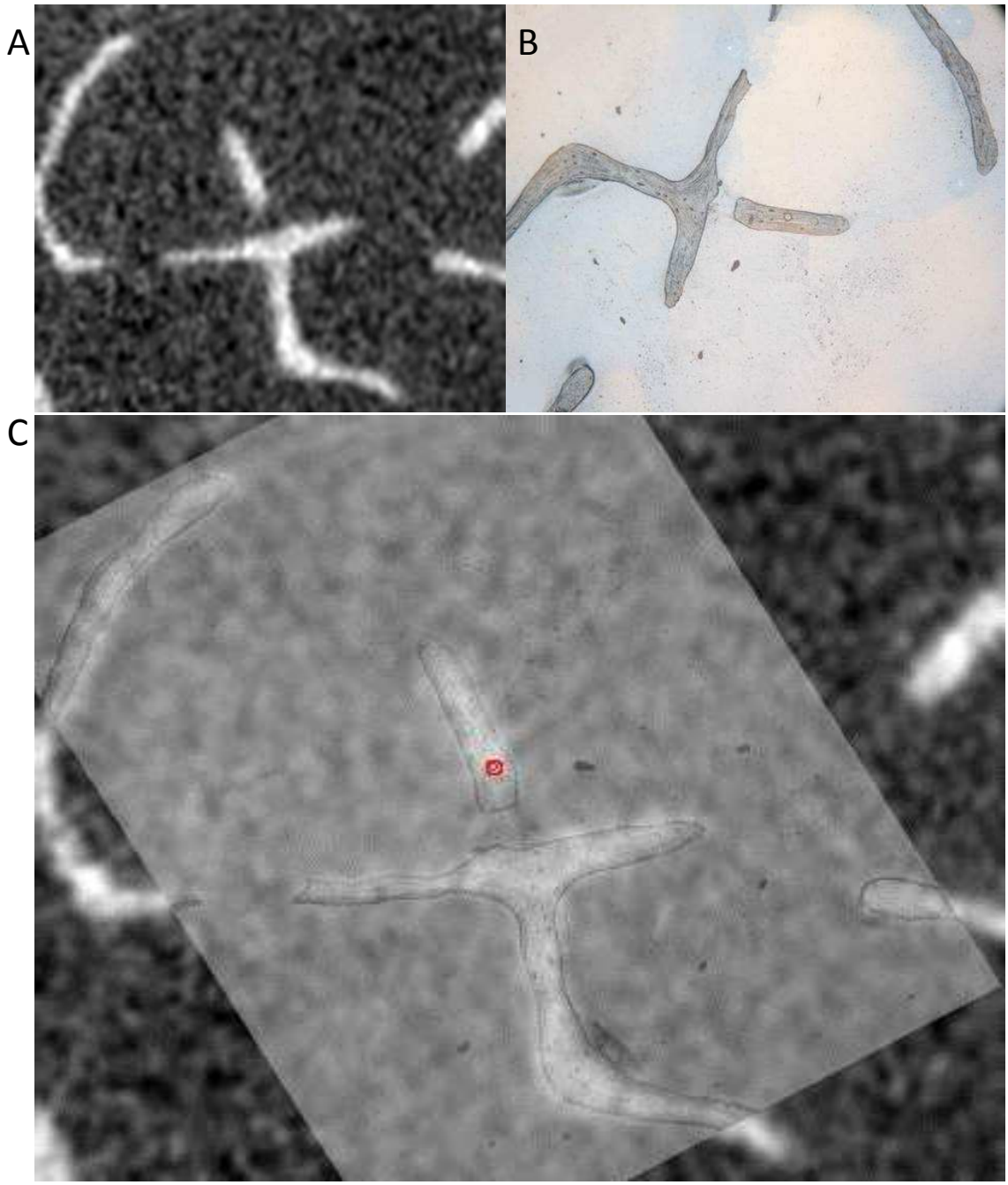

Figure 3.4 Illustration of co-localizing the TMD and Young's modulus.

A) μCT slice of an individual trabecular bone corresponding to the indentation locations.
B) Microscopic photo of a region selected for indentation.
C) Registered image between μCT and the microscopic photo; the red circle indicates one of the indentation locations.

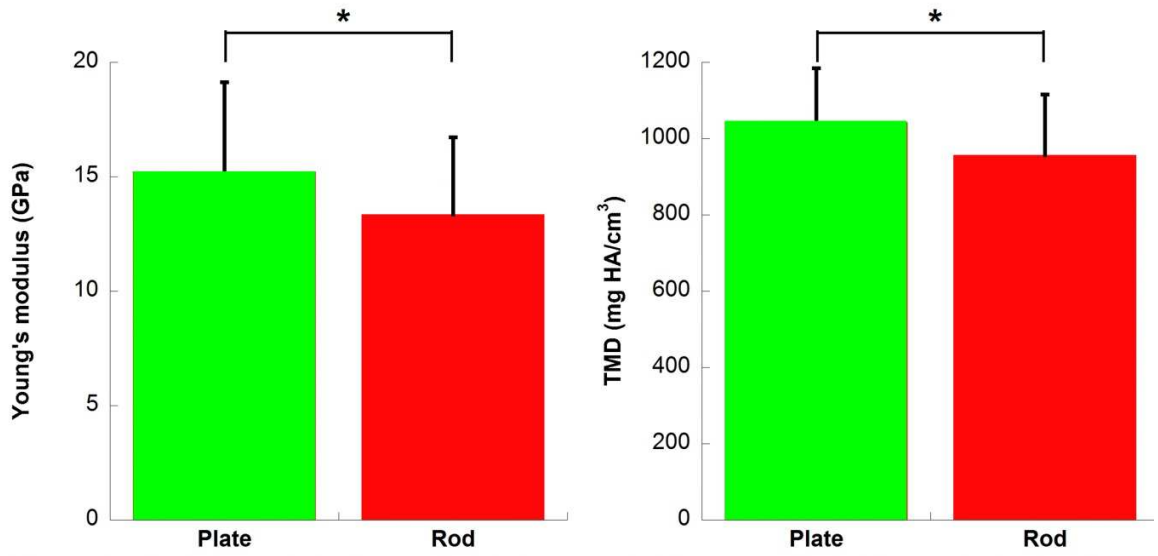

Figure 3.5 Comparisons of Young's modulus and co-localized TMD between plates and rods

A) Comparison of Young's modulus between trabecular plate and rod. *p<0.05

B) Comparison of co-localized TMD between trabecular plate and rod. *p<0.05

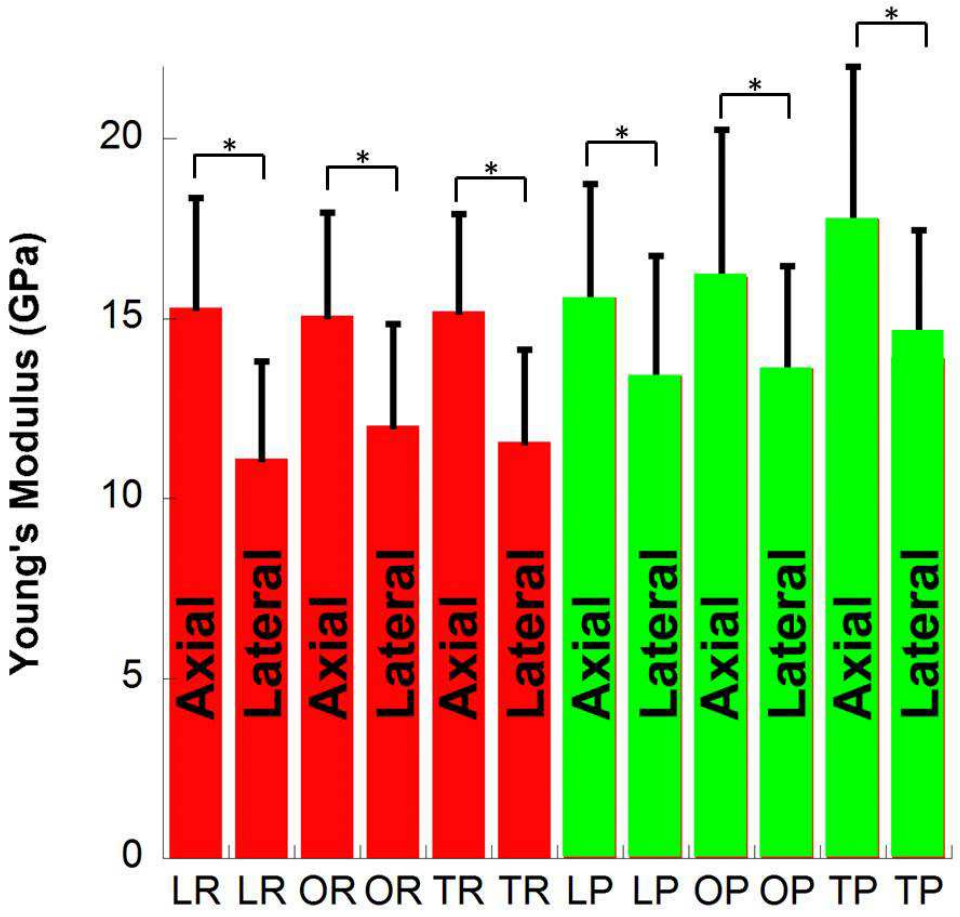

Figure 3.6 Comparisons of Young's modulus between axial and lateral directions for all trabecular types and anatomic directions; *p<0.05.

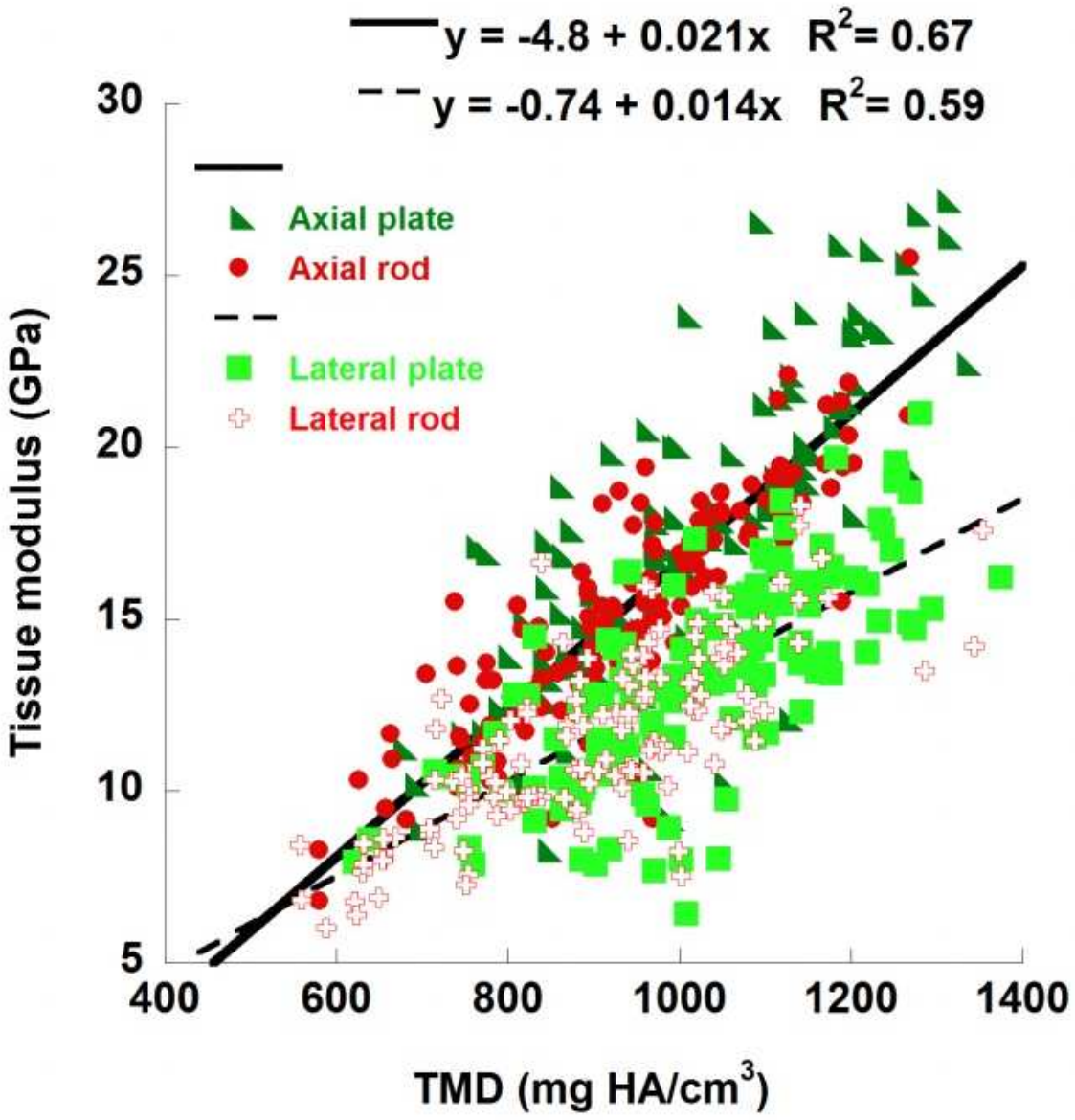

Figure 3.7 Comparisons of Young's modulus between axial and lateral directions for all trabecular types and anatomic directions; *p<0.05.

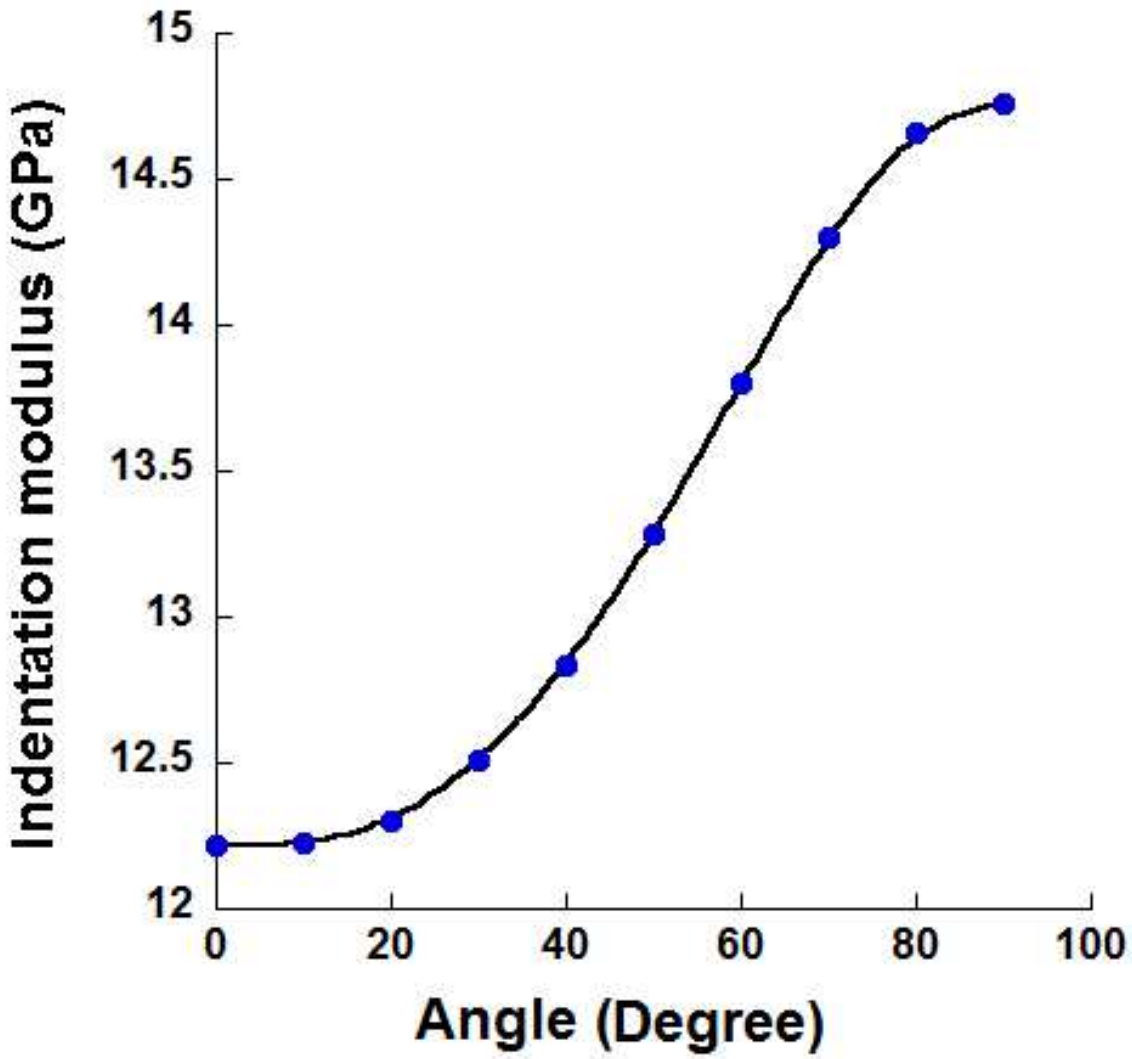

Figure 3.8 Simulated indentation modulus corresponding to the different angle between the material direction and indentation directions.

Chapter 4. μFE modeling with anisotropic and heterogeneous tissue properties

4.1. Introduction

Human bone consists of a heterogeneous distribution of mineralization due to spatially distinctive turnover and the kinetics of mineral accumulation. The heterogeneous mineralization dictates the heterogeneous tissue modulus distribution. Suggested by the work in chapter 3, trabecular bone possesses anisotropic material properties. Also, trabecular bone is likely to possess anisotropy for the reason that the trabecular bone tissue is essentially comprised of highly organized lamellar layers similar to cortical bone (Reznikov, Chase et al. 2015), the anisotropy of which has been widely studied (Swadener, Rho et al. 2001, Reisinger, Pahr et al. 2011, Carnelli, Vena et al. 2013). Bone's remarkable mechanical properties are fundamentally originated from its optimized hierarchical structures. Therefore the anisotropic and heterogeneous tissue properties are likely to affect larger scale mechanical behavior of human bone.

Tissue material properties have been widely believed to be an important determinant of human bone strength. There have been extensive studies focusing on tissue material properties and bone strength. However, there is a gap between how tissue material properties contribute to whole bone strength. Currently, the widely-used bone strength assessment method, μCT-based μFE analysis, captures the detailed and patient-specific microstructure. However, it routinely assumes an empirical constant tissue modulus and doesn't take the spatially heterogeneous TMD observed by μCT into account (Ulrich, Hildebrand et al. 1997, Kabel, van Rietbergen et al. 1999, van der Linden, Birkenhager-Frenkel et al. 2001). Furthermore, although there have been

attempts to simulate the contributions of heterogeneity to whole bone level bone mechanics (van der Linden, Birkenhager-Frenkel et al. 2001, Jaasma, Bayraktar et al. 2002, Bourne and van der Meulen 2004), most studies assume a certain scaled correlation between the TMD and tissue modulus. Wolfram et al. used nanoindentation to experimentally determine the tissue modulus and used specimen-specific averaged tissue modulus as a material property input for μFE modeling. Although it accounts for specimen specificity and the tissue material prosperities are measured instead of assumed, the heterogeneity and anisotropic material properties were not considered, and, possibly as a result, the predicted stiffness between specimen-specific tissue modulus models was not different from the global tissue modulus models (Wolfram, Wilke et al. 2010). From a quantitative point of view, the predicted μFE results are critically dependent on the chosen trabecular bone tissue properties. Thus, the inclusion of experimentally determined heterogeneous and anisotropic material properties in μFE models is most likely to fill in the gap and reflect the realistic contribution of tissue properties to apparent level bone mechanics.

Anisotropic tissue material properties affect the cortical bone on both tissue level and structural level (Swadener, Rho et al. 2001, Reisinger, Pahr et al. 2011, Carnelli, Vena et al. 2013). The uniform arrangement of osteons in the longitudinal direction and the consistently higher Young's modulus of the osteon in the longitudinal direction compared to radial direction make the anisotropic mechanical properties of cortical bone straightforward to understand. However, due to the complicated trabecular bone morphology and microstructure, there is a lack of knowledge in the anisotropy of individual trabecular bone elements and trabecular bone structure as a whole. If trabecular plates and rods randomly grew in different directions, then the anisotropy of individual trabecular bone should not play a role in the overall trabecular structure. However, trabecular bone stiffness and yield strength are largely dependent on the axially

aligned trabecular bone elements (Liu, Sajda et al. 2008), and, in the loading sites, there is a principle trabecular direction, meaning most trabecular bone is aligned in one direction (von Meyer 2011). Our previous work confirms most plates are aligned longitudinally along the loading directions (Liu, Sajda et al. 2008), coinciding with the higher Young's modulus in trabecular plates. Therefore, the newly discovered anisotropic Young's modulus of trabecular plates is likely to contribute to the apparent level trabecular mechanical behaviors due to the amplification of the anisotropy of trabecular bone microstructure.

The objective of this study is to quantify the contribution of tissue-level anisotropy and heterogeneity to apparent level bone mechanical competence. To achieve the objective, one anisotropic/heterogeneous model, three isotropic/heterogeneous models, and one isotropic/homogeneous model were created for each specimen, and the stiffness and strength were compared between the outcomes of each model.

4.2. Materials and Methods

4.2.1. Specimen Preparation

The samples in this study were adopted from my colleagues Dr. Wang's previous study and the preparation procedures were exactly the same as descided in her paper(Wang, Zhou et al. 2015). Fifteen sets of freshly frozen human cadaveric tibiae (11 male/4 female, age: 71 ± 9 years, ranging from 55 to 84 years old) and fifteen sets of proximal femurs (8 male/7 female, age 73 ± 14 years, ranging from 40 to 91 years old) were obtained from the International Institute for the Advancement of Medicine (Scranton, PA) with no history of bone-related metabolic diseases, as shown in Table 4.1. Contact x-ray radiography was performed to verify that there was no fracture in the specimens. Cylindrical trabecular bone cores with a diameter of ~8.5 mm were

prepared from proximal tibiae and femurs along the principle trabecular orientation (Morgan and Keaveny 2001). To ensure that the longitudinal axis of the bone core was aligned with the principle trabecular orientation, x-ray radiographs were taken on two orthogonal planes parallel to the longitudinal axis. Any sample with an angle between the trabecular orientation and the longitudinal axis larger than 10° was excluded from this study. In total, 20 proximal tibia, 20 femoral neck, and 20 greater trochanter trabecular bone cores were harvested. Specimens were kept in sealed plastic bags at -20°C and wrapped with wet gauze between preparations.

4.2.2. μCT imaging and segmentation

The specimens were scanned along the cylindrical axis using a μCT scanner at an isotropic voxel size of 15μm with 55 KVp energy and 109 μA at 200 ms integration time. The middle 15 mm trabecular bone of the cylinder was scanned to assure that the 8 mm strain gage region in mechanical testing was included in the μCT image. To minimize the beam hardening effect, a standard aluminum filter was installed in the μCT scanner, and a voltage- and scanner-specific BHC algorithm derived from a wedge phantom of 200 mg HA/cm^3 density was implemented (Burghardt, Kazakia et al. 2008). Gaussian filters (Gauss sigma=0.8, gauss support=1) and anatomic site-specific thresholds were applied to segment grayscale images into binary images composed of trabecular bone and background. The binary images were used as a mask to apply to the original grayscale image. Therefore an image with grayscale values on trabecular bone and background as zero was generated. These new grayscale μCT images were used to convert into heterogeneous/isotropic and heterogeneous/anisotropic μFE models.

4.2.3. μFE modeling: homogeneous/isotropic model and heterogeneous/isotropic model

For each μCT image, μFE models were generated by converting each voxel into an 8-node brick element. A tension-compression asymmetric model with plastic hardening was used

in the simulation with a Poisson's ratio of 0.3. A uniaxial compression test was simulated in the μFE analysis, and fixed boundary conditions were assigned to the nodes at the two ends of the model. The bone tissue constitutive law was prescribed based on the elastoplastic material model that incorporates geometric large deformations and material non-linearity (Papadopoulos and Lu 2001). The tissue-level yield strains were assumed to be 0.81% of strain in tension and compression (Bayraktar, Morgan et al. 2004). The post-yield tissue modulus was 5% of its initial value. A displacement equivalent to 1% strain was applied in the axial direction. The elastic modulus of each sample was calculated by the linear curve fit within a 0-0.2% strain range. An implicit parallel FE framework, Olympus, was used to solve the nonlinear μFE models on a Sun Constellation Linux Cluster at the Texas Advanced Computing Center.

For the homogeneous model, Young's modulus for each model was determined by using the average tissue modulus measured by indentation multiplied by the ratio between the sample's average TMD and the overall TMD of all the samples. For the heterogeneous model, Young's modulus was selected based on the experimentally measured TMD-to-modulus correlation in the axial direction (Figure 3.6 solid line), in the lateral direction (Figure 3.6 dash line), and the overall TMD-to-modulus correction with pooled data as shown below.

Axial $$E = 0.021 \bullet TMD - 4.80 \quad (4.1)$$

Lateral $$E = 0.014 \bullet TMD - 0.74 \quad (4.2)$$

Pooled $$E = 0.018 \bullet TMD - 2.68 \quad (4.3)$$

Therefore, for each sample, there were three heterogeneous models generated. The grayscale value-to-TMD correlation was based on *in situ* density calibration phantom sets. Each voxel was assigned a different modulus based on its grayscale-to-TMD conversion. There was no additional scaling involved in either of the two models.

4.2.4. Development of anisotropic and heterogeneous μFE voxel model

The development of anisotropic and heterogeneous voxel models was also based on the μCT images. After scanning, for each sample, one grayscale image (original) and one segmented image (after thresholding) were generated. The segmented image was subjected to ITS analysis. The trabecular type and trabecular anatomic orientation of each voxel were recorded. From the grayscale image, the TMD of each voxel was calculated based on a calibration curve from density phantoms. Each local trabecular plate or rod was first considered to have a local coordinate. According to Hooke's law, the constitutive law was implemented to each voxel based on each local coordinate with a compliance matrix as shown in Figure 4.1. In this study, based on the suggested transversely isotropic tissue material properties of both plate and rod from Chapter 3, the independent variables of the compliance matrix is reduced to five: axial modulus, lateral modulus, axial Poisson's ratio, lateral Poisson's ratio, and shear modulus in the lateral direction. The axial and lateral moduli were assigned based on experimentally obtained TMD-to-modulus relationships from equation 4.1 and equation 4.2. The Poisson's ratio in both axial and lateral directions was assumed to be 0.3. The ratio of the shear modulus in the two directions was assumed to be a constant (Dong and Guo 2004), where

$$G_{axi} = \frac{2(1 + v_{axi})}{E_{axi}} \tag{4.3}$$

Afterward, the material properties defined in each local coordinate were converted to the global coordinate of the bone sample based on a fourth order tensor. A uniaxial compression test was simulated in the μFE analysis, and fixed boundary conditions were assigned to the nodes at the two ends of the model. A displacement equivalent to 1% strain was applied in the axial direction. The tissue-level yield strains were assumed to be 0.81% of strain in tension and

compression (Bayraktar, Morgan et al. 2004). The post-yield tissue modulus was 5% of its initial value. In summary, except the Young's modulus input, all the other conditions of the three types of FE models were the same. The anisotropic model was validated on a solid cube sample by rotating a random degree and a regular cubic trabecular bone core by rotating 90 degrees in all the directions.

4.2.5. Mechanical testing

The mechanical testing was precisely adopted from our lab's previous study(Wang, Zhou et al. 2015). After μCT scanning, the bone marrow near the two ends of the bone cores was cleaned with a water jet. The specimens were then glued into customized brass cylindrical end caps with the inner diameter the same as the diameter of trabecular bone cores. The specimens were pushed to the bottom of the end cap to eliminate movement during mechanical testing and to reduce end-artifacts (Keaveny, Guo et al. 1994). A uniaxial compression test was performed on each core at room temperature while keeping the specimen hydrated to measure the mechanical properties (MTS 810, Eden Prairie, MN). An 8 mm strain gage was attached to the middle of the specimen to measure strain. To ensure uniform deformations between the end caps and no yielding at the end cap-bone interface, a 25 mm extensometer (MTS 634.11F-24) was attached to the end caps. The specimen was preconditioned by three cycles with a 0.05% strain per second loading speed and a final ramp beyond the yield point. The elastic modulus was calculated by the linear curve fit within a 0-0.2% strain range. The yield strength and the yield strain were calculated using a 0.2% offset technique (Keaveny, Guo et al. 1994).

4.2.6. Statistical Analyses

Statistical analyses were performed using NCSS software (NCSS 2007, NCSS Statistical Software, Kaysville, Utah). The stiffness measurements predicted by different FE models as well

as measured by mechanical testing were correlated with each other through linear regression. In the bar charts, the simulated stiffness and yield strength were presented in the form of mean ± standard deviation. Multiple linear regression analysis was used to evaluate if two correlations were different. Two-sided p values <0.05 were considered to indicate statistical significance.

4.3. Results

4.3.1. Elastic modulus and yield strength predicted by homogeneous/isotropic model and heterogeneous/anisotropic model compared to mechanical testing

The elastic modulus predicted by the anisotropic model was strongly correlated with that predicted by mechanical testing (R^2 = 0.98). However, the correlation of determination was not higher than that between the isotropic model and mechanical testing (R^2 =0.99), suggesting that the prediction power of voxel FE model does not improve by including the anisotropic modulus, as shown in Figure 4.2.A. The yield strength predicted by anisotropic model was also strongly correlated with that predicted by mechanical testing (R^2 = 0.96). Compared to homogeneous/isotropic model, the heterogeneous/anisotropic model predicted higher yield strength.

4.3.2. Elastic modulus and yield strength predicted by heterogeneous/isotropic model and heterogeneous/anisotropic model compared to mechanical testing

The elastic modulus predicted by heterogeneous and isotropic models with all different Young's modulus profiles were highly correlated with mechanical testing (R^2 = 0.99). However, the elastic modulus predicted by the heterogeneous model with axial Young's modulus was overestimated. The axial model vastly overestimated the elastic modulus, while the lateral model greatly underestimated the stiffness in the z-direction. The correlation between the anisotropic

model and mechanical testing has a slope that is close to 1, indicating an improvement in the accuracy of the prediction. The anisotropic modulus predicted higher yield strength than the heterogeneous model with pooled modulus and lateral modulus. However, the predicted yield strength was indistinguishable between the anisotropic/ heterogeneous model and isotropic/ heterogeneous model with axial modulus.

4.4. Discussion

In this chapter, the μCT-based μFE voxel modeling was extended in two dimensions: first, an experimentally obtained TMD-to-Young's modulus correlation was used to examine the accuracy of the model, and second, the anisotropic and heterogeneous tissue material properties were incorporated into the voxel model. The anisotropic and heterogeneous models were compared with isotropic and homogeneous models, isotropic and heterogeneous models, and mechanical testing for predicting apparent stiffness and yield strength. Overall, the predictions of the anisotropic and heterogeneous model in mechanical properties were identical to mechanical testing measurements, without any extra adjustments on the scaling of tissue modulus, which in turn serves as a piece of strong evidence of the existence of tissue level anisotropic Young's modulus.

Although the anisotropic and heterogeneous Young's modulus of individual trabecular bone was suggested separately in the past, this study is the first time to utilize an experimentally obtained Young's modulus that possesses both material properties into a μFE model. Wolfram et al. tested rod-like trabecular bone with nano-indentation and found a higher modulus in the axial direction compared to the transverse direction (Wolfram, Wilke et al. 2010). However, not a single study has incorporated tissue-level anisotropy of trabecular bone into the prediction of

apparent-level mechanical properties. Separately, heterogeneous models have been suggested to underestimate the apparent stiffness and yield strength (van der Linden, Birkenhager-Frenkel et al. 2001, Jaasma, Bayraktar et al. 2002), which is consistent with this study. The heterogeneous model with pooled TMD-to-Young's modulus relationship showed a reduction in the prediction compared to the measurements by gold standard mechanical testing. However, this study provides an explanation that the previous studies did not underestimate the apparent level mechanical properties by assuming an unrealistic heterogeneity. Instead, it was due to the omission of the tissue level anisotropy for individual trabecular bone. It can be interpreted as follows: the loading environment not only shapes the anisotropic trabecular morphology at the structure level, but it also affects the tissue-level anisotropy of the elastic modulus.

Nonetheless, it was not surprising to see that the inclusion of the mechanically obtained tissue-level Young's modulus did not improve the prediction power of the μFE models, which suggests the tissue level heterogeneity and anisotropy are not as important predictors as morphological parameters for the apparent level mechanical behaviors. However, the differences in the absolute values of the predictions between the heterogeneous/anisotropic model and the heterogeneous/isotropic models were truly reflective of the anisotropy of both the tissue-level material properties and trabecular bone alignments. In all the loading sites, the majority of trabecular bone aligns along the loading direction, and the distribution of trabecular bone shares a very similar pattern (Liu, Sajda et al. 2006, Liu, Sajda et al. 2008). The anisotropy of the tissue material properties essentially aligns with the anisotropy of trabecular directions. It would be interesting to see in certain diseases, such as osteoarthritis where the anisotropy of trabecular bone alignment is further amplified, whether the addition of anisotropic tissue material properties

might significantly affect the whole bone mechanical behaviors in terms of both prediction power and accuracy.

In terms of the yield strength prediction, it appears both the anisotropy and heterogeneity tend to predict higher yield strength compared to homogeneous/isotropic model. For heterogeneity, a possible explanation is that due to the adaptation, mineralization tends to be higher in the critical loading sites, and counting the heterogeneity at those sites tends to increase the bone's capability to resist yield. Also, at weak sites, due to the heterogeneity, the tissue level yield resistance does not compromise much because the locally higher modulus compensate the lower modulus and make the overall modulus doesn't go down much and therefore, the capability of assuming load remains. For anisotropy, the same explanation stands. It will be interesting to analyze the post yield behavior based on these different tissue modulus distribution that might play a more important role.

In summary, this chapter of the thesis represents a conclusive milestone for the researcher who studies the tissue material properties with both basic science and clinical perspectives. Our results indicate the inclusion of anisotropy and heterogeneity does not contribute to the prediction power of apparent level stiffness or strength, suggesting that the clinical assessment of bone does not need to focus on the tissue level material properties. In addition, the fact that μFE models with an experimentally obtained modulus predict the apparent level mechanical properties no better or worse than the current standard homogeneous/isotropic models further strengthens the potential of the current clinical μCT-based biomechanical assessments. Further, research areas such as reference point indentation-based bone material property assessments are not likely to reflect the whole bone-level mechanical behaviors.

Table 4.1. Donor and sample information in the experimental set.

Anatomic site	*No. Specimens*	*No. Donors (male/female)*	*Age (year)*	*BV/TV*
Proximal tibia	20	11 (10/1)	65±7	0.097±0.03
Femoral neck	20	13 (7/6)	72±15	0.28±0.10
Greater Trochanter	20	12 (8/4)	73±13	0.085±0.032

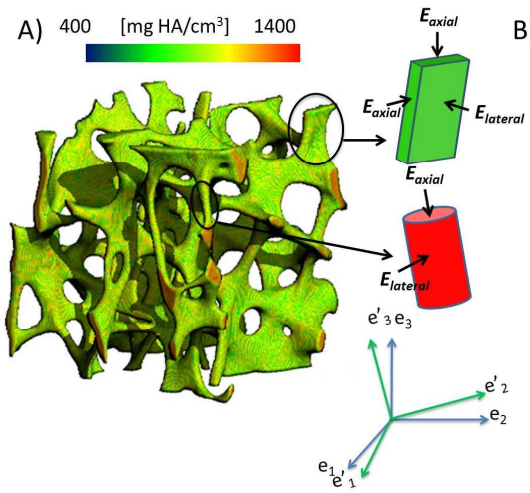

B)

$$\begin{bmatrix} \frac{1}{E_{axi}} & -\frac{v_{axi}}{E_{axi}} & -\frac{v_{Lat}}{E_{Lat}} & 0 & 0 & 0 \\ -\frac{v_{axi}}{E_{axi}} & \frac{1}{E_{axi}} & -\frac{v_{Lat}}{E_{Lat}} & 0 & 0 & 0 \\ -\frac{v_{axi}}{E_{axi}} & -\frac{v_{axi}}{E_{axi}} & \frac{1}{E_{Lat}} & 0 & 0 & 0 \\ 0 & 0 & 0 & \frac{1}{G_{Lat}} & 0 & 0 \\ 0 & 0 & 0 & 0 & \frac{1}{G_{Lat}} & 0 \\ 0 & 0 & 0 & 0 & 0 & \frac{2(1+v_{axi})}{E_{axi}} \end{bmatrix}$$

Figure 4.1. Compliance matrix and local-to-global coordinates transformation. E_{axi} : axial modulus; E_{lat}: lateral modulus; ν_{axi}: Poisson's ratio in axial direction, ν_{lat}: Poisson's ratio in lateral direction; G_{Lat}: shear modulus in lateral direction

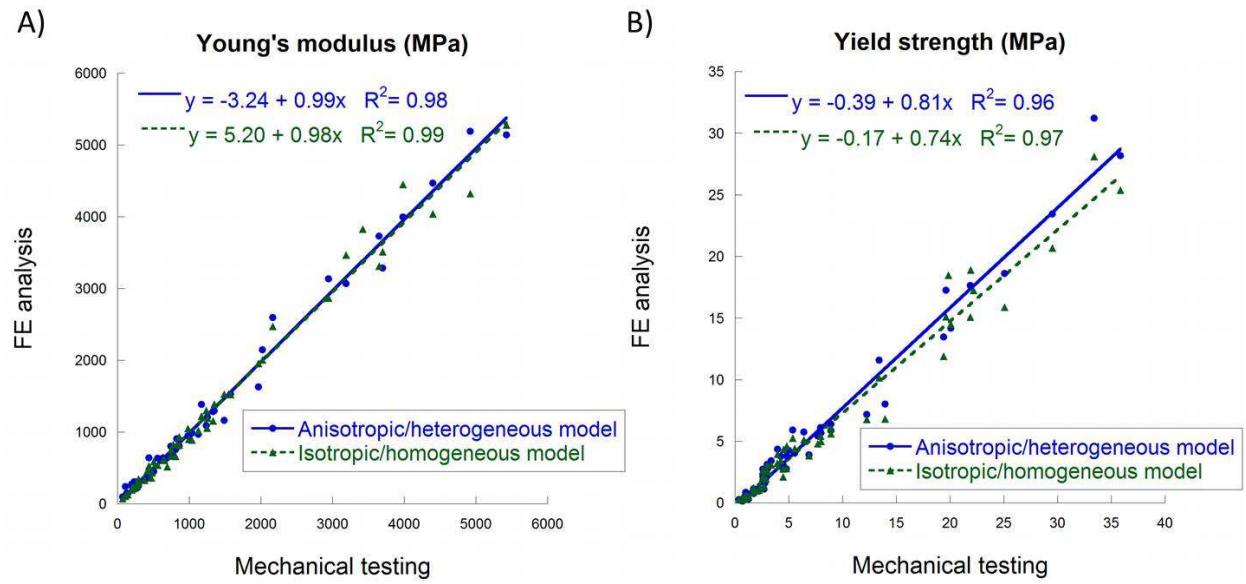

Figure 4.2 Linear regression of A) Young's modulus and B) between predictions by isotropic model, anisotropic model, and measurements by mechanical testing.

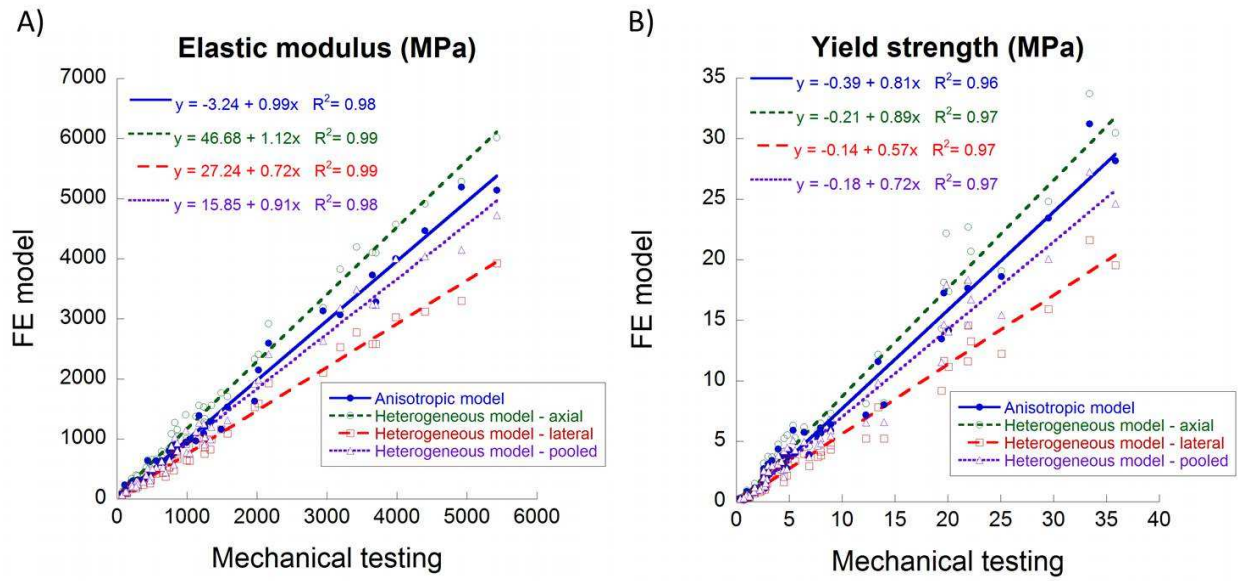

Figure 4.3. Linear regression of A) Young's modulus and B) yield strength between predictions by heterogeneous/isotropic models, heterogeneous/anisotropic model, and measurements by mechanical testing.

Chapter 5. Tissue material properties of adolescent idiopathic scoliosis patients

5.1. Introduction

Adolescent idiopathic scoliosis (Bacchetta, Boutroy et al.) is a three-dimensional (3D) spinal deformity occurring mainly in girls with a prevalence of 2-4% worldwide (Weinstein 1989). The etiopathogenesis of AIS remains largely unknown. From a biomechanical perspective, aBMD and microstructural abnormalities might provide additional insights. AIS patients are known to be associated with a lower bone mass that can persist into adult life (Cheng and Guo 1997, Cheng, Guo et al. 1999). It was also observed that osteopenic AIS was associated with larger curve magnitude and higher risk of curve progression compared to non-osteopenic AIS (Hung, Qin et al. 2005) A recent clinical μCT study demonstrated that AIS is also associated with a lower trabecular number and greater trabecular bone separation (Yu, Chan et al. 2014), indicating abnormal trabecular bone formation that might relate to the malfunctions in the modulation of bone mineralization (Rauch, Travers et al. 2000). These bone mass and microstructural changes, although not conclusive, could imply underlying abnormal bone metabolism in AIS, which might result in decreased bone strength that could contribute to initiation or progression of the spinal deformity.

To further understand the detailed plate- and rod-related bone microstructure, Cheuk et al. recently reported a trabecular plate and rod derangement in the loading direction similar to that of idiopathic osteoporosis (Liu, Cohen et al. 2010, Cheuk KY 2016), when compared to normal controls. Axially-aligned trabecular bone provides the primary support for loading (Liu, Zhang et

al. 2009, Shi, Liu et al. 2010). Therefore, this derangement of trabecular bone microstructure could initiate a change in the loading environment that collectively results in eventual spinal deformity, or even immediately results in spinal deformity, as 75% of spine is composed of trabecular bone. In addition, the tissue material properties of AIS patients have been barely studied. AIS occurs mostly in girls at the age of 10-13, which coincides with the fast growth period when the bone tissue is still compliant compared with adults (Weinstein 1989). It has been reported that the rapid bone modeling and delayed mineral accrual during puberty might result in transient low bone mass and bone weakness (Wang, Alen et al. 2005, Wang, Wang et al. 2010). A closer look at these derangements in trabecular alignment, specifically the direction-related trabecular level compositional and mechanical properties, might give additional insights into mechanisms underlying this disease.

The objective of this study was to investigate differences in the composition and tissue-level mechanics between AIS and non-AIS control and to examine how the tissue-level mechanical properties affect apparent level mechanics.

5.2. Materials and Methods

5.2.1. Subjects

Fourteen AIS patients with severe scoliosis undergoing posterior instrumentation and spinal fusion surgery were recruited from the Joint Scoliosis Research Center of the Chinese University of Hong Kong. The diagnosis was confirmed clinically and radiologically with standing full-spine posteroanterior X-ray radiographs after excluding other possible causes of scoliosis. Five ethnic-matched non-AIS adolescents without diseases affecting bone metabolism

and in need of iliac crest autograft as part of their orthopaedic surgical procedure were recruited as controls. The exclusion criteria were as follows: (a) other scoliosis, such as congenital scoliosis, neurofibromatosis, ankylosing spondylitis, or syringomyelia with scoliosis; (b) any medical conditions that affected bone metabolism, such as hyperparathyroidism and acute or chronic renal disease; (c) receiving drug treatment that affected bone metabolism, such as bisphosphonate and steroids; (d) history of operation that would affect bone metabolism, such as the hepatic surgery; (e) malignant bone tumors such as osteosarcomas; (f) presence of any implants that affected BMD measurement; and (g) pregnancy or malabsorption history.

The demographic assessments along with body weight and bone volume fraction were measured. Curve severity was graded with standard Cobb angle of the major curve on the standard full-spine radiograph. Areal BMD (aBMD) of the femoral neck on the concave side of the major curve in AIS was measured by DXA (XR-36; Norland Medical Systems, Fort Atkinson, WI, USA). For controls, aBMD was measured at the non-dominant femoral neck. A normative BMD dataset of local ethnic Chinese was used for the calculation of the age- and gender-adjusted Z-score (6). All the parameters above are presented in Table 5.1.

Informed consents to obtain bone biopsy during operation were obtained before the surgery. Clinical ethical approval was obtained from the Ethical Committee of the university and the hospital (CREC-2012.528). Standardized trabecular bone biopsies of roughly 5 x 5 x 5 mm^3 in size were obtained from the posterior part of the ilium of AIS patients and controls at 2 cm below iliac crest and 2 cm in front of the posterior-superior iliac spine intraoperatively as part of the autograft harvesting procedure.

Due to the preserved conditions and the actual size of the samples after previous experiments, 7 AIS and four control samples were used for indentation. AIS samples had a Z score of -0.87 ± 0.84, and control samples had a Z score of -1.72 ±0.45. The overall age range was 14.9±1.9. The average TMD was 548.6 ±28.1 mg HA/cm^3 for the AIS patients and 518.2±13.3 mg HA/cm^3 for the control group. Detailed preparation procedures, including cleaning, embedding, polishing, and storage were described in detail in Chapter 3.2.1.

5.2.2. µCT

The original cubic specimens were then subjected to a µCT scan (µCT 40, Scanco, Brüttisellen, Switzerland) at a voltage of 70 kVp with a current of 114 µA at an isotropic voxel size of 10.5 µm (Bouxsein, Boyd et al. 2010). A low-pass Gaussian filter (Sigma=0.8; Support=1) was applied to reduce the noise signal. Due to the irregular shape of bone biopsy and in order to standardize the volume of interest in evaluation, a 4 x 4 x 4 mm^3 cubic sub-volume of samples was contoured for standard µCT microstructural analysis, ITS analysis, and FEA. The bone volume fraction (BV/TV), material bone mineral density (mBMD) and volumetric bone mineral density (vBMD) are shown in Table 5.1. A sample-specific adaptive thresholding technique was applied to convert gray scale images into binary images using the standard analysis protocol provided by Scanco.

The embedded specimens were scanned again at the same voxel size but increased integration time at 600ms to improve the signal noise ratio for TMD measurements. A set of 5 density calibration phantoms (CIRS, Norfolk, Virginia) was scanned with the samples for *in situ* calibration of the attenuation-to-TMD relationship.

5.2.3. ITS

The detailed process of ITS was described in previous work (Liu, Sajda et al. 2008). Briefly, the 3D segmented trabecular bone images were completely decomposed by digital topologic analysis (DTA)-based skeletonization and reconstructed by an iterative reconstruction method. Based on the evaluations of dimension and orientation of each individual trabecular plate and rod, as well as junctions of surface and curve skeletons, a set of ITS-based morphological parameters was derived to quantify plate and rod bone volume fraction (BV/TV, pBV/TV and rBV/TV), plate-to-rod ratio (P-R ratio), that is, the ratio of plate bone tissue divided by rod bone tissue, plate and rod numerical density (pTb.N and rTb.N, mm^{-1}), plate and rod thickness (pTb.Th and rTb.Th, mm), plate surface area (pTb.S, mm^2), rod length (rTb.L, mm), and rod-rod, plate-rod, and plate-plate junction density (R-R, P-R, and P-P Junc.D, mm^{-3}).

5.2.4. Microindentation

On each sample, 20 indentations were performed on 8-10 randomly selected trabeculae. Each indentation was at least 50μm away from each other and from the boundary of a bone to minimize the boundary effect. The selection of the trabecular bone did not take plate and rod types into consideration. The sample was kept wet by Gentamicin solution during the indentation procedure. The calculation of the Young's modulus and the procedures for indentation has been described in Chapter 3.2.3. A photo of each selected trabecula was taken by light microscopy before and after the indentation to confirm the indentation locations. Indents made on lacunae were excluded from the study.

5.2.5. FE analyses

Three μFE models were generated for each specimen with different bone tissue properties: (1) homogeneous model with a global tissue modulus; (2) homogeneous model with a sample-specific tissue modulus scaled by average TMD measured by μCT; and (3) heterogeneous model.

In the homogeneous model (1), the global tissue modulus was assigned as the average indentation modulus for each patient group. In the specimen-specific homogeneous FE, a different tissue modulus was assigned to each specimen scaling from the average TMD of each sample. In the heterogeneous FE model, each bone element was assigned with a different Young's modulus by using a linear attenuation-to-tissue modulus relationship based on indentation results. The detailed Young's modulus assignment is described in Chapter 4.2.3. The bone in all the FE models was defined as an isotopic material with a Poisson's ratio of 0.3 (van Rietbergen, Weinans et al. 1995). The linear analysis was performed on FAIM, FE analysis software specifically designed for compatibility of bone μCT images by bone imaging lab of University of Calgary (http://www.numerics88.com/n88/faim.html). A uni-axial compression test was simulated to calculate apparent modulus. A displacement equivalent to 1% strain was applied in the axial direction. The elastic modulus of each sample was calculated by the linear curve fit within a 0-0.2% strain range.

5.2.6. Statistical analysis

All data is expressed as mean ± standard deviation. Mann–Whitney U test was used for testing. All the statistical analysis was performed with SPSS 17.0 software (SPSS, Inc., Chicago, IL, USA). A multivariate ANOVA was performed to examine the difference in TMD-adjusted

Young's modulus between plates and rods of different anatomic directions. $p<0.05$ was considered statistically significant.

5.3. Results

5.3.1. Microstructural results

ITS results revealed most parameters, including BV/TV, pBV/TV and rBV/TV, pTb.N and rTb.N, were not different between AIS and non-AIS control. Significantly higher plate thickness (p=0.012) and numerically higher rod thickness (p=0.052) was observed in AIS when compared with control. In addition, a significant decrease in the rod-rod junction connectivity was detected in AIS than in control (p=0.033). Rod-plate and plate-plate junction connectivity also decreased in AIS, but did reaching statistical significance.

5.3.2. Microindentation results

In total, 220 indentations were made. 28 indentations performed on lacunae were discarded; therefore, a total of 192 indentations were used for analysis. Overall, no difference was detected in the indentation modulus between AIS and the control group (p=0.28). The co-localized TMD was also not different between the two groups (p=0.55), as shown in Figure 5.1. The tissue modulus moderately correlates to TMD in both groups (Figure 5.2 A, B). However, no differences were found between the two groups and therefore the data was pooled together for an overall TMD-to-modulus correlation (Fig 5.2 C).

5.3.3. FE results

As shown in Table 5.3, AIS bone tissue exhibited numerically slightly lower apparent modulus when compared with control as indicated in all the homogeneous and heterogeneous FE

models; however, the differences did not reach statistical significance. The heterogeneous FE-predicted apparent level Young's modulus was also strongly correlated with that predicted by the sample-specific homogeneous model ($R^2 = 0.93$, Figure 5.2.D)

5.4. Discussion

In this study, the tissue modulus and microstructural differences were studied between AIS patients and non-AIS controls. Morphologically, no major difference was found in either pBV/TV nor rBV/TV. However, pTb. Th was significantly higher in AIS while R-R junc. D was more than 50% lower than in the control group. The higher pTb. Th was compensated by a similar percentage decrease in pTb. N, although not significant. On the tissue level, no difference was found in the Young's modulus or co-localized TMD. This is consistent with the overall mBMD measurements. It was not surprising that the overall apparent level modulus did not different when the microstructural and tissue level Young's modulus was not different.

Recent cross-sectional studies with HR-pQCT measurements at the non-dominant distal radius showed significant differences in Tb.N and Tb.Th between AIS patients and controls after adjusting for age and aBMD (Wang, Lee et al. 2016). The trabecular alterations were also observable in the present study after segmenting into rod-like and plate-like trabeculae. In summary, ITS analysis revealed predominant loss of connectivity between rod-like trabecular bone and abnormal plate thickness in AIS. Studies have shown that aging-related change towards more rod-like configuration is associated with bone mechanical deterioration (Ding and Hvid 2000, Liu, Sajda et al. 2006). On the contrary, the observed plate and rod configuration changes in AIS are unique and differ from other reports in premenopausal women with idiopathic

osteoporosis (IOP)(Liu, Cohen et al. 2010). Unlike IOP with predominant reduction in pBV/TV (-41.5%) but less in rBV/TV (-22.8%), AIS showed relatively more reduction in rBV/TV (-19.2%) than pBV/TV (-5.9%). Significant reduction in rod-to-rod connectivity was also observed in AIS. However, the microstructural changes in AIS only resulted in numerical reductions in the apparent modulus in AIS with various tested FE models.

On the tissue level, neither tissue modulus nor TMD was different between AIS and control. TMD and modulus were correlated moderately in both control and AIS. However, the correlation was not different. However, it is interesting to compare these results with results from Chapter 3. The average modulus and TMD in this study is 3.90 GPa and 677.4 mg HA/cm^3, compared to 14.1 GPa and 998.7 mg HA/cm^3 in elderly bone. Also, compared to the TMD-to-modulus correlation in this study, the slope of the correlation in Chapter 3 was much steeper. These results indicate that the mineral content plays different roles in adolescent and adult bone, as the matured bone tissue with only ~50% of the increase in TMD resulted in an almost 3-fold increase in the modulus compared to adolescent bone. It could be attributed to the maturation of the crystal, collagen cross-linking, and the interaction between the mineral and collagen. On the apparent level, the Young's modulus was not different between AIS and control subjects in any of the three prediction models. But numerically, with smaller BV/TV and tissue modulus, the overall apparent modulus could be reduced by a higher proportion compared to adult bone. It was not surprising that the predicted apparent modulus was not different between the three different models, as the tissue level heterogeneity does not contribute much. The specimen-specific homogeneous model and heterogeneous model predicted apparent modulus was highly

correlated with each other, and the slope of the correlation was close to 1, which further supports the underlying tissue level heterogeneity doesn't play a notable role in apparent level mechanics.

Several limitations are associated with this study. First, due to the difficulties in collecting age-matched non-AIS control biopsies, only four samples were used as controls in the indentation tests. At the same time, the Z-scores of the control samples were as low as the AIS samples. The mBMD in the AIS group was numerically even higher. This could potentially bias the indentation results. Also, only five control samples were used in ITS, which limits the characterization of plate and rod microstructural changes. Furthermore, the control samples were from non-AIS patents instead of healthy controls. Most of the controls also have osteopenia diagnosed by DXA. Second, the accuracy of ITS and FE analyses could be greater if the dimensions of the samples were higher. However, for ethical considerations, iliac crest bone biopsies were only collected as part of many trabecular bone strips during autograft harvesting for spinal fusion, rather than as standard transiliac crest bone core biopsies. The bone biopsies were thus less uniform in size and shape, and only 4 x 4 x 4 mm^3 cubic sub-volumes of the μCT images were analyzed for ITS and FEA.

Overall, this chapter serves as an application study that discovers the potential for mechanical differences at both tissue and apparent levels. Although this study suggests the tissue-level material properties are not likely to contribute or be affected by AIS pathogenesis, the differences in the contribution of mineral density to tissue modulus between growing and adults bone were demonstrated. Clearly, for a younger group of patients, the tissue-level properties should be carefully considered before moving into FE predictions.

Table 5.1 Sample information including age, spine curve angle, bone mass Z-score, and standard μCT measurements.

Parameters	**AIS** **N = 14**	**Con** **N = 5**	***p* value**
Age (years)	14.8 ± 1.89	14.5 ± 4.13	0.591
Major curve (°)	52.7 ± 10.05	-	-
Z-score of aBMD	-0.96 ± 0.72	-0.91 ± 1.19	0.751
BV/TV	0.18 ± 0.033	0.19 ± 0.035	0.405
mBMD(mg HA/cm^3)	634.98 ± 33.559	629.52 ± 40.824	0.926
vBMD(mg HA/cm^3)	137.88 ± 30.152	152.23 ± 37.860	0.517

Table 5.2 Trabecular micro-architecture measured with ITS in AIS and controls. Difference %= (AIS-control)/control %.

Parameters	**AIS** ***N*=14**	**Con** ***N*=5**	**% difference**	***p* value**
pBV/TV	0.16 ± 0.027	0.17 ± 0.026	-5.88	0.517
rBV/TV	0.021 ± 0.008	0.026 ± 0.014	-19.23	0.459
pBV/BV	0.88 ± 0.026	0.87 ± 0.05	1.15	0.781
rBV/BV	0.117 ± 0.026	0.131 ± 0.05	-10.69	0.781
P-R ratio	7.93 ± 1.928	7.31 ± 2.305	8.48	0.781
pTb.N (mm^{-1})	4.10 ± 0.27	4.38 ± 0.387	-6.39	0.139
rTb.N (mm^{-1})	2.90 ± 0.317	3.26 ± 0.716	-11.04	0.229
pTb.Th (mm)	0.087 ± 0.003	0.082 ± 0.003	**6.1**	**0.012**
rTb.Th (mm)	0.065 ± 0.003	0.062 ± 0.004	4.84	0.052
pTb.S (mm^2)	0.026 ± 0.002	0.024 ± 0.003	8.33	0.165
rTb.L (mm)	0.215 ± 0.012	0.211 ± 0.004	1.9	0.926
R-R Junc.D (mm^{-3})	7.84 ± 2.568	18.19 ± 18.765	**-56.9**	**0.033**
R-P Junc.D (mm^{-3})	76.82 ± 24.618	103.82 ± 56.032	-26	0.267
P-P Junc.D (mm^{-3})	71.34 ± 18.528	94.57 ± 40.344	-24.56	0.229

Table 5.3 Apparent modulus in AIS and controls calculated by homogeneous and heterogeneous FE analysis. Difference %= (AIS-control)/control %

Apparent modulus (MPa)	**AIS *N*=14**	**Con *N*=5**	**% difference**	***p* value**
Homogeneous FEA with global tissue modulus	96.78 ± 47.04	107.20 ± 36.67	-9.72	0.517
Homogeneous FEA with sample specific modulus	97.41 ± 49.62	105.57 ± 33.11	-7.73	0.355
Heterogeneous FEA	93.79 ± 51.80	100.58 ± 31.34	-6.75	0.405

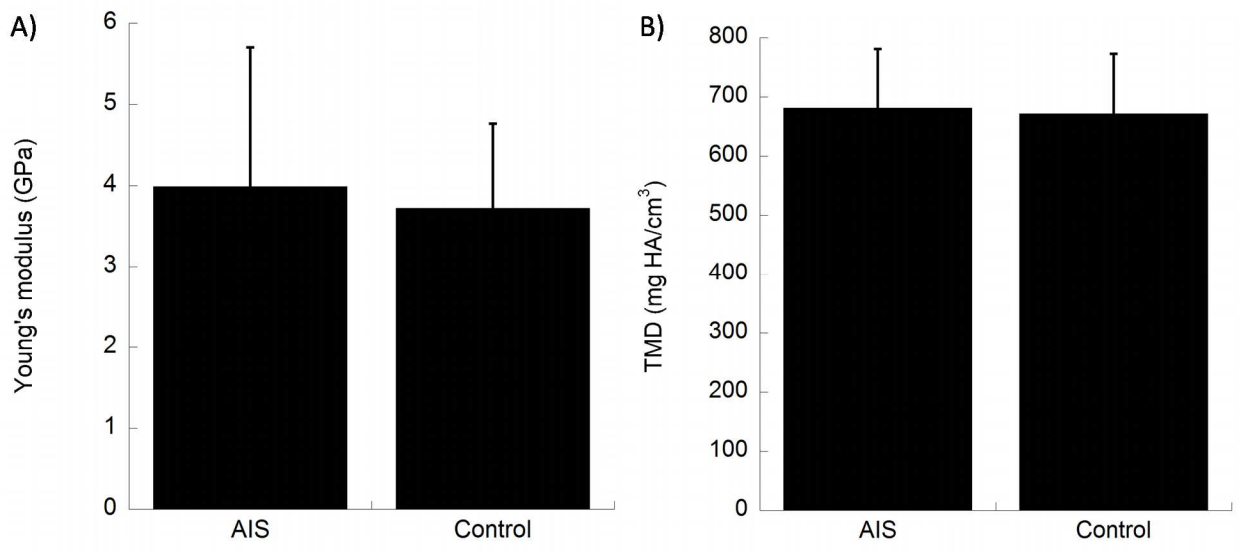

Figure 5.1. Comparisons of Young's modulus and co-localized TMD between AIS and control

A) Comparison of Young's modulus between trabecular plates and rods. p=0.28
B) Comparison of co-localized TMD between trabecular plates and rods. p=0.55

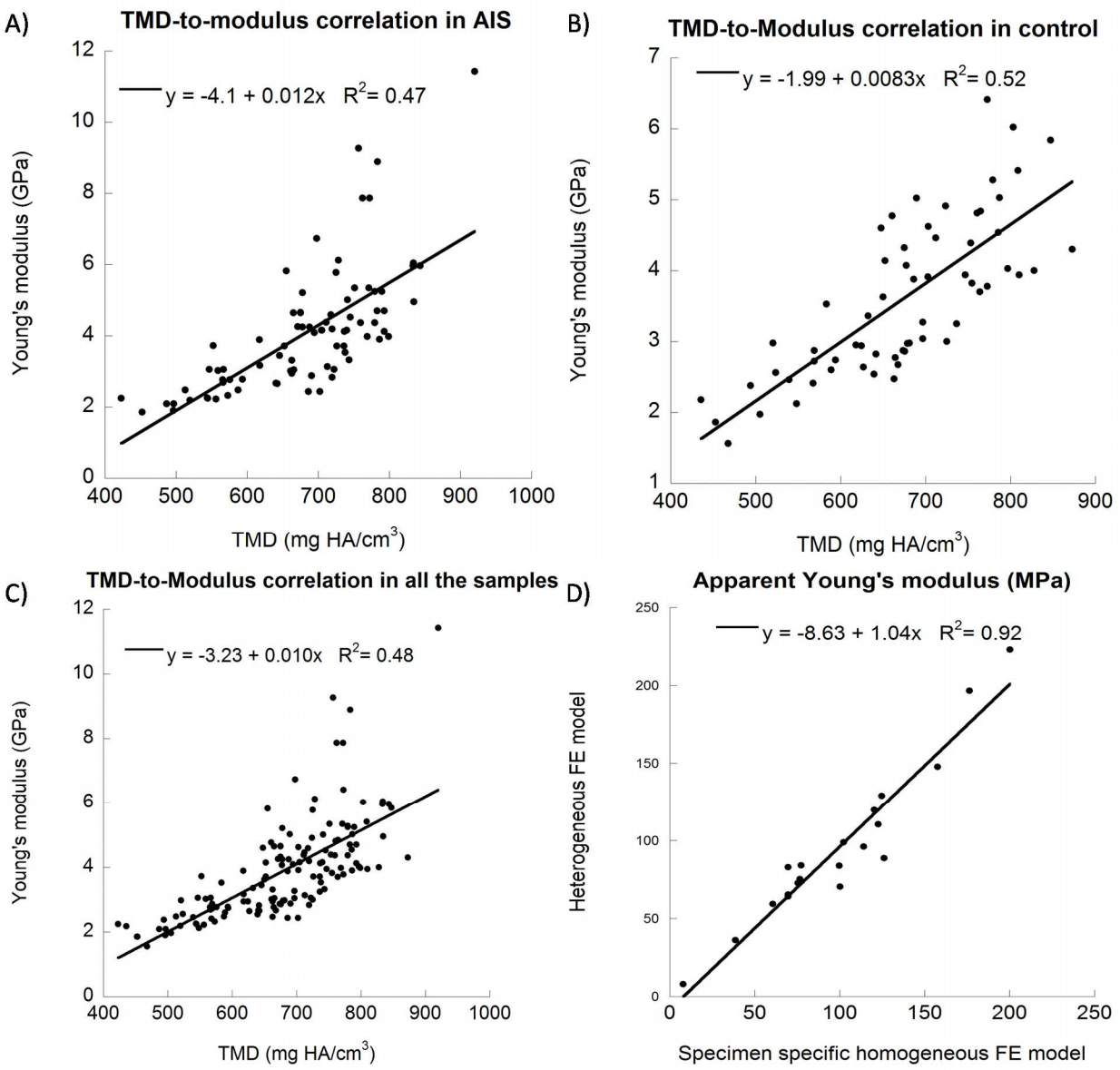

Figure 5.2. Correlations between tissue modulus and TMD in A) AIS, B) control, and C) overall samples, as well as D) correlation between apparent Young's modulus predicted by two types of FE models.

Chapter 6. Tissue material properties and microstructural changes in subchondral bone in osteoarthritis with/without type 2 diabetes

6.1. Introduction

Osteoarthritis (Bouxsein, Coan et al.) is a debilitating musculoskeletal disease that affects approximately 27 million aging adults, and type 2 diabetes mellitus (T2DM) is a group of metabolic diseases that affect over 21 million adults in US alone (Lawrence, Felson et al. 2008). The growing prevalence of T2DM and osteoarthritis among similar demographics indicates that both diseases are likely to appear simultaneously. Recent epidemiological evidence suggests that, despite possessing independent pathologies, this comorbidity (*i.e.,* T2DM/OA) might not be a mere coincidence; rather, there may be an underlying biological mechanism linking these two conditions (Schett, Kleyer et al. 2013).

Previous studies on bone microstructure and bone mineral density in these conditions have also been controversial. While some studies suggest that diabetes might induce or promote OA (King and Rosenthal 2015), others propose instead that OA may be a risk factor for diabetes (Rahman, Cibere et al. 2014). A possible connection might be joint overloading as diabetes is associated with obesity, a known risk factor for OA (Suri, Morgenroth et al. 2012). However, one population-based study found a strong correlation between T2DM and OA even in the non-load-bearing joints of the hand (Magnusson, Hagen et al. 2015), dismissing this hypothesis. Several groups have investigated the biochemical factors surrounding this comorbidity (Garcia-Martin, Rozas-Moreno et al. 2012, Gennari, Merlotti et al. 2012, Laiguillon, Courties et al. 2015). Other studies have focused on tissue-level changes in the knee joint. For example, Wen et al.

found that T2DM+OA caused lower bone mineral density and higher porosity in the subchondral plate of the proximal tibia (Wen, Chen et al. 2013).

However, no studies to date have investigated the effects of T2DM+OA on trabecular bone microstructure and tissue mechanical properties at the same time. Subchondral trabecular bone supports the loads exerted on the articulating joint surface. Cartilage erosion in OA may lead to localized overloading that damages the underlying trabecular bone. In turn, this weakened trabecular bone further perpetuates the altered mechanical environment, contributing to the progression of OA (Goldring and Goldring 2010, Chen 2016). At the same time, the subchondral trabecular bone is subjected to a series of metabolic activities that might differ between T2DM/OA and regular OA. For example, studies have suggested sclerostin levels are higher in diabetic patients (Garcia-Martin, Rozas-Moreno et al. 2012), especially in T2DM patients (Gennari, Merlotti et al. 2012). Furthermore, during the progression of OA, instead of promoting OA, the sclerosis development in T2DM/OA patients might be disrupted compared to regular OA. The higher sclerostin levels in T2DM could also reflect a prolonged lower bone turnover, which leads to defective microdamage repair, this postulated disruption in turnover can be captured by micro-indentation tests(Dall'Ara, Schmidt et al. 2012).

Therefore, by studying both the microstructure and tissue material properties, we might provide new insights into the pathogenesis of OA and the linkage between OA and T2DM. In this study, a comparison of bone quality, *i.e.,* plate and rod microstructure and tissue level material properties, between the two diseases, is carried out. The aim of this study is to determine whether T2DM/OA possesses a noticeable clinical delineation from OA alone based on microstructural analysis and micro-indentation testing.

6.2. Materials and Methods

6.2.1. Subjects

Tibial plateaus were collected from OA patients undergoing total knee replacement surgeries (regular OA: n=11, diabetic OA: n=8) and healthy cadaver donors (control: n=10). The patient's information is shown in Table 6.1. This study was reviewed and approved by the Institutional Review Board of the Hong Kong University. Subjects were screened to exclude history of metabolic bone disease or bone cancers. Intact, full-thickness cartilage covering the entire subchondral bone surface was observed in normal specimens, while severe cartilage damage was observed on the medial side of OA specimens. On the lateral side of the OA-affected tibial plateau, cartilage appears to remain mostly intact. The classification of the damage status was confirmed with μCT images and histology. Of these samples, 4 regular OA, 4 diabetic OA and 4 control samples were selected for indentation tests. For each sample, two cylindrical bone cores (~8.5 mm diameter, ~10 mm length) were harvested along the loading direction from the lateral intact and medial damaged regions. X-ray radiographs were taken on two orthogonal planes parallel with the longitudinal axis to confirm that the difference between the trabecular orientation and the longitudinal axis was no larger than 10°. The bone cores were sprayed with Gentamicin solution (Hoffler, Guo et al. 2005), wrapped with wet gauze, and kept in sealed plastic bags at −20 °C before experiments.

The cylindrical samples were cut with an Isomet low-speed saw (Buehler, Lake Bluff, IL). The segments with 5 mm length directly beneath the cartilage were saved for indentation. The preparation of the samples including cleaning, embedding, and polishing was described in detail

in Chapter 3.2.1. The polished sample was ~4mm in thickness and was prepared for μCT-based TMD measurements and then indentation tests.

6.2.2. μCT and ITS

Whole tibial plateaus were scanned by μCT (Skyscan) at an isotropic voxel size of 17 μm. Cubic regions (5 mm) were selected from subchondral trabecular bone directly beneath intact and severely damaged cartilage in each OA sample, as were the corresponding anatomic regions from control, as shown in Figure 6.1. These cubic regions were then segmented with a global threshold. The binary images were then subjected to ITS and homogeneous/isotropic finite element analysis.

The polished samples were scanned again by μCT (Scanco Viva 80, Scanco Medical AG, Switzerland) with a source potential of 55 kV and tube current of 109 μA at a voxel size of 10.5 μm and 600 ms integration time to achieve a high image quality for TMD measurements. A set of 5 density calibration phantoms (CIRS, Norfolk, Virginia) was scanned with the samples for *in situ* calibration of the attenuation-to-TMD relationship, as described in chapter 3.2.1.

ITS was performed on all the sub-regions. Bone volume fraction (BV/TV), plate bone volume fraction (pBV/TV), rod bone volume fraction (rBV/TV), plate number (pTb.N), rod number (rTb.N), plate thickness (Th. P) and rod thickness were assessed.

6.2.3. Microindentation tests

On each sample, 20 indentations were performed on 8-10 randomly selected trabeculae. Each indentation was at least 50μm away from each other and from the boundary of a bone to minimize the boundary effect. The selection of the trabecular bone did not take plate and rod

types into consideration. The samples were kept wet by Gentamicin solution during indentation procedure. The calculation of the Young's modulus and the procedures for indentation has been described in Chapter 3.2.3. A photo of each selected trabecula was taken by light microscopy before and after the indentation to confirm the indentation locations. Indents made on lacunae were excluded from the study.

6.2.4. μFE models

For each μCT image, one homogeneous model was generated. In the homogeneous model, a global tissue modulus for damaged region was assigned to the medial side regions of regular OA and T2DM/OA based on the average indentation modulus of the corresponding regions. For the control and lateral side of OA samples, a global tissue modulus from the average indentation tissue modulus of the corresponding regions was used. The bone in all the FE models was defined as an isotopic material with a Poisson's ratio of 0.3 (van Rietbergen, Weinans et al. 1995). A uni-axial compression test was simulated to calculate apparent modulus. A displacement equivalent to 1% strain was applied in the axial direction. The linear analysis was performed on FAIM, FE analysis software specifically designed for compatibility of bone μCT images by a bone imaging lab at the University of Calgary (http://www.numerics88.com/n88/faim.html).

6.2.5. Statistics

All data are expressed as mean ± SD. All the statistical analysis was performed with Kaleidagraph (Reading, PA. USA). One way ANOVA with Bonferroni post hoc analysis (alpha=0.05) was used to assess the differences in tissue modulus and microstructure between

medial and lateral side, and between T2DM/OA, OA and control groups. Statistical significance was set at 0.05.

6.3. Results

6.3.1. Microstructural differences

On the medial side where cartilage is mostly damaged, BV/TV and pBV/TV were significantly higher in regular OA compared to T2DM/OA ($p<0.01$), and significantly higher than control in both OA groups. No difference in rBV/TV between the three groups was discovered on the medial side as shown in Figure 6.2.A. On the lateral side where cartilage is mostly intact, microstructural analysis found no difference in bone volume fraction (BV/TV) and plate bone volume fraction (pBV/TV) between regular OA, T2DM/OA, and control. However, rod bone volume fraction (rBV/TV) was significantly lower in both regular OA and T2DM/OA (*$p<0.01$) compared to control, but no difference was found between the two OA groups, as shown in Figure 6.2.B. Detailed ITS results are shown in Table 6.2.

6.3.2. Microindentation results

For tissue mechanical properties, no difference between the three groups was found on the lateral side. On the medial side, however, both regular OA and T2DM/OA had lower tissue modulus than control (*$p<0.05$), while no difference was found between the two OA groups, as shown in 6.3.A. Interestingly, when comparing the lateral and medial side within each group, tissue modulus was significantly higher on the lateral side than on the medial side in both OA groups, while no difference was found between the medial and lateral side in control, as shown in 6.3.B

6.3.3. FE results

For finite element predicted apparent elastic modulus, no difference was found between regular OA, T2DM/OA and control on the lateral side. On the medial side, however, regular OA had significant higher apparent modulus than control and T2DM/OA (*$p<0.05$), as shown in Figure 6.4. Surprisingly no difference in elastic modulus were found between T2DM/OA and control on the medial side.

6.4. Discussion

This chapter of the thesis explores the bone quality differences in subchondral bone between regular OA, T2DM/OA, and control. Morphologically, on the lateral side where OA is considered mild, characterized by relatively intact cartilage, little difference in BV/TV and pBV/TV was discovered among the three groups. rBV/TV was significantly lower in both T2DM/OA and regular OA compared to control, suggesting rod loss is associated with the OA initialization. This is in line with previous microstructural characterizations of OA (Chen 2016). However, on the medial side where OA symptoms are more severe, BV/TV (which is predominantly pBV/TV) was significantly higher in regular OA compared to T2DM/OA. This difference indicates that, as OA progresses, bone microstructure in T2DM/OA might not be affected as greatly as that in regular OA. There could be multiple reasons for this observation. First, the T2DM/OA knee samples could have been obtained from patients at different stages of OA compared to regular OA. However, this is unlikely, as the replacement surgeries were all performed on end-stage OA patients. T2DM might associate with lower daily physical activities, which could be a minor contributor. A better confirmation of this finding would require a longitudinal study. Second, the biological responses in T2DM patients could prevent OA

progression to a certain extent. For example, Garci-Martin et al. showed that serum sclerostin levels in T2DM/OA patients are higher than in regular OA (Garcia-Martin, Rozas-Moreno et al. 2012). Sclerostin is known to have anti-anabolic effects on bone formation, which could lead to the lower bone volume fraction on the medial side in T2DM/OA compared to regular OA.

Differences in the tissue modulus between the two OA groups were not detected on either lateral or the medial side, suggesting T2DM does not affect tissue material properties in OA patients. However, it was interesting to see that the tissue modulus was lower on the medial side than on the lateral side in OA groups, suggesting that deterioration of tissue properties could be caused by poor mineralization or incomplete bone formation process associated with rapid development of bone sclerosis. The average TMD of the medial side bone tissue was lower than that of control sample as well as the TMD of lateral side for both control and OA, which supports the hypothesis. The lower modulus on the medial severe OA sites was consistent with other studies. Tomanik et al. studied the microhardness of bone tissue right under the cartilage in human femoral head and found a decrease in hardness associated with similar percentage of decrease in mineral density (Tomanik, Nikodem et al. 2016). Dall'Ala et al. also found reduced tissue hardness of trabecular bone in severe OA (Dall'Ara, Ohman et al. 2011). It is worth noting that, on the medial side, the tissue modulus in T2DM/OA, although not significant ($p=0.18$), was slightly higher than that in regular OA, given the small sample size. As there could be a slower development of sclerosis in T2DM supported by morphological data, there might be a trend of higher modulus in T2DM/OA.

The finite element results indicate a significant increase in the medial damaged regions of regular OA compared to the other regions, which is not surprising due to the higher bone volume

fraction. However, with a scrutiny of the values, with roughly twofold BV/TV and three fold pBV/TV in medial damaged regions compared to the medial control regions, the apparent elastic modulus of regular OA was only ~64% higher than that of control. However, this percentage was still higher than the percentage increase of 30%-50% in OA bone stiffness, which Li and Aspden suggested using on mechanical testing (Li and Aspden 1997). This can be likely explained by neglecting of the spatial inhomogeneous mineralization distribution. Especially at severe OA sites, the out layers of an individual trabecular bone are likely much more poorly mineralized than the central core region, which can cause the apparent stiffness decrease significantly compared to a homogeneous distribution with same mean TMD (van der Linden, Birkenhager-Frenkel et al. 2001). Surprisingly, on the medial side the elastic modulus of T2DM samples was not different from that of control samples. This might be explained by compromised tissue material properties compensated the higher bone volume fraction in T2DM samples, further support the hypothesis that D2TM might protect the OA subchondral bone from progression. However, this data needs to be interpreted with caution. Without considering the tissue material properties difference between T2DM and control, the apparent modulus of the medial side was actually different between T2DM and control (data obtained by linearly scaling up the T2DM apparent modulus). The decrease in tissue modulus in regular OA can be explained by the rapid development of sclerosis. However, in T2DM/OA, such development was delayed or hindered suggested by the ITS data. Nonetheless the tissue modulus was found no difference between T2DM/OA and regular OA on the medial side, suggesting that there might be other factors affected the measurements of tissue modulus in T2DM/OA samples. For example, accumulated

microdamage by T2DM bone tissue due to long term Wnt inhibition caused by higher sclerostin level can be detected by micro-indentation (Dall'Ara, Schmidt et al. 2012).

Overall, this study investigated differences in microstructural and tissue mechanical properties in subchondral bone between regular OA, T2DM/OA and control, which may help explain the linkage between and mechanisms underlying T2DM and OA. More broadly, this study indicates that the tissue material properties play an important role in determining apparent level bone mechanics for samples with disrupted bone pathological changes like OA. The microstructure changes induced apparent elastic modulus increase was pronouncedly compensated by the deterioration of tissue modulus. It will be interesting to thoroughly study the effect of anisotropic and heterogeneous tissue modulus on the apparent modulus in the future.

Table 6.1 Patient information and bone volume fraction of regular OA, T2DM/OA, and control for A) morphological analysis B) Indentation

Table A	Regular OA (N=11)	T2DM/OA (N=8)	Control (N=10)
Age	73.3 ± 11.4	69.7 ± 6.1	66.9 ± 12.1
Gender (F/M)	7/4	5/3	6/4

Table B	Regular OA (N=4)	T2DM/OA (N=4)	Control (N=4)
Age	72.0 ± 10.9	68.2 ± 8.1	67.5 ± 10.1
Gender (F/M)	2/2	2/2	2/2

Table 6.2 Detailed ITS results of the comparison between regular OA, T2DM/OA and control. * represents significant difference from control and # represents significant difference tween T2MD/OA and regular OA. *p<0.05, #p<0.05

	Medial			Lateral		
Mean ± SD	Regular OA	T2DM + OA	Control	Regular OA	T2DM + OA	Control
BV/TV	0.297 ± 0.068*#	0.232 ± 0.086*	0.149 ± 0.067	0.158 ± 0.089	0.151 ± 0.053	0.151 ± 0.054
pBV/TV	0.236 ± 0.062*#	0.175 ± 0.088*	0.088 ± 0.057	0.122 ± 0.085	0.119 ± 0.051*	0.085 ± 0.047
rBV/TV	0.06 ± 0.018	0.056 ± 0.014	0.062 ± 0.023	0.036 ± 0.014*	0.032 ± 0.013*	0.051 ± 0.016
aBV/TV	0.13 ± 0.034*#	0.092 ± 0.042*	0.059 ± 0.036	0.064 ± 0.046	0.062 ± 0.028	0.053 ± 0.03
pBV/BV	0.792 ± 0.055*#	0.722 ± 0.119*	0.531 ± 0.196	0.744 ± 0.101*	0.759 ± 0.149*	0.58 ± 0.128
rBV/BV	0.208 ± 0.055*#	0.278 ± 0.119*	0.469 ± 0.196	0.256 ± 0.101*	0.241 ± 0.149*	0.42 ± 0.128
pTb.N (1/mm)	3.656 ± 0.396*#	3.391 ± 0.392*	2.982 ± 0.698	2.791 ± 0.342	2.868 ± 0.354	2.844 ± 0.434
rTb.N (1/mm)	3.183 ± 0.433*	3.201 ± 0.408*	3.545 ± 0.568	2.514 ± 0.397*	2.558 ± 0.457*	3.249 ± 0.449
pTb.Th (mm)	0.114 ± 0.011*#	0.106 ± 0.012*	0.091 ± 0.014	0.109 ± 0.012	0.104 ± 0.012	0.097 ± 0.009
rTb.Th (mm)	0.083 ± 0.004*	0.082 ± 0.004*	0.074 ± 0.007	0.09 ± 0.006*#	0.084 ± 0.007*	0.077 ± 0.005
pTb.S (mm^2)	0.043 ± 0.009*	0.039 ± 0.008*	0.03 ± 0.007	0.047 ± 0.01*	0.045 ± 0.009*	0.033 ± 0.006
rTb.l (mm)	0.298 ± 0.012*#	0.289 ± 0.012*	0.283 ± 0.009	0.309 ± 0.015*#	0.295 ± 0.013*	0.283 ± 0.008
R-R Junc.D ($1/mm^3$)	11.197 ± 5.487*	14.306 ± 7.943*	31.631 ± 21.288	6.803 ± 5.167*	8.008 ± 7.372*	21.346 ± 10.996
R-P Junc.D ($1/mm^3$)	62.79 ± 25.867	54.406 ± 16.969	69.067 ± 41.58	25.793 ± 12.31*	27.742 ± 11.829*	47.272 ± 22.711
P-P Junc.D ($1/mm^3$)	55.371 ± 21.678	45.763 ± 13.219	49.419 ± 32.087	21.864 ± 10.345*	24.624 ± 9.229*	34.566 ± 16.623

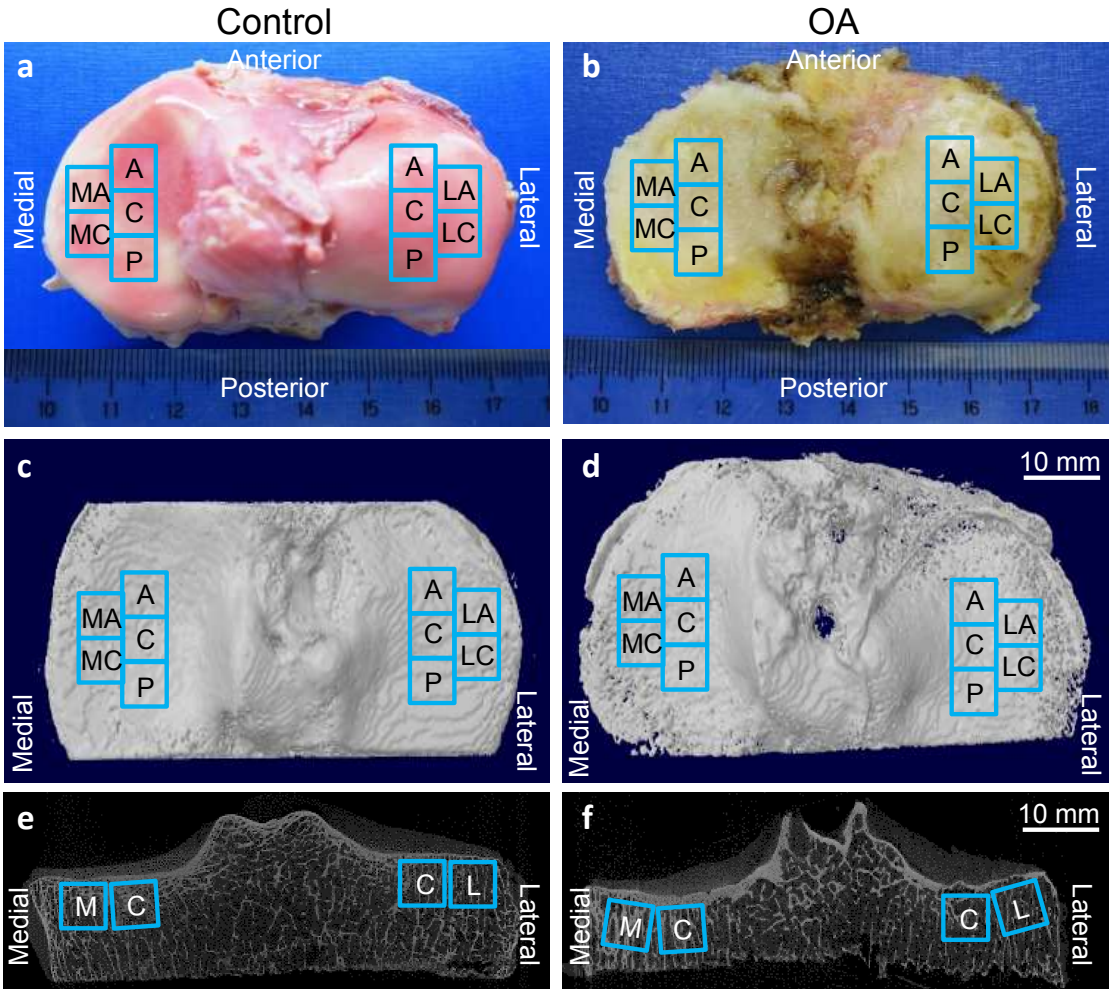

Figure 6.1 Illustration of sub-region selections. a, b) Top-down view of a tibial plateau from control and OA; c, d) Top-down view from reconstructed µCT images of control and OA; e, f) µCT images of the anterior-posterior view. A: anterior; P: posterior; C: central; MA: medial anterior; MC: medial central; LA: lateral anterior; LC: lateral central

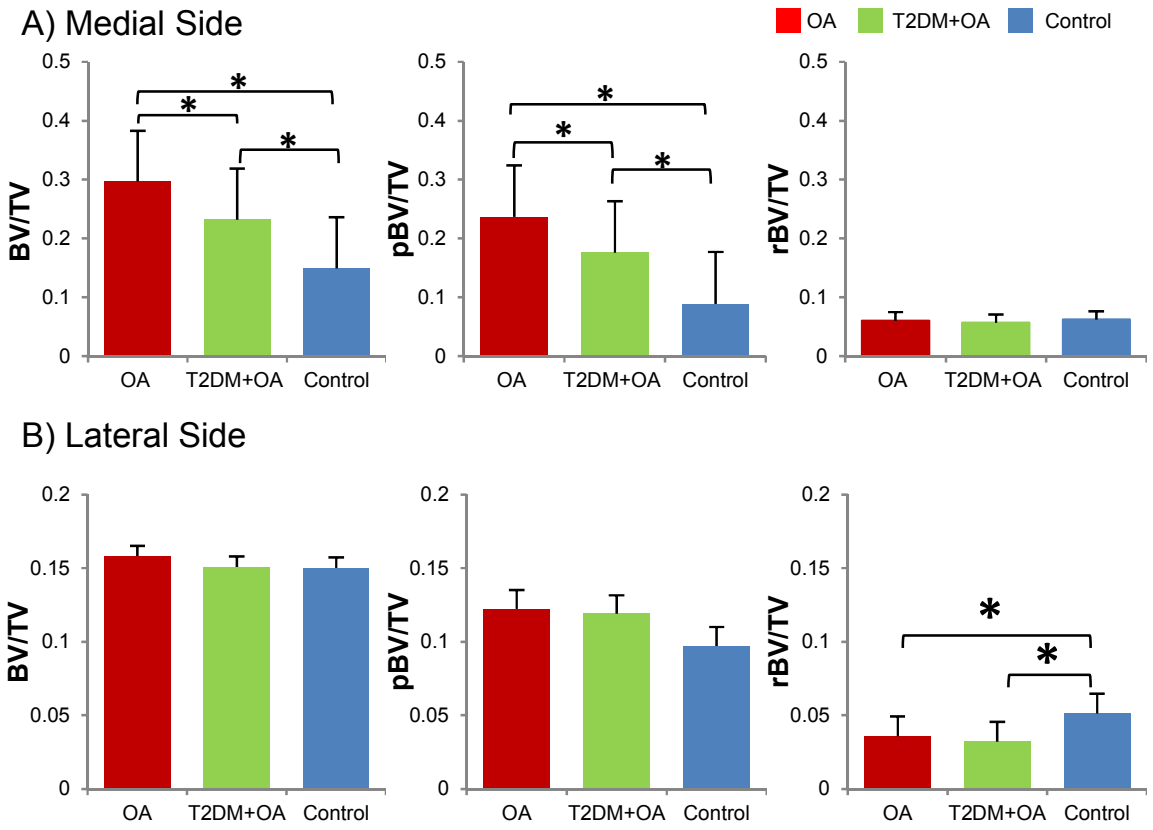

Figure 6.2 Microstructural comparisons between OA, T2DM/OA, and control on A) medial side and B) lateral side.

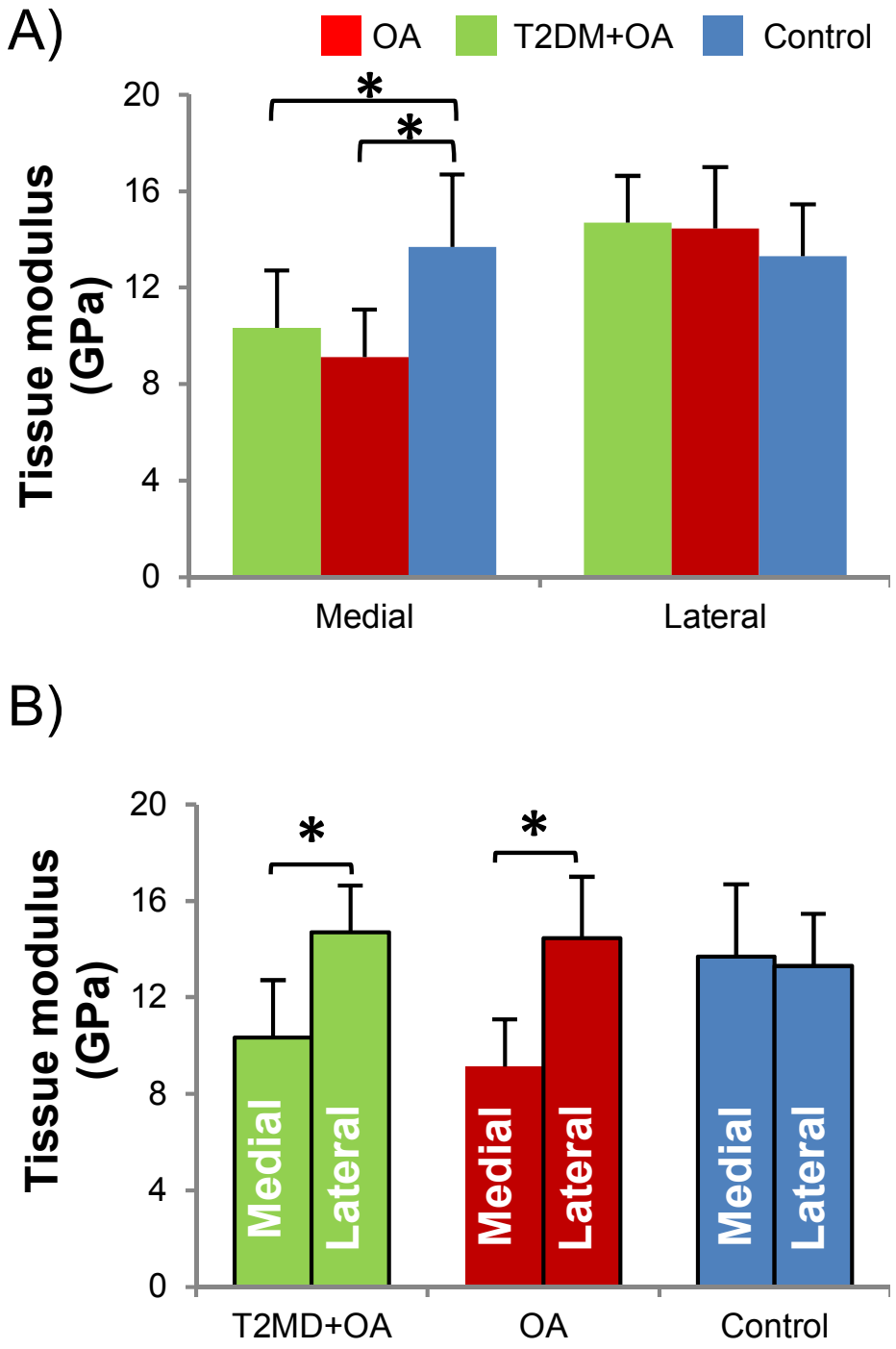

Figure 6.3 Tissue modulus comparisons between A) medial and lateral side, and B) T2DM/OA, regular OA, and control.

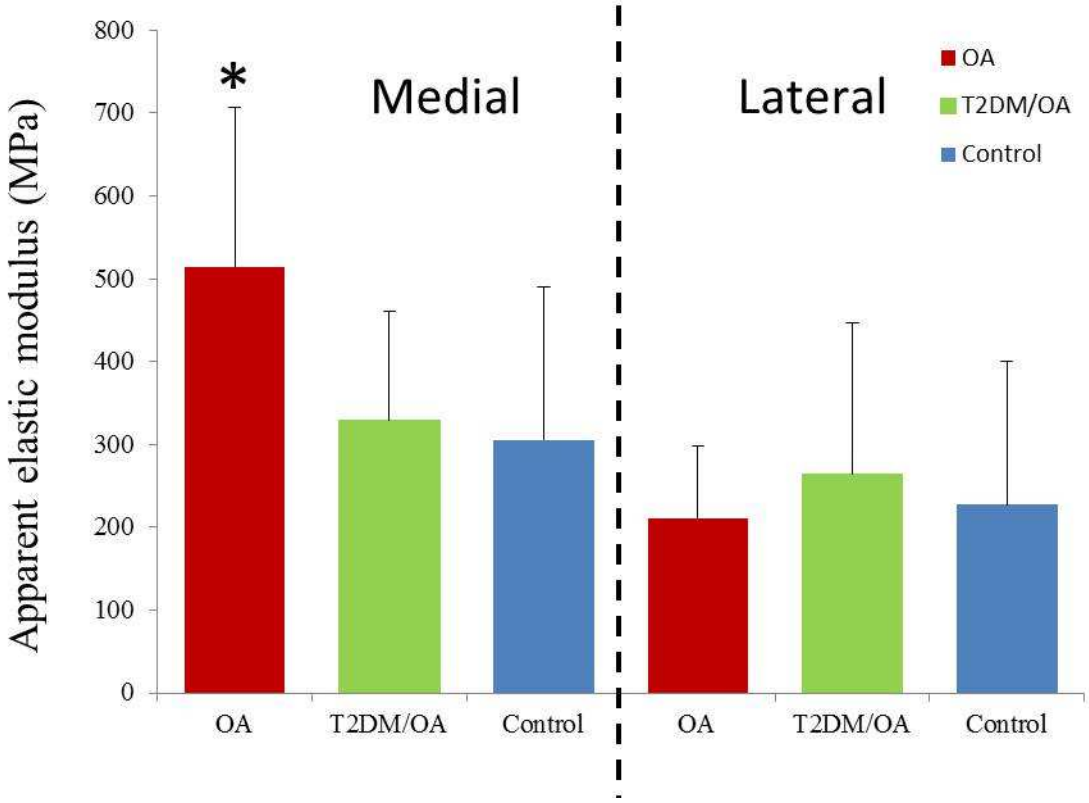

Figure 6.4 Apparent elastic modulus predicted by FE analysis.* indicate significance from the other groups. *p<0.05

Chapter 7. Summary and future work

This thesis is focused on evaluating the contribution of trabecular bone tissue-level anisotropy and heterogeneity to apparent-level bone stiffness and included: 1) an assessment of the anisotropy and heterogeneity of individual trabecular plates and rods; 2) the development of a voxel-based μFE model with an experimentally obtained anisotropic TMD-to-modulus relationship; and 3) an evaluation of the influence of bone diseases on bone quality and bone stiffness. These studies will fundamentally formulate a novel approach to quantitatively assess bone strength that accounts for the trabecular anisotropic and heterogeneous material properties of healthy and diseased human bone. This thesis comprehensively investigated the contribution of trabecular anisotropy and heterogeneity to bone mechanical competence, which may improve the understanding of current clinical fracture risk assessment. Furthermore, the study of mineral composition and tissue modulus correlation on the valuable AIS and OA biopsy and specimens gave insights into whether the altered tissue affects the apparent bone strength and stiffness of patients and the factors that possibly contribute to the altered apparent level mechanics. From a basic science perspective, the thesis also provides direct evidence into how several hierarchical levels are mechanically connected. Further, the anisotropy of trabecular bone was evaluated for the first time on different trabecular types and in different anatomic directions, which will provide insights into the underlying mineral and collagen ultrastructure and lamellar layouts of trabecular bone.

Extensive efforts have been dedicated to study the tissue material properties, including the collagen matrix and the mineral content, and it has been widely believed that tissue material

properties are fundamental determinants of bone strength. However, the studies in this thesis systematically and experimentally validated and confirmed that tissue material properties actually have very limited contributions to whole bone-level mechanical behaviors. These discoveries are of considerable importance, as they solve the last piece of the puzzle in our understanding of bone strength and highlight that future research directions should not focus on variances within tissue material properties. On the other hand, in certain bone diseases, the overall altered material properties collectively might affect the apparent bone strength and stiffness.

7.1. Anisotropic trabecular plates and rods

With the capabilities of ITS, the complicated trabecular bone structure could be segmented into individual structural elements, which allowed us to systematically study the tissue-level mechanical properties of trabecular plates and rods in this work. Not only did we find that the tissue modulus differences between plates and rods were attributed to the different levels of mineralization, but we also confirmed, for the first time, that trabecular plates and rods possess the same anisotropic Young's modulus. On the tissue level, strong but different correlations were discovered between TMD and Young's modulus in axial and lateral cross-sections of trabecular bone regardless of the trabecular type and anatomic direction. These results suggest that the underlying ultrastructure between trabecular plates and rods are similar, and the anisotropy is most likely attributed to the highly organized alignments of trabecular ultrastructure. Also, the spatially heterogeneous mineralization determines the local tissue modulus, which is consistent with our current understanding. These findings were demonstrated similarly in major loading sites such as femur and tibia. It would also be interesting to see if the discoveries of this

study translate to major trabecular loading sites like the spine and non-loading sites like the radius.

7.2. Contribution of anisotropic trabecular plate and rod to apparent level mechanical properties

Once the anisotropic and heterogeneous tissue level trabecular mechanical properties were established, they were incorporated into our voxel-based FE models to evaluate their contribution to apparent level stiffness and strength. Without any surprise, such incorporation didn't improve the prediction power of current μFE based bone strength assessment. However, without any scaling in the modulus, the anisotropic model prediction of stiffness and strength is indistinguishable with the gold standard mechanical testing measurements, suggesting that the anisotropy of trabecular bone is an important apparent stiffness and strength determinant. Nonetheless, the anisotropic model prediction was not different from the specimen-specific homogeneous model, suggesting that the tissue level modulus contributes to the apparent level in a more collective manner and the microscopic variances only play a minor role. However, the anisotropy and heterogeneity might make a difference in bone diseases affecting bone mineralization and the trabecular orientation distributions.

7.3. Diseases altered tissue material properties and apparent level mechanical properties

OA knee subchondral bone and AIS pelvic trabecular bone were selected to study disease-altered tissue material properties and the associated apparent level mechanical properties. Dramatic changes in trabecular microstructure suggest the occurrence of a high level of

remodeling, which makes the subchondral bone in OA an ideal candidate for studying changes in tissue material properties. A decrease in tissue modulus was discovered in the region under severely damaged cartilage, which provides explanations for a limited increase in apparent stiffness with almost doubled bone volume fraction, as described in Chapter 5. The tissue material properties of AIS bone had never been studied prior to this thesis work. Although no differences were found between AIS and control bone tissue, the tissue modulus of the growing adolescent bone was ~70% lower with a ~30% decrease of TMD compared to the matured bone described in Chapter 3, suggesting a distinct role of the mineral density in determining tissue modulus.

7.4. Future work

The discoveries in this thesis prompt several new questions that can be explored in future studies. First, it would be interesting to study the tissue material properties of trabecular bone in non-loading sites such as radius and trabecular bone-dominated sites like spine, as the directional based anisotropy might be a result of bone adaptation to loading. Whether similar anisotropy can be found at these alternative sites would serve as major evidence of how adaptation sculptures the bone structure at the ultrastructural level. Second, the anisotropic tissue modulus can be incorporated into our already established heterogeneous plate- and rod-based FE models to increase the precision of this fast and computation time-saving model for the clinical assessment of bone strength. Third, the anisotropic model might be applied to a highly direction-based loading condition, such as the side loading on the femoral neck, which mimics a side fall that causes a common type of fracture. The anisotropic tissue modulus might be amplified by microstructure weaknesses and suggest an important difference, as the anatomic directions in

which most trabecular bone has its lateral cross-section faces to and has lower lateral modulus could be in the same directions that have fewer trabecular bone aligned, and vice versa. Similar suggestions might apply to the subchondral bone under the severely damaged cartilage in OA, as ITS analysis indicates the vast majority of trabecular plates aligning in the longitudinal loading directions that might further amplify the higher trabecular modulus in that direction, which might help understand the local mechanical loading environment that could have an implication in OA pathogenesis and progression.

Bibliography

Center for Disease Control and Prevention. National diabetes statistics report: Estimates of diabetes and its burden in the United States, 2014. US Department of Health and Human Services.

Agarwal, S., F. Rosete, C. Zhang, D. J. McMahon, X. E. Guo, E. Shane and K. K. Nishiyama (2016). "In vivo assessment of bone structure and estimated bone strength by first- and second-generation HR-pQCT." Osteoporos Int.

Bacchetta, J., S. Boutroy, N. Vilayphiou, B. Ranchin, A. Fouque-Aubert, O. Basmaison and P. Cochat (2011). "Bone assessment in children with chronic kidney disease: data from two new bone imaging techniques in a single-center pilot study." Pediatr Nephrol **26**(4): 587-595.

Basel, D. and R. D. Steiner (2009). "Osteogenesis imperfecta: recent findings shed new light on this once well-understood condition." Genet Med **11**(6): 375-385.

Bayraktar, H. H., E. F. Morgan, G. L. Niebur, G. E. Morris, E. K. Wong and T. M. Keaveny (2004). "Comparison of the elastic and yield properties of human femoral trabecular and cortical bone tissue." J Biomech **37**(1): 27-35.

Beer, F. P. (2006). Mechanics of materials. E. R. Johnston and J. T. DeWolf. Boston :, McGraw-Hill Higher Education.

Bevill, G., S. K. Eswaran, A. Gupta, P. Papadopoulos and T. M. Keaveny (2006). "Influence of bone volume fraction and architecture on computed large-deformation failure mechanisms in human trabecular bone." Bone **39**(6): 1218-1225.

Bilezikian, J. P. (1999). "Osteoporosis in men." J Clin Endocrinol Metab **84**(10): 3431-3434.

Birkenhager-Frenkel, D. H., A. L. Nigg, C. J. Hens and J. C. Birkenhager (1993). "Changes of interstitial bone thickness with age in men and women." Bone **14**(3): 211-216.

Boivin, G. and P. J. Meunier (2002). "Changes in bone remodeling rate influence the degree of mineralization of bone." Connect Tissue Res **43**(2-3): 535-537.

Bourne, B. C. and M. C. van der Meulen (2004). "Finite element models predict cancellous apparent modulus when tissue modulus is scaled from specimen CT-attenuation." J Biomech **37**(5): 613-621.

Boutroy, S., B. Van Rietbergen, E. Sornay-Rendu, F. Munoz, M. L. Bouxsein and P. D. Delmas (2008). "Finite element analysis based on in vivo HR-pQCT images of the distal radius is associated with wrist fracture in postmenopausal women." J Bone Miner Res **23**(3): 392-399.

Bouxsein, M. L., S. K. Boyd, B. A. Christiansen, R. E. Guldberg, K. J. Jepsen and R. Muller (2010). "Guidelines for assessment of bone microstructure in rodents using micro-computed tomography." J Bone Miner Res **25**(7): 1468-1486.

Bouxsein, M. L., B. S. Coan and S. C. Lee (1999). "Prediction of the strength of the elderly proximal femur by bone mineral density and quantitative ultrasound measurements of the heel and tibia." Bone **25**(1): 49-54.

Boyde, A., J. C. Elliott and S. J. Jones (1993). "Stereology and histogram analysis of backscattered electron images: age changes in bone." Bone **14**(3): 205-210.

Bronner, F. and R. V. Worrell (1999). "Orthopaedics: Principles of basic and clinical science." Informa HealthCare.

Burghardt, A. J., G. J. Kazakia, A. Laib and S. Majumdar (2008). "Quantitative assessment of bone tissue mineralization with polychromatic micro-computed tomography." Calcif Tissue Int **83**(2): 129-138.

Camacho, N. P., S. Rinnerthaler, E. P. Paschalis, R. Mendelsohn, A. L. Boskey and P. Fratzl (1999). "Complementary information on bone ultrastructure from scanning small angle X-ray scattering and Fourier-transform infrared microspectroscopy." Bone **25**(3): 287-293.

Carnelli, D., P. Vena, M. Dao, C. Ortiz and R. Contro (2013). "Orientation and size-dependent mechanical modulation within individual secondary osteons in cortical bone tissue." J R Soc Interface **10**(81): 20120953.

Chen, Y. Z., B; Wang J; Zhao, W; Wang, T; Leung F; Lu, W; Guo, XE (2016). "Changes in subchondral trabecular plate and rod microstructure and articular cartilage in human osteoarthritic knees." ASBMR Podium and poster presentation

Cheng, J. C. and X. Guo (1997). "Osteopenia in adolescent idiopathic scoliosis. A primary problem or secondary to the spinal deformity?" Spine **22**(15): 1716-1721.

Cheng, J. C., X. Guo and A. H. Sher (1999). "Persistent osteopenia in adolescent idiopathic scoliosis. A longitudinal follow up study." Spine **24**(12): 1218-1222.

Cheuk KY, W. J., Yu WP, Lee W, Lam T, Guo XE, Cheng JC (2016). Abnormal trabecular plate and rod structure in adolescent idiopathic scoliosis- a study with individual trabecula segmentation (ITS). ORS. Orlando, FL, USA.

Cheuk, K. Y., T. Y. Zhu, F. W. Yu, V. W. Hung, K. M. Lee, L. Qin, J. C. Cheng and T. P. Lam (2015). "Abnormal Bone Mechanical and Structural Properties in Adolescent Idiopathic

Scoliosis: A Study with Finite Element Analysis and Structural Model Index." Calcif Tissue Int **97**(4): 343-352.

Chevalier, Y., D. Pahr, H. Allmer, M. Charlebois and P. Zysset (2007). "Validation of a voxel-based FE method for prediction of the uniaxial apparent modulus of human trabecular bone using macroscopic mechanical tests and nanoindentation." J Biomech **40**(15): 3333-3340.

Chiang, C. Y., R. M. Zebaze, A. Ghasem-Zadeh, S. Iuliano-Burns, A. Hardidge and E. Seeman (2013). "Teriparatide improves bone quality and healing of atypical femoral fractures associated with bisphosphonate therapy." Bone **52**(1): 360-365.

Christen, D., L. J. Melton, 3rd, A. Zwahlen, S. Amin, S. Khosla and R. Muller (2013). "Improved fracture risk assessment based on nonlinear micro-finite element simulations from HRpQCT images at the distal radius." J Bone Miner Res **28**(12): 2601-2608.

Cowin, S. C. (2001). "Bone mechanics handbook CRC press." Bone mechanics handbook(2nd ed.) Boca Raton: USA: CRC Press.

Dall'Ara, E., C. Karl, G. Mazza, G. Franzoso, P. Vena, M. Pretterklieber, D. Pahr and P. Zysset (2013). "Tissue properties of the human vertebral body sub-structures evaluated by means of microindentation." J Mech Behav Biomed Mater **25**: 23-32.

Dall'Ara, E., C. Ohman, M. Baleani and M. Viceconti (2011). "Reduced tissue hardness of trabecular bone is associated with severe osteoarthritis." J Biomech **44**(8): 1593-1598.

Dall'Ara, E., R. Schmidt and P. Zysset (2012). "Microindentation can discriminate between damaged and intact human bone tissue." Bone **50**(4): 925-929.

Ding, M. and I. Hvid (2000). "Quantification of age-related changes in the structure model type and trabecular thickness of human tibial cancellous bone." Bone **26**(3): 291-295.

Dong, X. N. and X. E. Guo (2004). "The dependence of transversely isotropic elasticity of human femoral cortical bone on porosity." J Biomech **37**(8): 1281-1287.

Donnelly, E., A. L. Boskey, S. P. Baker and M. C. van der Meulen (2010). "Effects of tissue age on bone tissue material composition and nanomechanical properties in the rat cortex." J Biomed Mater Res A **92**(3): 1048-1056.

Dowsett, D. J. (2006). The physics of diagnostic imaging. P. A. Kenny and R. E. Johnston. London :, Hodder Arnold ;.

Duan, Y., T. J. Beck, X. F. Wang and E. Seeman (2003). "Structural and biomechanical basis of sexual dimorphism in femoral neck fragility has its origins in growth and aging." J Bone Miner Res **18**(10): 1766-1774.

Einhorn, T. A. (1992). "Bone strength: the bottom line." Calcif Tissue Int **51**(5): 333-339.

Ettinger, B., D. B. Burr and R. O. Ritchie (2013). "Proposed pathogenesis for atypical femoral fractures: lessons from materials research." Bone **55**(2): 495-500.

Faingold, A., S. R. Cohen, N. Reznikov and H. D. Wagner (2013). "Osteonal lamellae elementary units: lamellar microstructure, curvature and mechanical properties." Acta Biomater **9**(4): 5956-5962.

Faingold, A., S. R. Cohen and H. D. Wagner (2012). "Nanoindentation of osteonal bone lamellae." J Mech Behav Biomed Mater **9**: 198-206.

Fonseca, H., D. Moreira-Goncalves, H. J. Coriolano and J. A. Duarte (2014). "Bone quality: the determinants of bone strength and fragility." Sports Med **44**(1): 37-53.

Fraser, W. D. (2009). "Hyperparathyroidism." Lancet **374**(9684): 145-158.

Garcia-Martin, A., P. Rozas-Moreno, R. Reyes-Garcia, S. Morales-Santana, B. Garcia-Fontana, J. A. Garcia-Salcedo and M. Munoz-Torres (2012). "Circulating levels of sclerostin are increased in patients with type 2 diabetes mellitus." J Clin Endocrinol Metab **97**(1): 234-241.

Gennari, L., D. Merlotti, R. Valenti, E. Ceccarelli, M. Ruvio, M. G. Pietrini, C. Capodarca, M. B. Franci, M. S. Campagna, A. Calabro, D. Cataldo, K. Stolakis, F. Dotta and R. Nuti (2012). "Circulating sclerostin levels and bone turnover in type 1 and type 2 diabetes." J Clin Endocrinol Metab **97**(5): 1737-1744.

Georgiadis, M., M. Guizar-Sicairos, A. Zwahlen, A. J. Trussel, O. Bunk, R. Muller and P. Schneider (2015). "3D scanning SAXS: a novel method for the assessment of bone ultrastructure orientation." Bone **71**: 42-52.

Goldring, M. B. and S. R. Goldring (2010). "Articular cartilage and subchondral bone in the pathogenesis of osteoarthritis." Ann N Y Acad Sci **1192**: 230-237.

Gourion-Arsiquaud, S., D. Faibish, E. Myers, L. Spevak, J. Compston, A. Hodsman, E. Shane, R. R. Recker, E. R. Boskey and A. L. Boskey (2009). "Use of FTIR spectroscopic imaging to identify parameters associated with fragility fracture." J Bone Miner Res **24**(9): 1565-1571.

Gourlay, M. L. and S. A. Brown (2004). "Clinical considerations in premenopausal osteoporosis." Arch Intern Med **164**(6): 603-614.

Gross, T., D. H. Pahr, F. Peyrin and P. K. Zysset (2012). "Mineral heterogeneity has a minor influence on the apparent elastic properties of human cancellous bone: a SRmuCT-based finite element study." Comput Methods Biomech Biomed Engin **15**(11): 1137-1144.

Grynpas, M. (1993). "Age and disease-related changes in the mineral of bone." Calcif Tissue Int **53 Suppl 1**: S57-64.

Harrison, N. M., P. F. McDonnell, D. C. O'Mahoney, O. D. Kennedy, F. J. O'Brien and P. E. McHugh (2008). "Heterogeneous linear elastic trabecular bone modelling using micro-CT attenuation data and experimentally measured heterogeneous tissue properties." J Biomech **41**(11): 2589-2596.

Hengsberger, S., A. Kulik and P. Zysset (2002). "Nanoindentation discriminates the elastic properties of individual human bone lamellae under dry and physiological conditions." Bone **30**(1): 178-184.

Hoffler, C. E., X. E. Guo, P. K. Zysset and S. A. Goldstein (2005). "An application of nanoindentation technique to measure bone tissue Lamellae properties." J Biomech Eng **127**(7): 1046-1053.

Hoffler, C. E., K. E. Moore, K. Kozloff, P. K. Zysset, M. B. Brown and S. A. Goldstein (2000). "Heterogeneity of bone lamellar-level elastic moduli." Bone **26**(6): 603-609.

Hoffler, C. E., K. E. Moore, K. Kozloff, P. K. Zysset and S. A. Goldstein (2000). "Age, gender, and bone lamellae elastic moduli." J Orthop Res **18**(3): 432-437.

Hollister, S. J., J. M. Brennan and N. Kikuchi (1994). "A homogenization sampling procedure for calculating trabecular bone effective stiffness and tissue level stress." J Biomech **27**(4): 433-444.

Hung, V. W., L. Qin, C. S. Cheung, T. P. Lam, B. K. Ng, Y. K. Tse, X. Guo, K. M. Lee and J. C. Cheng (2005). "Osteopenia: a new prognostic factor of curve progression in adolescent idiopathic scoliosis." J Bone Joint Surg Am **87**(12): 2709-2716.

Iwata, K., T. Mashiba, T. Hitora, Y. Yamagami and T. Yamamoto (2014). "A large amount of microdamages in the cortical bone around fracture site in a patient of atypical femoral fracture after long-term bisphosphonate therapy." Bone **64**: 183-186.

Jaasma, M. J., H. H. Bayraktar, G. L. Niebur and T. M. Keaveny (2002). "Biomechanical effects of intraspecimen variations in tissue modulus for trabecular bone." J Biomech **35**(2): 237-246.

Jarvinen, T. L. (2003). "Novel paradigm on the effect of estrogen on bone." J Musculoskelet Neuronal Interact **3**(4): 374-380; discussion 381.

Kabel, J., B. van Rietbergen, M. Dalstra, A. Odgaard and R. Huiskes (1999). "The role of an effective isotropic tissue modulus in the elastic properties of cancellous bone." J Biomech **32**(7): 673-680.

Keaveny, T. M. and M. L. Bouxsein (2008). "Theoretical implications of the biomechanical fracture threshold." J Bone Miner Res **23**(10): 1541-1547.

Keaveny, T. M., X. E. Guo, E. F. Wachtel, T. A. McMahon and W. C. Hayes (1994). "Trabecular bone exhibits fully linear elastic behavior and yields at low strains." J Biomech **27**(9): 1127-1136.

King, K. B. and A. K. Rosenthal (2015). "The adverse effects of diabetes on osteoarthritis: update on clinical evidence and molecular mechanisms." Osteoarthritis Cartilage **23**(6): 841-850.

Kontulainen, S. A., H. M. Macdonald and H. A. McKay (2006). "Change in cortical bone density and its distribution differs between boys and girls during puberty." J Clin Endocrinol Metab **91**(7): 2555-2561.

Korsa, R., J. Lukes, J. Sepitka and T. Mares (2015). "Elastic Properties of Human Osteon and Osteonal Lamella Computed by a Bidirectional Micromechanical Model and Validated by Nanoindentation." J Biomech Eng **137**(8): 081002.

Laiguillon, M. C., A. Courties, X. Houard, M. Auclair, A. Sautet, J. Capeau, B. Feve, F. Berenbaum and J. Sellam (2015). "Characterization of diabetic osteoarthritic cartilage and role of high glucose environment on chondrocyte activation: toward pathophysiological delineation of diabetes mellitus-related osteoarthritis." Osteoarthritis Cartilage **23**(9): 1513-1522.

Lawrence, R. C., D. T. Felson, C. G. Helmick, L. M. Arnold, H. Choi, R. A. Deyo, S. Gabriel, R. Hirsch, M. C. Hochberg, G. G. Hunder, J. M. Jordan, J. N. Katz, H. M. Kremers, F. Wolfe and W. National Arthritis Data (2008). "Estimates of the prevalence of arthritis and other rheumatic conditions in the United States. Part II." Arthritis Rheum **58**(1): 26-35.

Li, B. and R. M. Aspden (1997). "Composition and mechanical properties of cancellous bone from the femoral head of patients with osteoporosis or osteoarthritis." J Bone Miner Res **12**(4): 641-651.

Linde, F., P. Norgaard, I. Hvid, A. Odgaard and K. Soballe (1991). "Mechanical properties of trabecular bone. Dependency on strain rate." J Biomech **24**(9): 803-809.

Liu, X. S., A. Cohen, E. Shane, E. Stein, H. Rogers, S. L. Kokolus, P. T. Yin, D. J. McMahon, J. M. Lappe, R. R. Recker and X. E. Guo (2010). "Individual trabeculae segmentation (ITS)-based morphological analysis of high-resolution peripheral quantitative computed tomography images detects abnormal trabecular plate and rod microarchitecture in premenopausal women with idiopathic osteoporosis." J Bone Miner Res **25**(7): 1496-1505.

Liu, X. S., P. Sajda, P. K. Saha, F. W. Wehrli, G. Bevill, T. M. Keaveny and X. E. Guo (2008). "Complete volumetric decomposition of individual trabecular plates and rods and its morphological correlations with anisotropic elastic moduli in human trabecular bone." J Bone Miner Res **23**(2): 223-235.

Liu, X. S., P. Sajda, P. K. Saha, F. W. Wehrli and X. E. Guo (2006). "Quantification of the roles of trabecular microarchitecture and trabecular type in determining the elastic modulus of human trabecular bone." J Bone Miner Res **21**(10): 1608-1617.

Liu, X. S., E. M. Stein, B. Zhou, C. A. Zhang, T. L. Nickolas, A. Cohen, V. Thomas, D. J. McMahon, F. Cosman, J. Nieves, E. Shane and X. E. Guo (2011). "Individual trabecula segmentation (ITS)-based morphological analyses and micro finite element analysis of HR-pQCT images discriminate postmenopausal fragility fractures independent of DXA measurements." J Bone Miner Res.

Liu, X. S., M. D. Walker, D. J. McMahon, J. Udesky, G. Liu, J. P. Bilezikian and X. E. Guo (2011). "Better skeletal microstructure confers greater mechanical advantages in Chinese-American women versus white women." J Bone Miner Res **26**(8): 1783-1792.

Liu, X. S., J. Wang, B. Zhou, E. Stein, X. Shi, M. Adams, E. Shane and X. E. Guo (2013). "Fast Trabecular Bone Strength Predictions of HR-pQCT and Individual Trabeculae Segmentation–Based Plate and Rod Finite Element Model Discriminate Postmenopausal Vertebral Fractures." Journal of Bone and Mineral Research **28**(7): 1666-1678.

Liu, X. S., X. H. Zhang and X. E. Guo (2009). "Contributions of trabecular rods of various orientations in determining the elastic properties of human vertebral trabecular bone." Bone **45**(2): 158-163.

Liu, X. S., X. H. Zhang, K. K. Sekhon, M. F. Adams, D. J. McMahon, J. P. Bilezikian, E. Shane and X. E. Guo (2010). "High-resolution peripheral quantitative computed tomography can assess microstructural and mechanical properties of human distal tibial bone." J Bone Miner Res **25**(4): 746-756.

Mackie, E. J., Y. A. Ahmed, L. Tatarczuch, K. S. Chen and M. Mirams (2008). "Endochondral ossification: how cartilage is converted into bone in the developing skeleton." Int J Biochem Cell Biol **40**(1): 46-62.

Macneil, J. A. and S. K. Boyd (2008). "Bone strength at the distal radius can be estimated from high-resolution peripheral quantitative computed tomography and the finite element method." Bone **42**(6): 1203-1213.

Magnusson, K., K. B. Hagen, N. Osteras, L. Nordsletten, B. Natvig and I. K. Haugen (2015). "Diabetes is associated with increased hand pain in erosive hand osteoarthritis: data from a population-based study." Arthritis Care Res **67**(2): 187-195.

Melton, L. J., 3rd, E. A. Chrischilles, C. Cooper, A. W. Lane and B. L. Riggs (1992). "Perspective. How many women have osteoporosis?" J Bone Miner Res **7**(9): 1005-1010.

Milovanovic, P., Z. Rakocevic, D. Djonic, V. Zivkovic, M. Hahn, S. Nikolic, M. Amling, B. Busse and M. Djuric (2014). "Nano-structural, compositional and micro-architectural signs of cortical bone fragility at the superolateral femoral neck in elderly hip fracture patients vs. healthy aged controls." Exp Gerontol **55**: 19-28.

Morgan, E. F. and T. M. Keaveny (2001). "Dependence of yield strain of human trabecular bone on anatomic site." J Biomech **34**(5): 569-577.

Nawathe, S., H. Akhlaghpour, M. L. Bouxsein and T. M. Keaveny (2014). "Microstructural failure mechanisms in the human proximal femur for sideways fall loading." J Bone Miner Res **29**(2): 507-515.

Nawathe, S., B. P. Nguyen, N. Barzanian, H. Akhlaghpour, M. L. Bouxsein and T. M. Keaveny (2015). "Cortical and trabecular load sharing in the human femoral neck." J Biomech **48**(5): 816-822.

Niebur, G. L., J. C. Yuen, A. J. Burghardt and T. M. Keaveny (2001). "Sensitivity of damage predictions to tissue level yield properties and apparent loading conditions." J Biomech **34**(5): 699-706.

Nishiyama, K. K., A. Cohen, P. Young, J. Wang, J. M. Lappe, X. E. Guo, D. W. Dempster, R. R. Recker and E. Shane (2014). "Teriparatide increases strength of the peripheral skeleton in premenopausal women with idiopathic osteoporosis: a pilot HR-pQCT study." J Clin Endocrinol Metab **99**(7): 2418-2425.

Oliver, W. C. and G. M. Pharr (1992). "An improved technique for determining hardness and elastic modulus using load and displacement sensing indentation experiments." Journal of Materials Research **7**(06): 1564-1583.

Pan, X., E. Y. Sidky and M. Vannier (2009). "Why do commercial CT scanners still employ traditional, filtered back-projection for image reconstruction?" Inverse Probl **25**(12): 1230009.

Papadopoulos, P. and J. Lu (2001). "On the formulation and numerical solution of problems in anisotropic finite plasticity." Computer Methods in Applied Mechanics and Engineering **190**(37–38): 4889-4910.

Parfitt, A. M. (2002). "Targeted and nontargeted bone remodeling: relationship to basic multicellular unit origination and progression." Bone **30**(1): 5-7.

Rahman, M. M., J. Cibere, A. H. Anis, C. H. Goldsmith and J. A. Kopec (2014). "Risk of Type 2 Diabetes among Osteoarthritis Patients in a Prospective Longitudinal Study." Int J Rheumatol **2014**: 620920.

Ralston, S. H., A. L. Langston and I. R. Reid (2008). "Pathogenesis and management of Paget's disease of bone." Lancet **372**(9633): 155-163.

Rauch, F., R. Travers, A. M. Parfitt and F. H. Glorieux (2000). "Static and dynamic bone histomorphometry in children with osteogenesis imperfecta." Bone **26**(6): 581-589.

Reisinger, A. G., D. H. Pahr and P. K. Zysset (2011). "Principal stiffness orientation and degree of anisotropy of human osteons based on nanoindentation in three distinct planes." J Mech Behav Biomed Mater **4**(8): 2113-2127.

Reznikov, N., H. Chase, V. Brumfeld, R. Shahar and S. Weiner (2015). "The 3D structure of the collagen fibril network in human trabecular bone: relation to trabecular organization." Bone **71**: 189-195.

Rho, J. Y., T. Y. Tsui and G. M. Pharr (1997). "Elastic properties of human cortical and trabecular lamellar bone measured by nanoindentation." Biomaterials **18**(20): 1325-1330.

Roschger, P., P. Fratzl, K. Klaushofer and G. Rodan (1997). "Mineralization of cancellous bone after alendronate and sodium fluoride treatment: a quantitative backscattered electron imaging study on minipig ribs." Bone **20**(5): 393-397.

Roschger, P., H. S. Gupta, A. Berzlanovich, G. Ittner, D. W. Dempster, P. Fratzl, F. Cosman, M. Parisien, R. Lindsay, J. W. Nieves and K. Klaushofer (2003). "Constant mineralization density distribution in cancellous human bone." Bone **32**(3): 316-323.

Roschger, P., E. P. Paschalis, P. Fratzl and K. Klaushofer (2008). "Bone mineralization density distribution in health and disease." Bone **42**(3): 456-466.

Ryan, J. W., P. H. Anderson, A. G. Turner and H. A. Morris (2013). "Vitamin D activities and metabolic bone disease." Clin Chim Acta **425**: 148-152.

Saha, P. K. and B. B. Chaudhuri (1996). "3D digital topology under binary transformation with applications." Computer Vision and Image Understanding **63**(3): 418-429.

Saha, P. K., B. B. Chaudhuri, B. Chanda and D. Dutta Majumder (1994). "Topology preservation in 3D digital space." Pattern Recognition **27**(2): 295-300.

Saha, P. K., B. B. Chaudhuri, D. Dutta and D. D. Majumder (1997). "A new shape preserving parallel thinning algorithm for 3D digital images." Pattern Recognition **30**(12): 1939-1955.

Schett, G., A. Kleyer, C. Perricone, E. Sahinbegovic, A. Iagnocco, J. Zwerina, R. Lorenzini, F. Aschenbrenner, F. Berenbaum, M. A. D'Agostino, J. Willeit and S. Kiechl (2013). "Diabetes is an independent predictor for severe osteoarthritis: results from a longitudinal cohort study." Diabetes Care **36**(2): 403-409.

Shi, X., X. S. Liu, X. Wang, X. E. Guo and G. L. Niebur (2010). "Type and orientation of yielded trabeculae during overloading of trabecular bone along orthogonal directions." J Biomech **43**(13): 2460-2466.

Sneddon, I. (1965). "The relation between load and penetration in the axisymmetric Boussinesq problem for a punch of arbitrary profile." Int J Engng Sci **3**: 47-57.

Sneddon, I. N. (2008). "Boussinesq's problem for a flat-ended cylinder." Mathematical Proceedings of the Cambridge Philosophical Society **42**(1): 29-39.

Stein, E. M., A. Kepley, M. Walker, T. L. Nickolas, K. Nishiyama, B. Zhou, X. S. Liu, D. J. McMahon, C. Zhang, S. Boutroy, F. Cosman, J. Nieves, X. E. Guo and E. Shane (2014). "Skeletal structure in postmenopausal women with osteopenia and fractures is characterized by abnormal trabecular plates and cortical thinning." J Bone Miner Res **29**(5): 1101-1109.

Stone, K. L., D. G. Seeley, L. Y. Lui, J. A. Cauley, K. Ensrud, W. S. Browner, M. C. Nevitt, S. R. Cummings and G. Osteoporotic Fractures Research (2003). "BMD at multiple sites and risk of fracture of multiple types: long-term results from the Study of Osteoporotic Fractures." J Bone Miner Res **18**(11): 1947-1954.

Suri, P., D. C. Morgenroth and D. J. Hunter (2012). "Epidemiology of osteoarthritis and associated comorbidities." PM R **4**(5 Suppl): S10-19.

Swadener, J. G., J. Y. Rho and G. M. Pharr (2001). "Effects of anisotropy on elastic moduli measured by nanoindentation in human tibial cortical bone." J Biomed Mater Res **57**(1): 108-112.

Tai, K., M. Dao, S. Suresh, A. Palazoglu and C. Ortiz (2007). "Nanoscale heterogeneity promotes energy dissipation in bone." Nat Mater **6**(6): 454-462.

Tomanik, M., A. Nikodem and J. Filipiak (2016). "Microhardness of human cancellous bone tissue in progressive hip osteoarthritis." J Mech Behav Biomed Mater **64**: 86-93.

Ulrich, D., T. Hildebrand, B. Van Rietbergen, R. Muller and P. Ruegsegger (1997). "The quality of trabecular bone evaluated with micro-computed tomography, FEA and mechanical testing." Stud Health Technol Inform **40**: 97-112.

van der Linden, J. C., D. H. Birkenhager-Frenkel, J. A. Verhaar and H. Weinans (2001). "Trabecular bone's mechanical properties are affected by its non-uniform mineral distribution." J Biomech **34**(12): 1573-1580.

van Rietbergen, B., H. Weinans, R. Huiskes and A. Odgaard (1995). "A new method to determine trabecular bone elastic properties and loading using micromechanical finite-element models." J Biomech **28**(1): 69-81.

Vilayphiou, N., S. Boutroy, E. Sornay-Rendu, B. Van Rietbergen, F. Munoz, P. D. Delmas and R. Chapurlat (2010). "Finite element analysis performed on radius and tibia HR-pQCT images and fragility fractures at all sites in postmenopausal women." Bone **46**(4): 1030-1037.

von Meyer, G. H. (2011). "The Classic: The Architecture of the Trabecular Bone (Tenth Contribution on the Mechanics of the Human Skeletal Framework)." Clinical Orthopaedics and Related Research **469**(11): 3079-3084.

Wagermaier, W., H. S. Gupta, A. Gourrier, M. Burghammer, P. Roschger and P. Fratzl (2006). "Spiral twisting of fiber orientation inside bone lamellae." Biointerphases **1**(1): 1.

Wang, J., G. J. Kazakia, B. Zhou, X. T. Shi and X. E. Guo (2015). "Distinct Tissue Mineral Density in Plate- and Rod-like Trabeculae of Human Trabecular Bone." J Bone Miner Res **30**(9): 1641-1650.

Wang, J., E. M. Stein, B. Zhou, K. K. Nishiyama, Y. E. Yu, E. Shane and X. E. Guo (2016). "Deterioration of trabecular plate-rod and cortical microarchitecture and reduced bone stiffness at distal radius and tibia in postmenopausal women with vertebral fractures." Bone **88**: 39-46.

Wang, J., B. Zhou, X. S. Liu, A. J. Fields, A. Sanyal, X. Shi, M. Adams, T. M. Keaveny and X. E. Guo (2015). "Trabecular plates and rods determine elastic modulus and yield strength of human trabecular bone." Bone **72**: 71-80.

Wang, Q., M. Alen, P. Nicholson, A. Lyytikainen, M. Suuriniemi, E. Helkala, H. Suominen and S. Cheng (2005). "Growth patterns at distal radius and tibial shaft in pubertal girls: a 2-year longitudinal study." J Bone Miner Res **20**(6): 954-961.

Wang, Q., X. F. Wang, S. Iuliano-Burns, A. Ghasem-Zadeh, R. Zebaze and E. Seeman (2010). "Rapid growth produces transient cortical weakness: a risk factor for metaphyseal fractures during puberty." J Bone Miner Res **25**(7): 1521-1526.

Wang, Z. W., W. Y. Lee, T. P. Lam, B. H. Yip, F. W. Yu, W. S. Yu, F. Zhu, B. K. Ng, Y. Qiu and J. C. Cheng (2016). "Defining the bone morphometry, micro-architecture and volumetric density profile in osteopenic vs non-osteopenic adolescent idiopathic scoliosis." Eur Spine J.

Wehrli, F. W. (2007). "Structural and functional assessment of trabecular and cortical bone by micro magnetic resonance imaging." J Magn Reson Imaging **25**(2): 390-409.

Weinstein, S. L. (1989). "Adolescent idiopathic scoliosis: prevalence and natural history." Instr Course Lect **38**: 115-128.

Wen, C. Y., Y. Chen, H. L. Tang, C. H. Yan, W. W. Lu and K. Y. Chiu (2013). "Bone loss at subchondral plate in knee osteoarthritis patients with hypertension and type 2 diabetes mellitus." Osteoarthritis Cartilage **21**(11): 1716-1723.

Wolfram, U., H. J. Wilke and P. K. Zysset (2010). "Rehydration of vertebral trabecular bone: influences on its anisotropy, its stiffness and the indentation work with a view to age, gender and vertebral level." Bone **46**(2): 348-354.

Wolfram, U., H. J. Wilke and P. K. Zysset (2010). "Valid micro finite element models of vertebral trabecular bone can be obtained using tissue properties measured with nanoindentation under wet conditions." J Biomech **43**(9): 1731-1737.

Yu, W. S., K. Y. Chan, F. W. Yu, B. K. Ng, K. M. Lee, L. Qin, T. P. Lam and J. C. Cheng (2014). "Bone structural and mechanical indices in Adolescent Idiopathic Scoliosis evaluated by high-resolution peripheral quantitative computed tomography (HR-pQCT)." Bone **61**: 109-115.

Zhou, B., X. S. Liu, J. Wang, X. L. Lu, A. J. Fields and X. E. Guo (2014). "Dependence of mechanical properties of trabecular bone on plate-rod microstructure determined by individual trabecula segmentation (ITS)." J Biomech **47**(3): 702-708.

Zhou, B., J. Wang, Y. E. Yu, Z. Zhang, S. Nawathe, K. K. Nishiyama, F. R. Rosete, T. M. Keaveny, E. Shane and X. E. Guo (2016). "High-resolution peripheral quantitative computed tomography (HR-pQCT) can assess microstructural and biomechanical properties of both human distal radius and tibia: Ex vivo computational and experimental validations." Bone **86**: 58-67.

Zhou, B., Z. Zhang, J. Wang, Y. E. Yu, X. S. Liu, K. K. Nishiyama, M. R. Rubin, E. Shane, J. P. Bilezikian and X. E. Guo (2016). "In Vivo Precision of Digital Topological Skeletonization Based Individual Trabecula Segmentation (ITS) Analysis of Trabecular Microstructure at the Distal Radius and Tibia by HR-pQCT." Pattern Recognit Lett **76**: 83-89.

Zysset, P. K., X. E. Guo, C. E. Hoffler, K. E. Moore and S. A. Goldstein (1999). "Elastic modulus and hardness of cortical and trabecular bone lamellae measured by nanoindentation in the human femur." J Biomech **32**(10): 1005-1012.